Multi-wavelength Study of Radio Galaxies in MeerKAT fields

DG Phuravhathu

orcid.org 0000-0002-0870-4569

Dissertation accepted in partial fulfilment of the requirements for the degree *Master of Science in Astrophysical Sciences* at the North-West University

Supervisor:	Prof JO Chibueze
Co-supervisor:	Prof M Böttcher

Graduation October 2023

34207767

Declaration of Authorship

I, Phuravhathu Dakalo Gerold, declare that this dissertation titled, **Multi-wavelength Study of Radio Galaxies in MeerKAT fields** and the work presented in it are my own. I confirm that:

- ☐ This work was done wholly or mainly while in candidacy for a research degree at this University.
- ☐ Where any part of this thesis has previously been submitted for a degree or any other qualification at this University or any other institution, this has been clearly stated.
- ☐ Where I have consulted the published work of others, this is always clearly attributed.
- ☐ Where I have quoted from the work of others, the source is always given. With the exception of such quotations, this thesis is entirely my work.
- ☐ I have acknowledged all main sources of help I do.
- ☐ Where the thesis is based on work done by myself jointly with others, I have made clear exactly what was done by others and what I have contributed myself.

Signed:

Date: 28 April 2023

Acknowledgements

I want to begin by extending my gratitude to the Almighty for the gift of life, good health, and the strength and ability to complete this thesis successfully. A special thank you to my MSc research supervisors, Prof. James Chibueze and Prof. Markus Boettcher, the continuous guidance, motivation and remarkable support throughout my MSc study over the last two years is much appreciated.

I am grateful for the financial support provided by the National Research Foundation (UID: 134321) and the Centre for Space Research (CSR), which was crucial to my ability to complete the thesis. I would also like to extend my gratitude to everyone in the North-West University CSR department for creating a working atmosphere that is highly favourable to productivity; thank you for the productive meetings that both the NWU-CSR Radio Astronomy Research Group and the High Energy Astrophysics Group hosted, which allowed us the opportunity to present our work and get valuable feedback.

Before ending the acknowledgement, I would like to give a shout-out to Anu Kundu, who never failed to pick me up when I was exhausted from typing and taking me to the Klipoog Cafeteria for ice cream and coffee. I furthermore want to express my gratitude to Jane Letsoalo, who has always been there for me whenever needed a friend or confidante.

Lastly, I would like to express my deepest appreciation to my parents and siblings for their unwavering love and support throughout this MSc journey and my entire existence.

Abstract

Active galaxies are distinct sub-types of galaxies; their centres, known as Active Galactic Nuclei (AGN), are the brightest and most persistently luminous objects in the cosmos and the AGN core is where the vast majority of radiated energy is released. When compared to the size of the host galaxy, multiple kilo-parsecs, this region is approximately 10^8 times smaller. The nuclei of the AGN are host to SMBHs (Supermassive Black Holes) that are $10^6 - 10^9 M_\odot$, and thus light cannot travel beyond the event horizon of a black hole because of the extreme gravitational pull it generates. SMBHs' deep gravitational potential has a considerable impact on the dynamics of their surrounding environments; approximately 10% of AGN feature large outflows and jets along their polar axes. Magnetically collimated funnels propel relativistic matter along these jets at almost the speed of light.

This thesis aims to perform a multi-wavelength study of a radio galaxy using the MeerKAT radio telescope, and the 1.28 GHz radio continuum data is reduced and analysed. Because of the massive radio jets that transport vast amounts of energy deep into the intergalactic medium, MKAT J221834.96-082253.50 was selected as the source of interest for this study. The generated spectral index maps of MKAT J221834.96-082253.50 reveal a steep core region that becomes flatter when moving toward the jets. The spectrum is flatter in the inner regions of the lobes than it is towards the edges, where it is steeper. The spectral radiative age map indicates that the core of MKAT J221834.96-082253.50 is older than the jets and lobes.

The one-zone leptonic self-synchrotron Compton (SSC) model was utilized to carry out a fitting of the spectral energy distribution (SED) with non-simultaneous archival multi-wavelength data. The SED exhibits a double-humped shape, which can be accounted for by the synchrotron radiation of relativistic electrons in the lower energy range and the SSC process in the higher energy range.

Keywords: Active Galactic Nuclei; Radio Galaxies; Supermassive Black Holes; Jets; Multi-wavelength; SED; MeerKAT Radio Telescope; MKAT J221834.96-082253.50

Contents

List of Figures

List of Tables

Table of abbreviations

1GC	First Generation Calibration
2GC	Second Generation Calibration
2MASS	Two Micron All Sky Surveys
AGN	Active Galactic Nucleus
BLR	Broad Line Region
EHT	Event Horizon Telescope
Fermi-LAT	Fermi Large Area Telescope
FR I/II	Fanaroff-Riley type I/II
FRB	Fast Radio Burst
FSRQ	Flat Spectrum Radio Quasars
ICS	Inverse Compton Scattering
ISM	Inter Stellar Medium
KAPB	Karoo Array Processor Building
NLR	Narrow Line Region
NRAO	National Radio Astronomy Observatory
PA	position angle
QSO	Quasi-Stellar Object
RMS	root mean squared
SED	Spectral Energy Distribution
SEFD	System Equivalent Flux Density
SMBH	Super-Massive Black Hole
SDSS	Sloan Digital Sky Survey
SSA	Synchrotron self-absorption
SSC	Synchrotron Self-Compton
SKA	Square Kilometre Array
VLA	Very Large Array
WISE	Wide-Field Infrared Survey Explorer

Chapter 1

Introduction

The formation and evolution of galaxies over a period of 13.7 billion years has resulted in the galaxies that exist in the present-day universe. The universe is constituted of dark energy, dark matter and baryonic matter, which are approximately 69%, 26%, and 5%, respectively (Ade et al., 2016).

Galaxy formation and evolution (see Figure 1.1) are both driven by two processes that are interrelated to one another. Firstly, there is the dynamical assembly of the mass distribution that takes place within the framework of the hierarchical structure creation that is dominated by dark matter. Star formation history (SFH) is another process to consider, and it refers to a process of gas being converted into stars, and subsequent feedback mechanisms (Rix et al., 2004).

Galaxies are formed in dark matter halos. Dark matter halo interactions and mergers cause their galaxies to grow hierarchically, leading to the formation of galaxy groups comprising a few galaxies, and eventually, galaxy clusters and superclusters consisting of hundreds to thousands of galaxies. The physical characteristics of galaxies are impacted by the interactions and mergers among them, leading to alterations in their morphology and structure, as well as instigating episodes of star formation (Rees and Ostriker, 1977).

Galaxies are composed of dust, stars, and gas, which are bound together by the force of gravity. According to research conducted over the past two decades, a central massive black hole is found in almost all galaxies (Kormendy et al., 2011) and they are called active galactic nuclei (AGN) if there is enough material to accrete. In recent years, as the quantity of observational data collected by space- and ground-based observatories has increased, the physics of SMBHs has been the focus of a growing number of research projects.

The first AGN was discovered in 1908 by astronomer Edward Arthur Fath. AGNs are the most powerful persistent emitters of high-energy emission in the universe. The core of an active galaxy (the host galaxy of an AGN) has a wide range of sub-types that col-

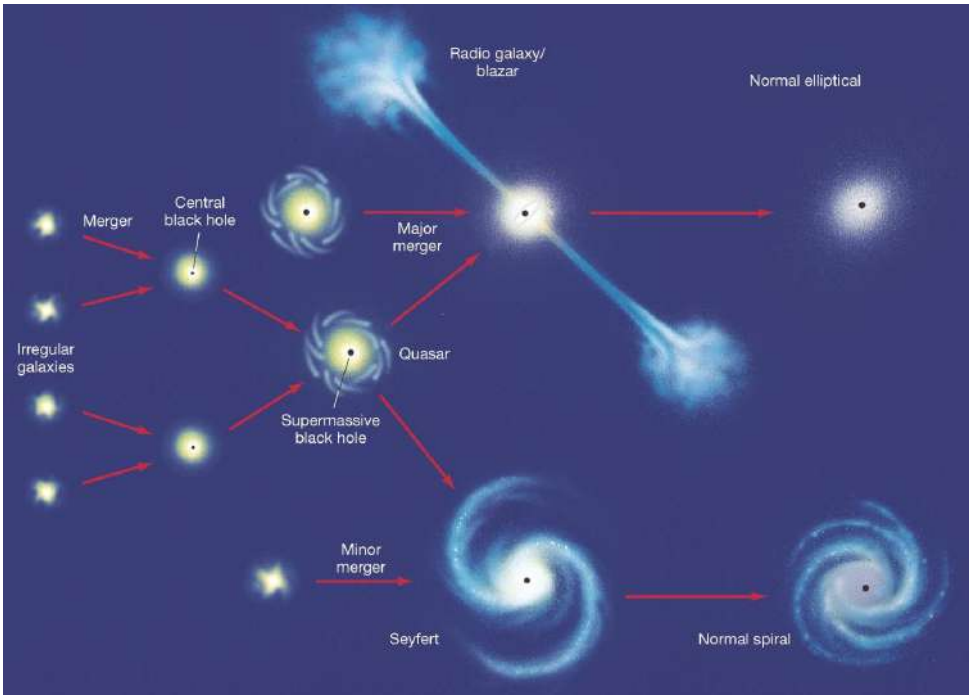

Figure 1.1: Evolutionary sequence for galaxies. As demonstrated, evolution starts with irregular galaxies that merge and form a central black hole. In addition, very bright quasars are formed from these mergers. Furthermore, the radio and Seyfert galaxies formed and were followed by the less violent normal spirals and ellipticals. The primary black holes that drove the early activity are still there, they merely run out of fuel over time. (Credit: Pearson Addison-Wesley (https://pages.uoregon.edu/jimbrau/BrauImNew/Chap25/6th/25_20Figure-F.jpg)).

lectively cover a large parameter space. Radiation, winds, and jets are just a few of the energy feedback mechanisms they use to interact with their surroundings. The current understanding of AGNs is that the primary source responsible for their emission stems from the accretion of matter onto the central SMBH. After being heated by the gravitational energy viscous dissipation, the material that surrounds the black hole forms a rotating disk (Blandford and Payne, 1982).

During the 1930s, Karl Jansky made the groundbreaking discovery of radio emissions originating from outside our planetary system. Grote Reber's pioneering work in radio astronomy in the 1940s led to the discovery of multiple 'radio galaxies' by the 1950s, including Centaurus A, M87 and Cygnus A. Radio galaxies are active galaxies that are distinguished by radio emission that is produced by jets ranging from parsecs (pc) to megaparsecs (Mpc). Most radio emission observed from astrophysical sources is synchrotron emission, and its detection indicates the existence of magnetic fields as well as electrons and/or positrons which are highly relativistic.

Research objectives

This thesis presents a multi-wavelength study of extra-galactic radio sources using MeerKAT data. For a better understanding of the evolution of radio galaxies and their interaction with the intergalactic medium, a multi-wavelength approach is fundamental. The aims of this thesis are to

- identify potentially interesting objects within the available MeerKAT fields for further study, based primarily on their radio morphology;
- assemble available archival multi-wavelength data, including infrared, optical, and X-ray surveys as well as data from the Fermi Gamma-Ray Space Telescope;
- build multi-wavelengths spectral energy distributions for those sources for which sufficient multi-wavelength coverage exists;
- interpret them in the framework of AGN jet emission models to diagnose the physical properties of the jets and their environments.

Thesis Outline

The following is an outline of the content of this thesis: Chapter 2 is the theoretical background where the features of AGN are discussed in greater detail, also the SED, and the theory regarding synchrotron radiation and Inverse-Compton scattering. The observations and the techniques used to process the data are described in Chapter 3. The archival catalogues from which the multi-wavelength data were obtained are also briefly described. Chapter 4 presents the results of the MeerKAT fields' sources and the SED model's input parameters. The results that are reported in Chapter 4 are discussed in Chapter 5. The conclusion and summary are presented in Chapter 6.

Chapter 2

Theoretical Background

The purpose of this chapter is to introduce the characteristics of AGN. Some of the characteristics that have been observed include non-thermal emission, strong emission lines, relativistic jets, and variability across a broad range of wavelengths. An overview of the different types of AGN is presented, and thereafter an explanation concerning radio galaxies and why they are studied. The theory of synchrotron radiation and Inverse-Compton scattering are thoroughly covered in this chapter. The SED is discussed in detail in this chapter, which highlights the importance of the multi-wavelength study.

2.1 Active Galactic Nuclei

2.1.1 What are Active Galactic Nuclei?

AGNs are assumed to be powered by supermassive black holes located at their centres. The results of material falling into the gravitational well, with some energy possibly extracted from the rotation of the black hole, release vast amounts of energy in various forms such as radio, optical, X-ray, or gamma radiation, as well as relativistic particle jets. The observed energy output is powered by matter falling into a SMBH, which has a mass that is millions or billions of times greater than the Sun's. AGNs can outshine their host galaxies by hundreds to thousands of times.

In Figure 2.1 the unified model of AGN is represented, consisting of common features of all types of AGN. The variability in AGN characteristics is associated with the direction of the line of sight relative to the nucleus/galaxy/jet. The unified model posits that within AGNs, there exists a central SMBH that is encompassed by a gaseous accretion disk that extends over a distance of a few light days. The broad emission lines observed in various AGN spectra are the result of fast-moving gas clouds, approximately at sub-parsec distances from the centre of the AGN. At a distance of a few parsecs, there is a molecular doughnut or torus of cool gas. It is optically thick, and when viewed from the edge, ob-

scures the broad line region (BLR) and the accretion disc. The narrow line region (NLR) exists at a distance of a few hundred parsecs from the centre of the galaxy (Blandford et al., 2019). Various AGN spectra show narrow emission lines that are created by clouds, which are ionized by the accretion disk radiation. There is also the presence or absence of a jet(s) depending on the type of AGN.

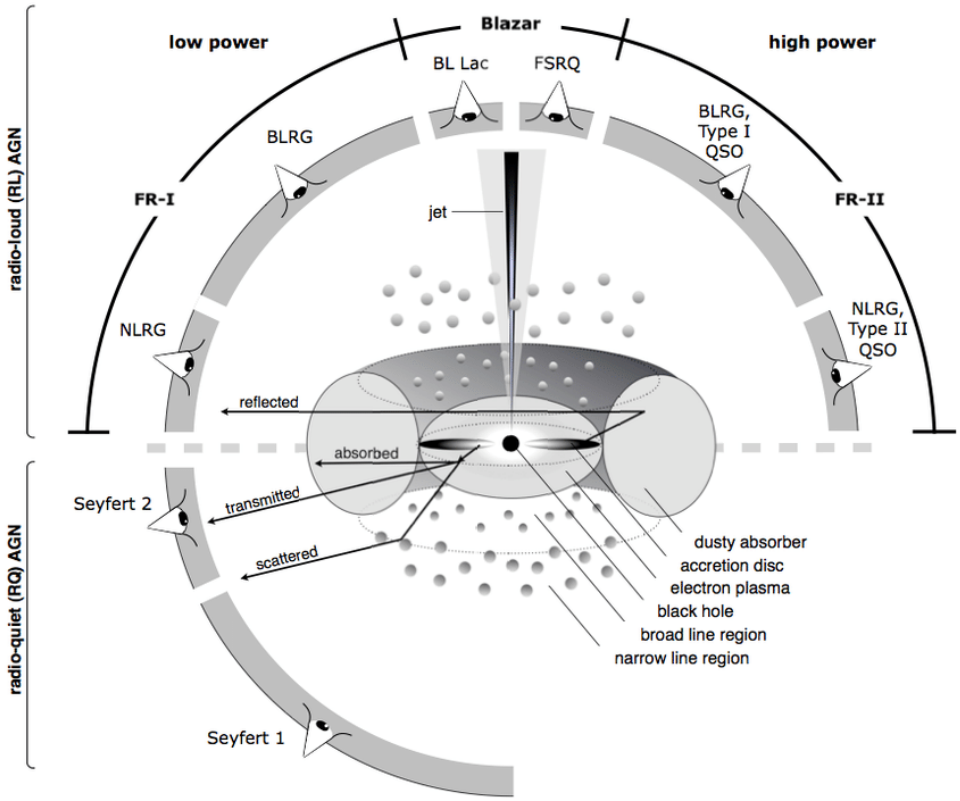

Figure 2.1: The Unified Model of AGN as shown in a schematic diagram. (Credit: Beckmann and Shrader 2013a).

What Turns a Galaxy into an AGN?

The luminosities of the Galactic centre and the centres of most other galaxies, have significantly lower magnitudes when compared to the Eddington luminosities that are determined from the masses of black holes (BHs). The Eddington luminosity, also known as the Eddington limit, refers to the utmost luminosity that an object can achieve, provided that there is an equilibrium between the radiation force that acts outward and the gravitational force that acts inward. As a result, the presence of a black hole is not a sufficient requirement for the existence of an AGN in the galaxy. Additionally, there needs to be a substantial amount of material that can be accreted into the galaxy's core black hole to make it an AGN. This matter can take the shape of diffuse gas accreted across a disk or a dense cluster of stars surrounding the black hole, depending on how dense the cluster is (Courvoisier, 2001).

The Central Engine

Supermassive black holes within the range of 10^4 - 10^{10} $M_\odot$ are assumed to be located inside the central engine. The gravitational potential energy is converted into radiation and outflow as the material is accreting onto the SMBH (Beckmann and Shrader, 2013b). The amount of energy released in AGN can only be explained by a tremendous gravitational potential, as seen in an SMBH. Black holes are characterised by their mass M_{BH} and spin a. The *event horizon*, is the radius below which it is impossible for any electromagnetic radiation, including visible light, to escape, and is a fundamental concept concerning BHs.

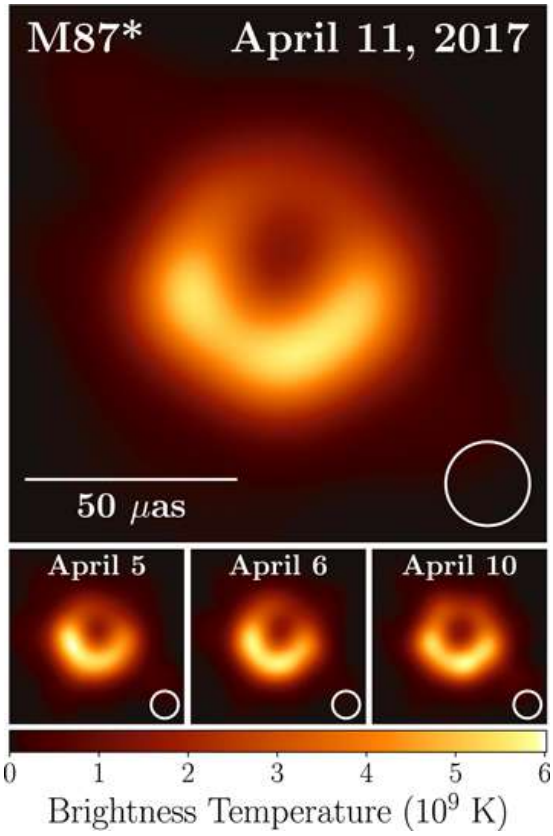

Figure 2.2: Image of M87 obtained by using the EHT at a frequency of 230 GHz. Top: an averaged picture for 11 April 2017. Bottom: comparable images from three other days. The brightness temperature is represented by the colour scale. General relativistic magnetohydrodynamic (GMRHD) simulations of a Kerr black hole provide a picture that is compatible with the data. It reveals what is known as the shadow of the black hole, which is characterised by a central flux depression and an asymmetric photon ring (Falcke et al., 1999). It is possible to explain it by an SMBH spin that points away from the Earth and the effects that Doppler beaming has as a consequence on the flowing plasma. (Credit: EHT Collaboration et al. 2019).

The Schwarzschild metric is used to characterise a black hole that does not rotate, and the Schwarzschild radius (R_S) is equal to the event horizon. This radius is defined as:

$$R_S = \frac{2GM_{BH}}{c^2} \tag{2.1}$$

where G is the gravitational constant and c is the speed of light. The Kerr metric describes a black hole that is in rotation, with a spin value denoted by $a = (Jc)/(GM_{BH}^2)$, where J represents the angular momentum of the black hole. The spin value is constrained by the inequality $0 \leq a \leq 1$ (Kerr, 1963). The event horizon radius, R_k, is reduced when the BH's spin is greater than zero and is given as:

$$R_k = 2R_g(1 - \sqrt{1 - a^2}) \tag{2.2}$$

Outside the event horizon, there is a region called the ergosphere and its radius is given as:

$$R_e = R_g(1 + \sqrt{1 - a^2 \cos\theta}) \tag{2.3}$$

where θ is the angle, which is measured with reference to the pole of rotation and R_g is the gravitational radius. In this region, the rotation of a BH is responsible for frame dragging, also known as the Lense-Thirring effect (Bardeen and Petterson, 1975). This effect enables matter located in the ergosphere to obtain rotational energy from the BH.

The Event Horizon Telescope recently produced the first images of the physical vicinity of the SMBH in the active galactic nucleus M 87 and our Galaxy, the Milky Way at event-horizon scales (EHT Collaboration et al. (2019); see Figure 2.2). The final image displays an asymmetric ring that has a diameter of $43 \pm 3\mu as$, which is in accordance with what is expected of a Kerr black hole.

The mass of a potential black hole may be detected and measured by monitoring the orbital movement of a single star or a cluster of stars (Beckmann and Shrader, 2013a). During the 1990s, astronomers obtained a significant discovery that established a correlation between the central black hole mass of a galaxy and the spherical distribution of stars surrounding it, commonly referred to as the "galactic bulge"; this is what makes the centre of the galaxy look like a ball of stars (Magorrian et al., 1998).

According to observational results, the $M - \sigma$ relation is a function of the velocity dispersion σ of a galaxy bulge and the mass M of the supermassive black hole located at its nucleus (see Figure 2.3). The $M - \sigma$ relation has been used to determine the black hole masses of thousands of galaxies. The $M - \sigma$ relation is mathematically represented as:

$$\frac{M_{BH}}{10^8 M_\odot} = \alpha\Big(\frac{\sigma}{200 kms^{-1}}\Big)^\beta, \tag{2.4}$$

values of α and β may vary by a minor fraction from one survey to the next, as reported by Beckmann and Shrader (2013a); Yang and Bu (2018). Remarkably, one finds $\beta \sim 4$ since this deviates from the simple expectation of $\beta \sim 2$ if the velocity dispersion was a result of the virialised motion of the stars.

Broad and Narrow Line Region

The broad and narrow line regions are two distinct line-emitting regions. There are two different categories of gas clouds based on the spectra: thick, fast-moving clouds are related to the BLR and low-density, slow-moving clouds are related to the NLR. An observable property of AGN that distinguishes them from other galaxies is the existence of emission lines with time-varying intensity that have red and blue shifts. These emission lines possess Doppler widths ranging from a factor of 10^3 to a few 10^4 km s^{-1} (Beckmann and Shrader, 2013a).

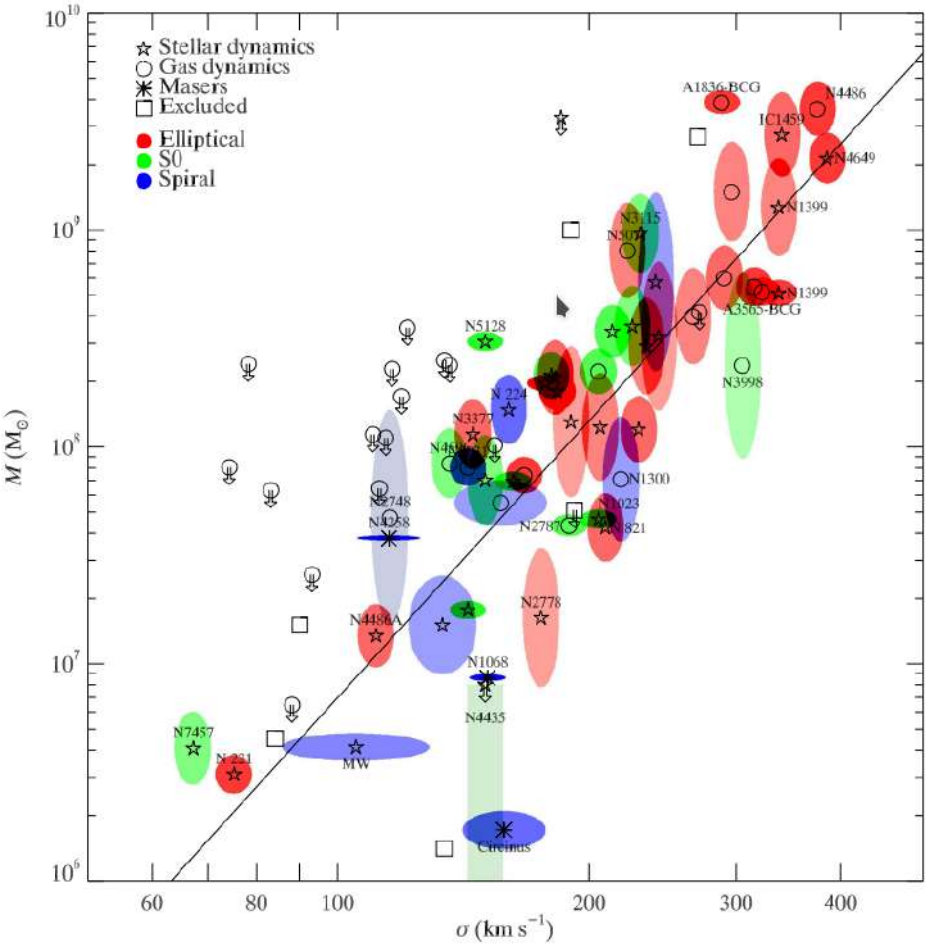

Figure 2.3: Galaxies with dynamical observations of the M–σ relation. There are three types of BH mass measuring methods represented by symbols: star dynamical (squares), masers (asterisks), and gas dynamical (circles). The upper limits of 3σ to BH masses are indicated by the arrows. (Credit: Gültekin et al. 2009).

Broad-line region (BLR)

The central engine is enclosed within the centre of the dust torus by the clouds of the BLR, which are illustrated in Figure 2.1. The BLR radius depends on the accretion-disk

luminosity, and it is of the order of $\sim 10^{16}$ - 10^{18} cm or even larger. Any dust present in this location will be vaporised when the clouds are subjected to the strong radiation from the accretion disk, resulting in extremely high temperatures in the clouds. The precise temperature of BLR clouds can be measured and the typical values are around 10^4 K (Netzer and Woltjer, 1990). Compared to the SMBH, the amount of mass is insignificant and is less than $10M_{\odot}$.

Narrow-line region (NRL)

Figure 2.1 shows that the NLR is located considerably farther away from the central engine, resulting in significantly slower orbital speeds; orbital speeds of $200 - 900$ km s^{-1} are common for the NLR. One of the most significant effects of the NLR's being beyond the dust torus is that it is always visible. This makes it possible to observe narrow lines even when the broad-line releasing gas is hidden. The NLR is the outermost component of the AGN and does not have a distinct limit. Furthermore, it shows the regions of the gas that are illuminated by the radiation that emanates from the accretion disk. Basically, the expanded region is just ionized interstellar gas from the engine's radiation.

Relativistic Jets

In some sub-classes of AGN, there are jets that emanate from the region around their active nuclei. They can extend into space for hundreds of kilo-parsecs or perhaps mega-parsecs while keeping a remarkable degree of collimation (Blandford et al., 2019).

Long-baseline interferometry, which is particularly useful for resolving AGN jets in radio frequency measurements, is the most common method for imaging AGN jets. Around 10% of AGN, also known as radio-loud sources, have jets. Those AGNs are further distinguished by the existence of a broad, non-thermal continuum that is due to synchrotron radiation from the charged particle population (Beckmann and Shrader, 2013b). The jets might appear irregular and short, or straight and lengthy, or curved in shape (Agarwal et al., 2021). Depending on the morphology of the jets, they might be generally smooth or dominated by knots, which are bright enhancements. Superluminal knots are most common in blazars, although in radio galaxies, the knots are usually sub-luminal (see Figure 2.4).

Jets are formed when a dense gas of particles is ejected perpendicular to the accretion disc in the vicinity of the black hole. These particles are then accelerated and spiral along the helical magnetic fields, which causes them to generate synchrotron radiation (Böttcher et al., 2012). The curving of these magnetic fields, due to the rotation of the accretion disk causes the outflow to be collimated in the rotation axis direction of the central engine (Beckmann and Shrader, 2013a).

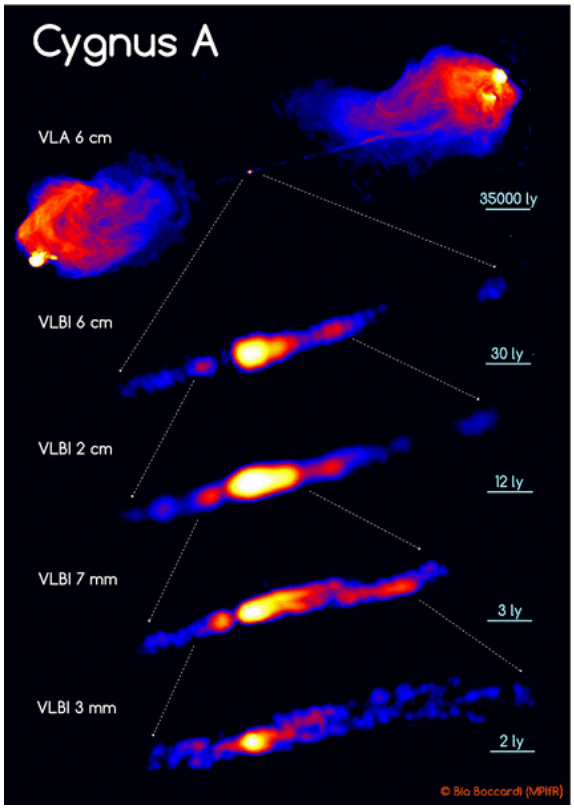

Figure 2.4: The jets of the radio galaxy Cygnus A, on various scales, from hundreds of kilo-parsecs as observed by the Very Large Array to sub-parsecs as observed by mm-VLBI. The VLBI images are produced by stacking numerous epochs of data together. The MOJAVE survey provided the data at 2 cm. (Credit: Boccardi et al. 2017).

2.1.2 Classification of the AGN

The most common categorisation designations for AGN are as follows: Type 1 AGN are those that have broad permitted lines that can be detected at optical wavelengths, whereas Type 2 AGN are those that have only narrow emission lines. AGNs may be classified into various categories based on their geometry and the angle at which the observer is viewing them (see Table 2.1). It is possible to detect the BLR in the immediate vicinity of an AGN when viewing it through a line of sight that is in close proximity its polar axis (Maini, 2016); however, only the NLR can be detected when viewing it across the equatorial axis of an obscuring structure. The classification of AGNs in the unified scheme is based on their viewing angle, as illustrated in Figure 2.1.

Seyfert galaxies

Seyfert Galaxies are spiral galaxies with compact, bright cores that fluctuate in brightness and have broad or narrow emission lines. Carl Seyfert identified a significant subset of spiral galaxies in 1943 with an incredibly bright point-like nucleus. When compared to regular galaxies, Seyfert galaxies have been observed to emit much more radiation in the far-infrared and other wavelengths. It is estimated that approximately 1% of spiral

Property:	**Radio Galaxies:**	**Seyfert Galaxies:**	**BL Lac Objects:**	**Quasars:**
Galaxy Type:	Giant Elliptical	Spiral	Elliptical	Spiral and Elliptical
Appearance:	Elliptical	Compact Bright Nucleus	Bright, Star-like	Compact, Blue
Emission Spectrum:	Rare, Broad and Narrow	Broad and Narrow	Very Weak	Broad and Narrow
Absorption Lines:	Yes	Yes	Yes	Yes
Red shift:	$z < 0.05$	$z \sim 0.05$	$z \sim 0.1$	$z > 0.5$
Emits Radio:	Strong	Weak	Weak	Some
Variability:	Days	Days to Weeks	Minutes	Days to Weeks
Jets:	Often	Some	All	Some

Table 2.1: A brief overview of the various types of AGN. This table was adapted from Cosmology - Galaxies (http://astronomyonline.org/Cosmology/Galaxies.asp).

galaxies are anticipated to exhibit Seyfert-type properties that are observed in Seyfert galaxies. The relative widths of emission lines in a spectrum of a galaxy are used to identify it as a Seyfert galaxy or not (Koulouridis et al., 2013).

Quasars

A quasi-stellar object (QSO), commonly referred to as a quasar, is an enormously bright AGN powered by a SMBH with a mass that ranges from $10^6 M_\odot$ to $10^{10} M_\odot$. Quasars are surrounded by a gaseous accretion disc (Leckrone, 2020) and a spectrum significantly different to those of stars. The significantly red-shifted emission lines were found to originate from hydrogen and other elements that exist naturally in astronomical sources. It is estimated that around 10% of quasars are intense radio emitters, and those quasars are thus considered radio-loud. The host galaxies of quasars have been challenging to investigate because of their large distances (D'Onofrio et al., 2012). It has also been discovered that elliptical and interacting galaxies are more likely to harbour radio-loud quasars (QSOs).

Blazars

Blazars are a type of AGN that emit jets of relativistic particles in a direction that is in close proximity to the observer's viewing angle. By beaming electromagnetic radiation from the jets in a relativistic state, blazars look far brighter than they would appear if

the jets were pointing in a different direction, away from Earth. Blazars are very intense sources of emission over the whole electromagnetic spectrum and are observed to be high-energy gamma-ray photons emitters. When it comes to brightness variations, blazars are extremely variable sources that frequently experience quick and dramatic changes in brightness over short time frames (Urry and Padovani, 1995).

A blazar may be categorised into two types: BL Lacertae (BL Lacs) and Flat Spectrum Radio Quasars (FSRQs) type objects (Sokolovsky et al., 2014). Low-luminosity radio galaxies have their beamed counterparts known as BL Lac objects, whereas high-luminosity radio galaxies are known as FSRQs. In 1978, the term "blazar" was invented by astronomer Edward Spiegel to describe the combination of these two types in a jet approaching the viewer at near-light speed (Webb, 2012).

Radio Galaxies

Radio galaxies are elliptical galaxies with an active nucleus, harbouring a supermassive black hole, powering relativistic beams (jets) of particles that extend over thousands of light-years into intergalactic space. The radio emission that jets emit is explained by the synchrotron process. Radio galaxies are distinguished by the presence of powerful radio sources in the range of 10^{41} - 10^{46} ergs s^{-1}. About 0.01% of all galaxies are radio galaxies. All radio galaxies show the presence of two perpendicular lobes or jets in relation to their accretion discs (Böttcher et al., 2012).

It has been discovered that radio galaxies have jets that stretch out to distances that are significantly larger than the galaxy's own size (Delhaize et al., 2021). Radio galaxies have a luminosity range of 0.1 to 10 times that of the Milky Way across all wavelengths. While intense radio emission from jets and their termination regions is the distinguishing feature of radio galaxies, the jets are known to radiate right through the electromagnetic spectrum, including X-rays and gamma-rays, with a handful of them being detected by the ground-based atmospheric Cherenkov Telescopes (at very high energy (VHE) band, >100 GeV) (e.g., Cen A: H. E. S. S. Collaboration et al. (2018); M87: VERITAS Collaboration (2010)).

Why do we study radio galaxies?

For galaxies to become massive, they must have grown for a very long period, perhaps hundreds of millions to billions of years (Garofalo and Singh, 2019). Astronomers will therefore be unable to study radio jets just by observing the evolution of one radio galaxy; a large number of distinct radio galaxies at various phases of their life cycles should, alternatively, be examined to reach a better understanding. It is possible to detect radio-loud active galaxies from a great distance, making them essential tools in observational cosmology and galactic evolution research. In addition, understanding radio galaxy jets is

critical because they are so powerful; these jets impact both the galaxy from which they originate and their environment.

Structure of Radio Galaxies

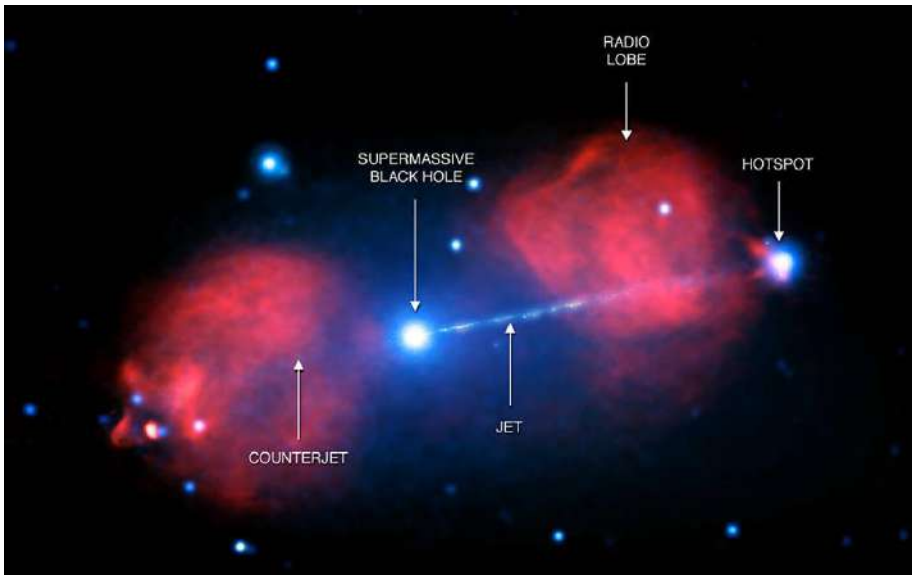

Figure 2.5: The radio galaxy Pictor A has a jet that stretches for 300,000 light years out from its central active galactic nucleus toward a luminous hot-spot and a counter jet that points in the opposite direction, as shown in this Chandra X-ray image. (Credit: X-ray: NASA/CXC/Univ. of Hertfordshire/M. Hardcastle et al.; Radio: CSIRO/ATNF/ATCA (https://www.nasa.gov/mission_pages/chandra/the-pictor-a-galaxy-with-labels.html).

One of the most prominent features of radio galaxies is the diversity of their morphologies. Most large-scale morphologies have lobes that are characterized by elliptical double structures situated on either side of the active nucleus and are approximately symmetrical. The nucleus of radio galaxies emits one or two observable extended narrow jets that go directly to the lobes of the galaxy (Montani and Petitta, 2014), as shown in Figure 2.5.

Fanaroff and Riley categorised radio sources into Fanaroff and Riley Class I (FRI) and Class II (FRII) in 1974. FRI objects are low-luminosity and possess weak jets, whereas FRII objects were high-luminosity and have powerful jets and intense hot-spots at the extremities of the lobes (Fanaroff and Riley, 1974). FRIIs are capable of successfully transporting energy to the lobes' ends. FRI beams, however, are inefficient because they radiate a considerable portion of their energy away while travelling (Fanaroff and Riley, 1974).

Since radio emission is strongest in the regions where FRI jets are decelerating (Laing and Bridle, 2002), it seems that the FRII/FRI transition shows whether a jet or beam may be emitted from the host galaxy without being slowed down to speeds much below the speed of light by interactions with the intergalactic medium. The relativistic beaming effects have been studied to determine that the jets of FRII sources maintain relativistic

speeds to the ends of the lobes. The spectral energy distributions of the hot spots, which are typically present in FRII sources and are believed to be visible characteristics of shock waves that arise as a result of the relativistic jet encountering the surrounding medium (the intergalactic medium or the interstellar medium of the galaxy) (Hardcastle et al., 2004). Multiple hot-spots are frequently observed, indicating either an ongoing outflow subsequent to the shock or migration of the termination point of the jet (Meisenheimer et al., 1989).

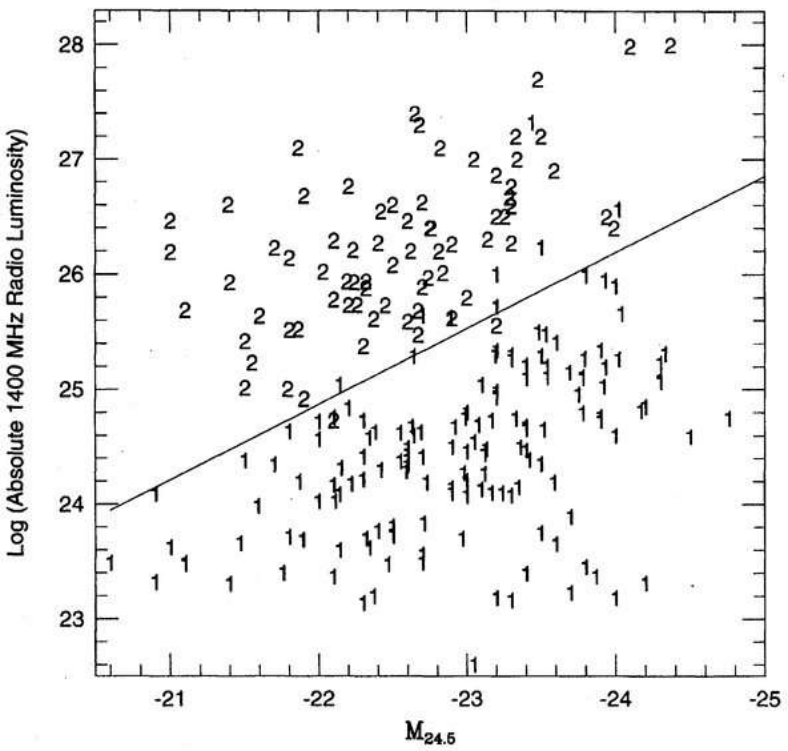

Figure 2.6: Comparison of Fanaroff-Riley morphological classification with radio and optical luminosities (the radio luminosity at 1.4 GHz against the absolute optical magnitude of the host galaxy). (Credit: Böttcher et al. 2012).

Depending on their radio structure, several kinds of radio sources have been named:

- When an FRII source has identifiable hot-spots, it is referred to as a classical double.
- An FRI source with a wide-angle tail has jets and occasionally hot-spots but plumes rather than lobes in the centre of clusters; this is an intermediate structure between FRI and FRII.
- "head-tail source" or "narrow-angle tail" might be used to describe an FRI that bends due to ram pressure.
- There are no jets, or hot-spots, in fat doubles, which are diffuse lobed sources without

jets. They could be things like relics that have had their energy supply turned off for good, or just for a short time.

- Wide-angle-tailed radio galaxies (WATs) are commonly observed in cluster environments. These galaxies are characterized by the presence of radio-emitting jets that have been bent into a distinctive 'C' shape.

The radio emission from the lobes is consistent with synchrotron emission, which is produced by energetic electrons travelling in a magnetic field (Condon and Ransom, 2016). The conclusion was that the structures of radio galaxies are made up of magnetized relativistic plasma. It is necessary to have a source of high-energy electrons since synchrotron-emitting electrons lose their energy rapidly.

2.2 Radiative Processes

Line emission is caused by atomic processes that only have very particular quantised energies, whereas continuum emission is caused by processes in which the energy exchange is not quantised and, as a result, the photons emitted might have an irregular energy distribution. The derivations presented in this section mostly draws the work of Pacholczyk (1970), Rybicki et al. (1979), and Böttcher et al. (2012).

2.2.1 Thermal and non-thermal radiation

Thermal radiation is a type of radiation whose intensity is related to the temperature of the source that gives out radiation. On the other hand, non-thermal radiation is radiation whose characteristics are not affected by the source's temperature (Burke et al., 2019). In astronomy, the following are forms of non-thermal radiation that are commonly encountered: Synchrotron emission, Compton scattering, and MASER emission.

The primary distinction between non-thermal and thermal emission is found in the characteristics of their respective sources. The spectra of non-thermal and thermal radiation are significantly different (Birkinshaw, 1999). Thermal radiation has a typical exponential drop-off at its highest energy levels, while non-thermal radiation can have a long 'tail' at high energy (Rosswog and Bruggen, 2003) which is represented by as a power law with the form $S_v \propto E^{-a}$. At shorter wavelengths, the emission from AGN is mainly from the thermal contribution from the galaxy/nucleus, while at longer wavelengths, it is the non-thermal emission from the jet. Thermal radiation is emitted by all bodies above absolute zero because charged particles (such as electrons in atoms) accelerate and generate electromagnetic radiation. The concept of a blackbody is the most basic example of thermal emission.

2.2.2 Synchrotron radiation

A kind of electromagnetic radiation called synchrotron radiation is produced due to the deflection of relativistic particles moving in a magnetic field. It is emitted at a variety of energies, resulting in a wide spectrum of energy emissions. The phenomenon of Cyclotron radiation refers to the emission of radiation by particles that are non-relativistic. On the other hand, Synchrotron radiation refers to the emission of radiation by particles that are relativistic (Rybicki and Lightman, 1991).

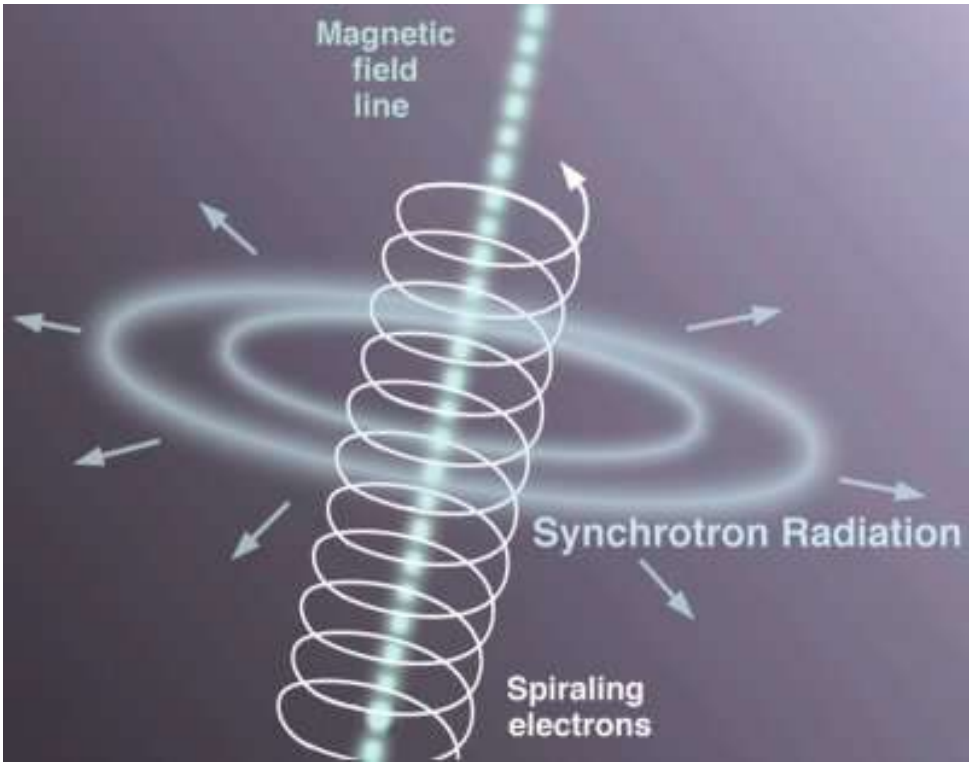

Figure 2.7: Synchrotron radiation. Electrons produce a narrow synchrotron radiation beam when they spiral around a magnetic field at close to the speed of light. (Credit: Jon Lomberg/Gemini Observatory).

Synchrotron radiation has been discovered to be emitted by a wide variety of astronomical objects. The magnetic field strength and particle energy are directly proportional to the frequency and intensity of the emitted radiation (Burke et al., 2019). According to classical electromagnetism, the Larmor equation can be used to determine the amount of power that is radiated by a particle with a charge q and is undergoing acceleration:

$$P(t) = -\frac{dE}{dt} = \frac{2}{3}\frac{q^2}{c^3}a^2(t) = \frac{2}{3}\frac{q^2}{m^2c^3}\left(\frac{d\mathbf{p}}{dt}\right)^2 \tag{2.5}$$

where $\mathbf{p} = \gamma m\mathbf{v}$ is the momentum of a particle. The power given off is inversely proportional to the mass of the particles squared, which means an electron or positron gives off a factor of 3×10^6 more radiation than a proton.

The Lorentz factor $\gamma = 1/\sqrt{1-(v/c)^2} \gg 1$ for relativistic particles ($v \approx c$). Lorentz transformation is taken into account to determine the relationship between values in two different frames of reference. Because the radiated power is known to be Lorentz invariant, it can be mathematically represented as:

$$P = P' = \frac{2}{3}\frac{q^2}{c^3}a'^2 = \frac{2}{3}\frac{q^2}{c^3}(a_{\parallel}'^2 + a_{\perp}'^2) \tag{2.6}$$

The primed quantities describe the particle's frame of rest, while the non-primed quantities describe the observer's frame. The acceleration in the above equation is separated into its perpendicular and parallel components. These components were Lorentz transformed and they can be written as (Rybicki and Lightman, 1991):

$$a_{\parallel}' = \gamma^3 a_{\parallel} \tag{2.7}$$

$$a_{\perp}' = \gamma^2 a_{\perp} \tag{2.8}$$

Therefore,

$$P = P' = \frac{2}{3}\frac{q^2}{c^3}a'^2 = \frac{2}{3}\frac{q^2}{c^3}(a_{\parallel}'^2 + a_{\perp}'^2) = \frac{2}{3}\frac{q^2}{c^3}\gamma^4(\gamma^2 a_{\parallel}^2 + a_{\perp}^2) \tag{2.9}$$

As shown in Figure 2.7, when the electric field ($\mathbf{E}$) is negligible the Lorentz force is acting, the force is given by this:

$$F_L = \frac{d}{dt}(\gamma m_e|\mathbf{v}|) = \frac{e}{c}|\mathbf{v}\times\mathbf{B}| = \frac{e}{c}vB\sin\alpha \tag{2.10}$$

where α represents the pitch angle, which is defined as the angular separation between the magnetic field and the velocity vector. The cross-product indicates that the only force acting is orthogonal to the lines of the magnetic field. This force also results in acceleration that is orthogonal to the magnetic field, and it takes the following form:

$$a_{\perp} = \frac{evB\sin\alpha}{\gamma m_e c} \tag{2.11}$$

When $v \approx c$ is taken into consideration, $a_{\parallel} = 0$ and $a_{\perp}$ (Equation 2.11) is substituted in the simplified Larmor formula (Equation 2.9), the power that an electron emits when subjected to the Lorentz force is obtained as:

$$P(\alpha) = \frac{2}{3}\frac{e^4}{m_e^2 c^3}B^2\gamma^2\left(\frac{v^2}{c^2}\right)\sin^2\alpha \tag{2.12}$$

When working with a group of mono-energetic particles whose pitch angles are distributed uniformly in all directions, the term $\sin^2 \alpha$ can be averaged throughout the solid angle to yield 2/3. Therefore, the emitted power of an ensemble of electrons can be expressed as:

$$P = \frac{4}{3} c \sigma_T U_B \gamma^2 \beta^2 \tag{2.13}$$

where $U_B \equiv B^2/8\pi$ is the magnetic energy density and $\sigma_T = 8\pi e^2/3m_e c^2 = 6.65 \times 10^{-25} cm^2$ is the electron's Thomson scattering cross section.

The Synchrotron Spectrum

The emission cones at different points along a gyrating particle's path are shown in Figure 2.8. The emission from the electron is beamed in the direction of motion with an opening angle $\sim 1/\gamma$. When an electron moves along the magnetic field lines in its orbit, the observer can only receive the radiation that is emitted by the electron when the cone is pointing along the observer's line of sight (Beckmann and Shrader, 2013a). Pulses are then received as a result of a single electron's emission. The pulse will be seen from locations 1 and 2 along the particle's trajectory (green curve) by the observer. The curvature radius of the path, $a = \Delta S/\Delta\theta$, may be used to calculate the distance ΔS along the path. The orbital angle $\Delta\theta$ forms one angle of a triangle, and the other two angles are equal to $\pi/2 - 1/\gamma$, such that $\Delta\theta = 2/\gamma$.

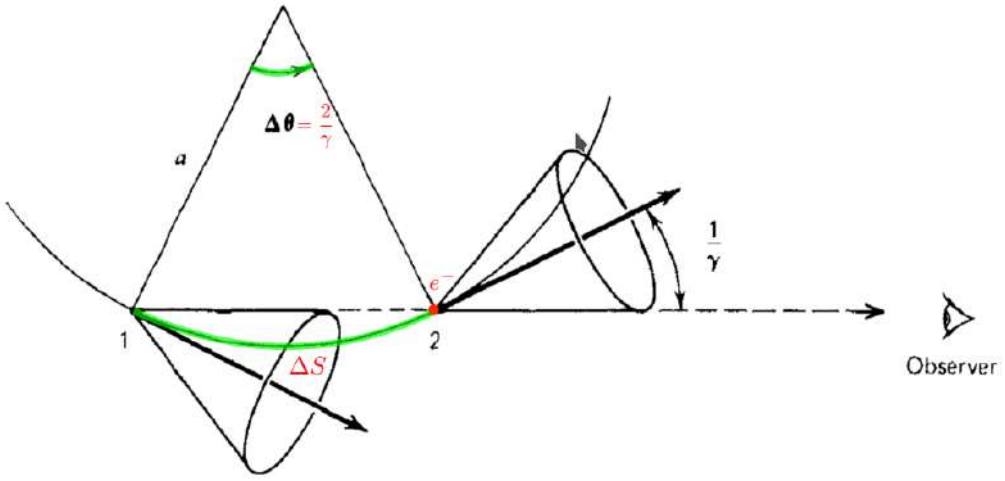

Figure 2.8: The power-generated emission cones at points 1 and 2 at various points. The orbit's radius and the angle between points 1 and 2 are indicated by the symbols a and $\Delta\theta$, respectively. (Credit: Rybicki and Lightman 1991).

The electron's cone of emission turns toward the observer while it is in position 1. When the electron reaches position 2, the pulse stops. There is a pulse of synchrotron radiation visible to the observer with the following duration:

$$\Delta t_p = \frac{\Delta S}{v} - \frac{\Delta S}{c}, \tag{2.14}$$

where $\Delta S/v$ is the time it takes the electron to traverse ΔS and $\Delta S/c$ is the light time taken to traverse ΔS. Following the Lorentz relation of the electron, the duration is:

$$\Delta t_p = \frac{\Delta S}{v}\left(1 - \frac{v}{c}\right) \simeq \frac{\Delta S}{v}\left(\frac{1}{2\gamma^2}\right) \tag{2.15}$$

Using the equation of motion:

$$\mathbf{F} = m\mathbf{a} = m\gamma\frac{d\mathbf{v}}{dt} = \frac{q}{c}|\mathbf{v} \times \mathbf{B}| = \frac{q}{c}vB\sin\alpha \tag{2.16}$$

Which implies

$$m\gamma\frac{|\Delta\mathbf{v}|}{\Delta t} = \frac{q}{c}vB\sin\alpha, \tag{2.17}$$

where $|\Delta\mathbf{v}| = v\Delta\theta$ and $\Delta t = \Delta S/v$. Then

$$m\gamma\frac{v^2\Delta\theta}{\Delta S} = \frac{q}{c}vB\sin\alpha \tag{2.18}$$

Let the relativistic gyration frequency be given as $\omega_g = qB/\gamma mc$, then

$$\Delta S = \frac{v}{\omega_g \sin\alpha}\Delta\theta = \frac{2v}{\gamma\omega_g\sin\alpha} \tag{2.19}$$

The duration of the synchrotron radiation pulse becomes:

$$\Delta t_p = \left(\frac{2v}{\gamma\omega_g\sin\alpha}\right)\left(\frac{1}{v}\right)\left(\frac{1}{2\gamma^2}\right) = \frac{1}{\gamma^3\omega_g\sin\alpha} \tag{2.20}$$

The spectral distribution of radiation in the synchrotron case shows that it peaks at $0.29\nu_c$, as shown in Figure 2.9. This ν_c is inversely proportional to the pulse's duration ($\Delta\tau_p$) and is given by (Pacholczyk, 2014):

$$\nu_c \simeq \Delta\tau_p^{-1} = \frac{3}{4\pi}\gamma^3\omega_g\sin\alpha = \frac{3qB}{4\pi mc}\gamma^2\sin\alpha \tag{2.21}$$

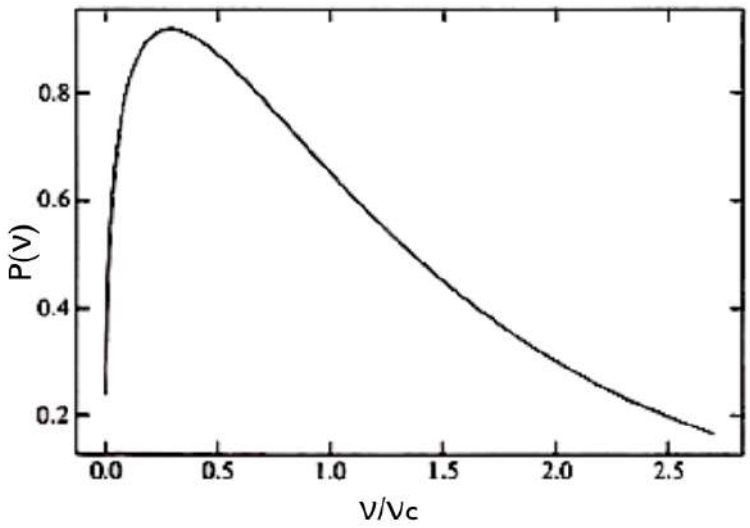

Figure 2.9: Spectrum produced by a single synchrotron electron. The plot shows the synchrotron radiation power emitted by a relativistic electron versus the frequency normalized to the critical frequency ν/ν_c. (Credit: Hughes et al. 1991).

An overall power law spectrum is produced by the superposition of all individual electron spectra, and each has a distinctive critical frequency ν/ν_c. The spectrum generated by the averaged power of a population of electrons whose velocities are distributed according to power law is given by:

$$P_\nu \propto \nu^{\frac{-(p-1)}{2}} \tag{2.22}$$

The radiation spectral index is represented by $\alpha = (1-p)/2$, where p denotes the particle index.

When synchrotron emission is absorbed by the low-energy photons this results in synchrotron self-absorption effects. The coefficient of absorption, α_ν, can be written as (see Böttcher et al. (2012) for a detailed derivation)

$$\alpha_\nu = -\frac{(p+2)}{18\pi m\nu^2}\left(\frac{3q}{4\pi mc}\right)^{\frac{p-1}{2}}\left(\frac{q^2}{mc^2}\right)B^{\frac{p+2}{2}}\nu^{-\frac{p+4}{2}} \tag{2.23}$$

for a power law distribution of particles in the magnetic field B with a mass m and charge q. The synchrotron self-absorption opacity increases as the frequency decreases for any non-thermal electron distribution. Because of this, non-thermal synchrotron sources tend to have an optically thick spectrum below a critical break frequency (Böttcher et al., 2012). Figure 2.10 illustrates the various scenarios of optically thin and thick synchrotron spectra. The source function, $S_\nu = j_\nu/\alpha_\nu$ determines the optically thick spectrum that

can be observed below the frequency of synchrotron self-absorption (Böttcher et al., 2012). This expression demonstrates that there is an increase in opacity in conjunction with a decrease in frequency.

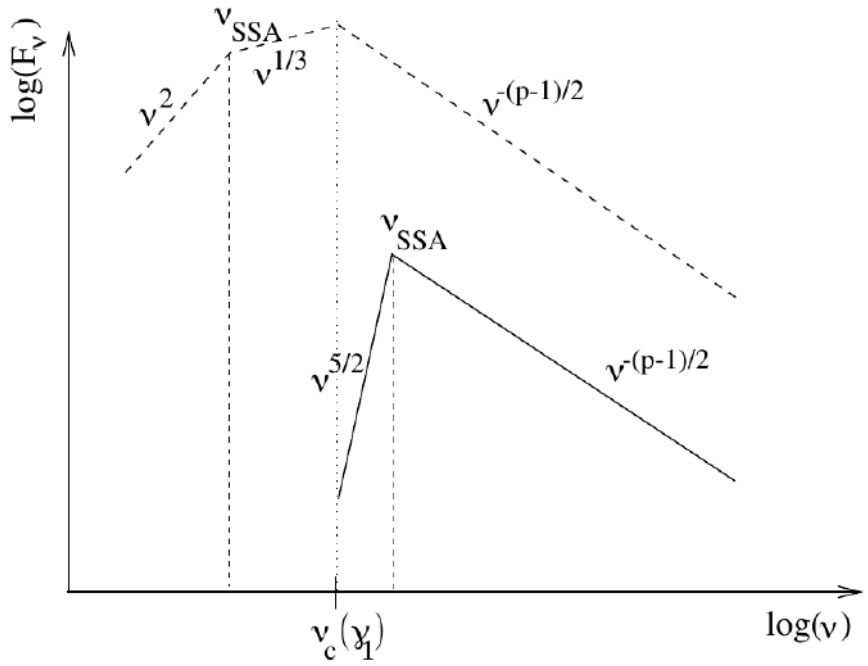

Figure 2.10: Spectra of synchrotron radiation from a power-law distribution of electrons. In the case that the frequency of synchrotron self-absorption is lower than the critical frequency of the electrons with the lowest energy, $\nu_{SSA} < \nu_c(\gamma_1)$, the spectral slope of the optically thick (low-frequency) section will be ν^2, and will turn to optically thin low-frequency synchrotron emission at a slope of $\nu^{1/3}$, which lies between the ν_{SSA} and $\nu_c(\gamma_1)$. In the case when ν_{SSA} is greater than $\nu_c(\gamma_1)$, the spectrum's optically thick (low-frequency) region is a $\nu^{5/2}$ power law. (Credit: Böttcher et al. 2012).

2.2.3 Inverse-Compton Scattering (ICS)

Compton scattering refers to the phenomenon of inelastic scattering between a photon and a charged particle, usually an electron (see Figure 2.11). The inverse Compton process involves relativistic electrons scattering low-energy photons to produce high-energy ones; as a result, the electrons lose energy while the photons gain energy. This process is efficient in astronomical sources that contain a hot corona around the accretion disk, such as the region around Galactic or supermassive black holes; it is efficient when there are ultra-relativistic electrons and target photon field to scatter (Rybicki and Lightman, 1991).

The process of ICS can result in the photon gaining enough energy to scatter from optical to X-ray and γ-ray frequencies depending on whether the relativistic electron is sufficiently energetic. There are two distinct regimes: the Thomson and the Klein-Nishina regime, that may be identified by comparing the scattering cross sections at different photon en-

ergies in the electron's rest frame. In the Thomson regime, the incoming photon's energy is less than the rest mass of the electron in the electron's rest frame ($\gamma h\nu \ll m_e c^2$), but the photon's energy is greater than the rest mass of the electron ($\gamma h\nu \gg m_e c^2$) in the Klein-Nishina regime.

Several distinct kinds of photon fields could be involved in inverse Compton scattering in AGN. In the synchrotron self-Compton (SSC) emission process, the electrons that first produced the synchrotron photons are also responsible for their subsequent up-scattering. In the case of external photon fields, a different parent population emits the seed photons; this process is known as external Compton emission (Meyer et al., 2012).

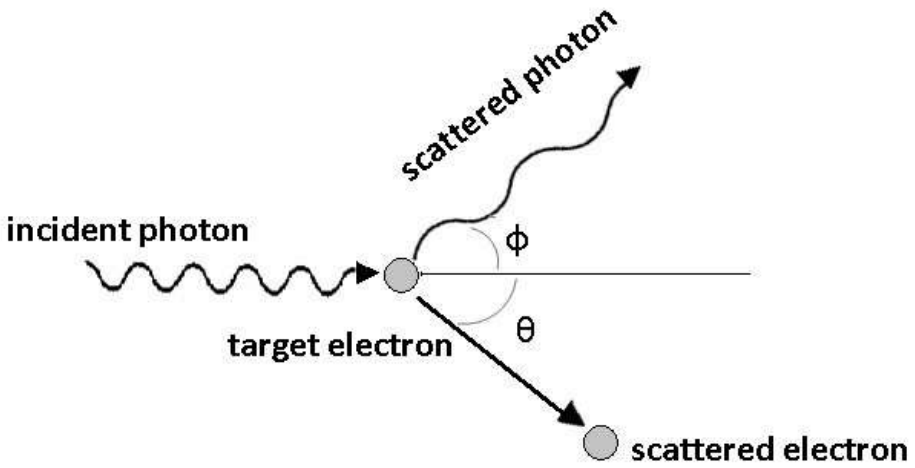

Figure 2.11: Inverse Compton Scattering is the process in which an electron with relativistic energy produces a high-energy photon that is higher in energy than the incoming photon. (Credit: Venugopal and Bhagdikar 2012).

The power in Inverse-Compton scattering from a single electron

Consider the Thomson scattering that is non-relativistic which is occurring within the electron's rest frame (Condon and Ransom, 2016). The power that is scattered may be expressed as:

$$P = \sigma_T c U_{rad}, \tag{2.24}$$

where U_{rad} is the incident radiation energy density. Now take into account the ultra-relativistic electron scattering radiation. The above equation is only true in the primed frame that is in motion at an equivalent speed as that of the electron:

$$P^{'} = \sigma_T c U^{'}_{rad} \tag{2.25}$$

This non-relativistic result must be converted into the unprimed rest frame of the observer. This is derived by using the following result:

$$P \equiv \frac{dE}{dt} = \frac{dE}{dt'}\frac{dt'}{dt} = \frac{dE}{dE'}\frac{dE'}{dt'}\frac{dt'}{dt} = P' \tag{2.26}$$

In other words, the power is invariant under Lorentz transformation, therefore,

$$P = \sigma_T c U'_{rad} \tag{2.27}$$

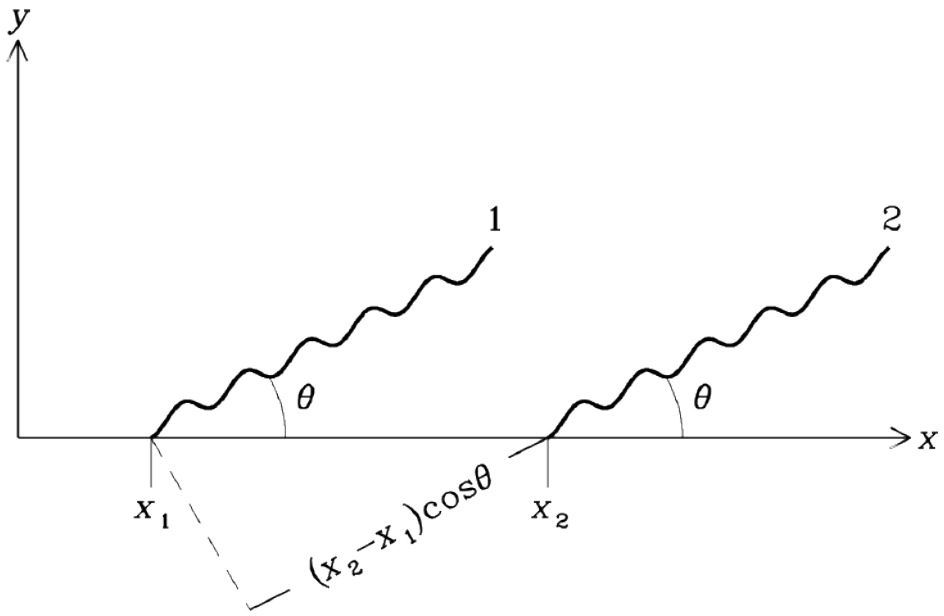

Figure 2.12: Two photons strike an electron travelling to the right in rapid succession in an unprimed observer's frame as they approach the x-axis, and the photons are at an angle θ to it. (Credit: Condon and Ransom 2016).

To Lorentz transform U'_{rad} to U_{rad}, consider an electron moving from x_1 to x_2 being affected by two low-energy photons coming from the x-axis at an angle θ, as illustrated in Figure 2.12 (Condon and Ransom, 2016). The coordinates of these events in an unprimed frame are as follows:

$$(t_1, x_1, 0, 0) \text{ and } (t_2, x_2, 0, 0) \tag{2.28}$$

If these two events occur in the same frame of reference as the observer, then the Lorentz transform provides the coordinates of these two events as

$$(\gamma t'_1, \gamma v t'_1, 0, 0) \text{ and } (\gamma t'_2, \gamma v t'_2, 0, 0) \tag{2.29}$$

It takes time Δt for the two photons to arrive at the plane (shown in Figure 2.12), which, in the reference frame of the observer, is perpendicular to the direction of propagation

(Condon and Ransom, 2016).

$$\Delta t = t_2 + \frac{(x_2 - x_1)}{c}\cos\theta - t_1 \tag{2.30}$$

$$= \gamma t_2^{'} + \frac{(\gamma v t_2^{'} - \gamma v t_1^{'})}{c}\cos\theta - \gamma t_1^{'} \tag{2.31}$$

$$= (t_2^{'} - t_1^{'})[\gamma(1 + \beta\cos\theta)], \tag{2.32}$$

where $\beta \equiv v/c$. In the electron's frame, the time interval between being impacted by two photons is $\Delta t^{'} = t_2^{'} - t_1^{'}$, so

$$\Delta t = \Delta t^{'}[\gamma(1 + \beta\cos\theta)] \tag{2.33}$$

A wave with a frequency of $\nu^{'} = (\Delta t^{'})^{-1}$ in the moving frame and $\nu = (\Delta t)^{-1}$ in the frame of the observer has a time interval that elapses of Δt between two subsequent cycles arrivals. Then

$$\nu^{'} = \nu[\gamma(1 + \beta\cos\theta)] \tag{2.34}$$

If we consider the frame of the electron, each photon's energy $E^{'} = h\nu^{'}$ and frequency $(\nu^{'})$ are multiplied by $[\gamma(1 + \beta\cos\theta)]$. Furthermore, this factor is used to multiply the rate at which subsequent photons arrive, if in the frame of the observer, the photon density is denoted by n_γ, then $n_\gamma^{'} = n_\gamma[\gamma(1 + \beta\cos\theta)]$. The energy density of radiation in the observer's frame is

$$U_{rad} = n_\gamma h\nu, \tag{2.35}$$

in the frame of the electron

$$U_{rad}^{'} = n_\gamma^{'} h\nu^{'} = n_\gamma[\gamma(1 + \beta\cos\theta)]h\nu[\gamma(1 + \beta\cos\theta)] \tag{2.36}$$

$$= U_{rad}[\gamma(1 + \beta\cos\theta)]^2 \tag{2.37}$$

Meaning that the transformation from U_{rad} to $U_{rad}^{'}$ is dependent on the angle θ. The energy density per unit solid angle $(U_{rad}/4\pi)$ for an isotropic radiation field with a total energy density of U_{rad} may be calculated by integrating Equation 2.39 across all possible directions:

$$U_{rad}^{'} = \frac{U_{rad}}{4\pi}\int_{\phi=0}^{2\pi}\int_{\theta=0}^{\pi}[\gamma(1 + \beta\cos\theta)]^2\sin\theta d\theta d\phi. \tag{2.38}$$

To calculate the value of this integral, use $z \equiv \cos\theta$ such that $dz = -\sin\theta d\theta$:

$$U'_{rad} = \frac{U_{rad}\gamma^2}{2}\int_{-1}^{1}(1+\beta z)^2(-1)dz = U_{rad}\gamma^2(1+\beta^2/3) \tag{2.39}$$

$$= U_{rad}\left[\gamma^2 + \frac{\gamma^2}{3} - \left(\frac{\gamma^2}{3} - \frac{\gamma^2\beta^2}{3}\right)\right] \tag{2.40}$$

$$= U_{rad}[\frac{4\gamma^2}{3} - \frac{1}{3}\gamma^2\left(1-\beta^2\right)], \tag{2.41}$$

Remember that $\gamma^2(1-\beta^2) = 1$; as a result,

$$U'_{rad} = U_{rad}\frac{4(\gamma^2 - 1/4)}{3}. \tag{2.42}$$

When substituting this for U'_{rad} in Equation 2.37, the result is

$$P = \frac{4}{3}\sigma_T c U_{rad}(\gamma^2 - 1/4), \tag{2.43}$$

which is related to the total power emitted due to the process of inverse-Compton up-scattering of photons with low energy. The source power of these photons was $\sigma_T c U_{rad}$. When photons encounter inverse-Compton scattering, the resulting radiation gains a net power of:

$$P_{IC} = \frac{4}{3}\sigma_T c U_{rad}\left(\gamma^2 - \frac{1}{4}\right) - \sigma_T c U_{rad} = \frac{4}{3}\sigma_T c U_{rad}\left(\gamma^2 - 1\right) \tag{2.44}$$

The final solution is obtained by substituting $(\gamma^2 - 1)$ by $\beta^2\gamma^2$

$$P_{IC} = \frac{4}{3}\sigma_T c\beta^2\gamma^2 U_{rad}. \tag{2.45}$$

When IC radiation losses are divided by synchrotron radiation losses, the result is remarkably simple:

$$\frac{P_{IC}}{P_{syn}} = \frac{\frac{4}{3}\sigma_T c\beta^2\gamma^2 U_{rad}}{\frac{4}{3}\sigma_T c\beta^2\gamma^2 U_B} = \frac{U_{rad}}{U_B}. \tag{2.46}$$

The energy density of radiation is proportional to IC loss, whereas the energy density of magnetism is proportional to synchrotron loss. There are no distinguishing features between the impacts of inverse-Compton and synchrotron losses since both have the same electron-energy dependency (Condon and Ransom, 2016) ($dE/dt \propto \gamma^2$). The above is only applicable within the Thomson regime. In the case of large photon energies in the electron's rest frame, it becomes imperative to take into account the quantum approach

of the Klein-Nishina regime. Despite the non-negligible recoil of the electron and its consequential energy loss upon collision, the primary outcome of the Klein-Nishina regime is a diminished scattering cross section relative to the classical value. This results in a reduced likelihood of scattering compared to the classical scenario. As a result of the rare occurrence of Klein-Nishina interactions, the inverse Compton process quantum effects are occasionally approximated by neglecting the scattering that happens in the Klein-Nishina regime, i.e., by a hard cut-off of the scattered spectrum when transitioning to the Klein-Nishina regime. For the emission modelling of blazars, it is often very important to properly take into account the Klein-Nishina regime.

The Inverse-Compton spectrum

The inverse Compton scattering spectrum is dependent on the incoming spectrum, as well as the electron energy distribution. When the observers' radiation field consists entirely of frequency ν_0 photons, the scattering caused by a single electron moving along the x-axis at ultra-relativistic velocity $+v$ is taken into consideration (see Figure 2.12). In the electron's rest frame, relativistic aberration causes most photons to approach almost head-on. It is given by the relativistic Doppler Equation that a photon coming close to the x-axis ($\theta \ll 1$) has a frequency of $\nu_0^{'}$ (Condon and Ransom, 2016) in the electron frame:

$$\nu_0^{'} = \nu_0[\gamma(1 - \beta\cos\theta)] \approx \nu_0[\gamma(1 + \beta)] \tag{2.47}$$

Photons dispersed through Thomson scattering have $\nu^{'} = \nu_0^{'}$ in the electron frame, which is the same as incident radiation. According to the relativistic Doppler formula for radiation, scattered towards the positive x-direction ($\theta \approx 0$), relativistic aberration determines the frequency ν of scattered photons and beams them in the electron's velocity direction:

$$\nu = \nu^{'}[\gamma(1 + \beta\cos\theta)] \approx \nu^{'}[\gamma(1 + \beta)] \approx \nu_0[\gamma(1 + \beta)]^2 \tag{2.48}$$

In the ultra-relativistic limit $\beta \to 1$,

$$\frac{\nu}{\nu_0} \approx 4\gamma^2, \tag{2.49}$$

in the observers' frame, this is the upscattered radiation's maximum frequency. To calculate the average energy $\langle E \rangle$ of scattered photons in an isotropic radiation field, for each electron, divide the average scattered power P_{IC} by $\dot{N}_{IC}$, the rate at which photons in the frame of the observer are dispersed per second. The rate may be calculated by dividing the power that was scattered by the energy of the photon:

$$\dot{N}_{IC} = \frac{\sigma_T c U_{rad}}{h\nu_0}. \tag{2.50}$$

Thus

$$\langle E \rangle = h\langle \nu \rangle = \frac{P_{IC}}{\dot{N}_{IC}} = \frac{4}{3}\gamma^2\beta^2\sigma_T c U_{rad}\left(\frac{h\nu_0}{\sigma_T c U_{rad}}\right) \tag{2.51}$$

where the upscattered photons have an average frequency $\langle \nu \rangle$, which is

$$\frac{\langle \nu \rangle}{\nu_0} = \frac{4}{3}\gamma^2. \tag{2.52}$$

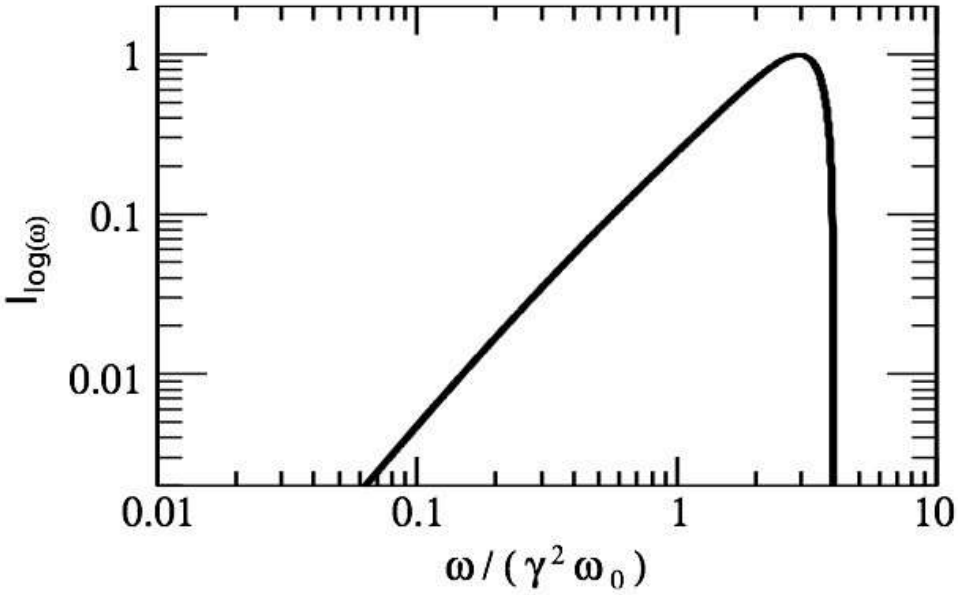

Figure 2.13: The inverse Compton spectrum produced by scattered photons with frequency ω_0 by electrons with energy γ. (Credit: Condon and Ransom 2016).

The spectra resulting from the process of Inverse Compton exhibit power law behaviour, where the spectral index is determined by the electron energy distribution, which follows a power law of the form $n(E) \propto E^{-\delta}$:

$$\alpha = \frac{\delta - 1}{2}. \tag{2.53}$$

This means that the inverse-Compton and synchrotron radiation in the Thomson regime will have the same spectral index. This is true for mono-energetic electron distributions, but if the photon field is not, this also changes the shape of the resulting spectrum.

2.3 AGN Multi-wavelength Study

A comprehensive multi-wavelength approach is necessary to understand the physics of AGNs and their interaction with the intergalactic medium. Figure 2.14 shows multi-

wavelength images of NGC 5128, which is a radio-loud AGN that shows jet-mode radio-loud emission. The AGN emits electromagnetic radiation with wavelengths ranging from radio to gamma rays. X-rays are emitted by the accretion disk, corona, and jets of an AGN. The dusty structure surrounding the AGN absorbs the optical and UV continuum light emitted by the accretion disk. The structure that causes obscuration has the ability to transform the energy emanating from optical and ultraviolet photons so that they can be re-radiated at mid-infrared wavelengths.

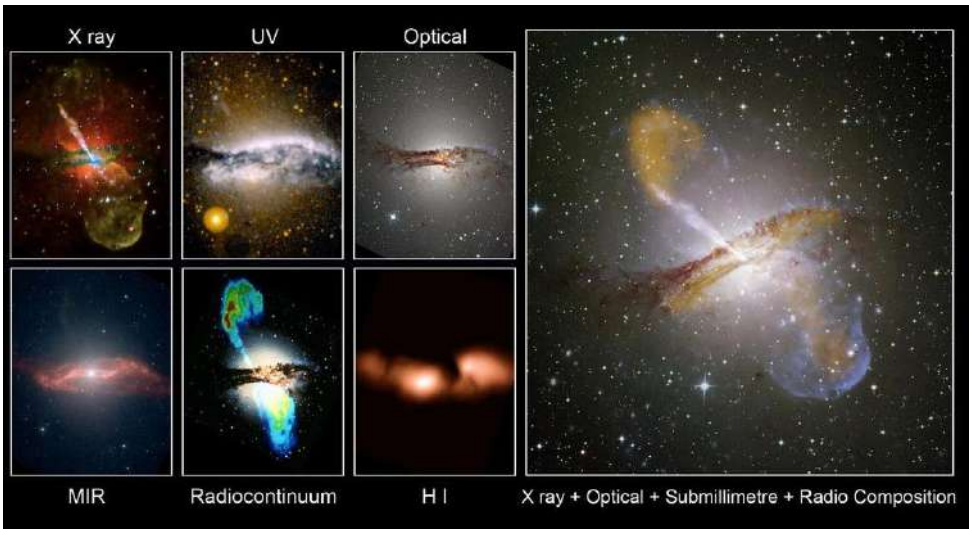

Figure 2.14: The multi-wavelength picture of Centaurus A, a radio-loud AGN, illustrates how a multi-wavelength study might be advantageous when studying AGN. (Credit: ©2014 Ángel R. López-Sánchez).

2.3.1 Spectral Energy Distribution (SED)

The SEDs of jetted AGN are dominated by non-thermal continuum spectra. The majority of radio-loud AGNs exhibit a broadband SED that matches the distinctive double-hump shape, as illustrated in Figure 2.15. The first peak appears within the frequency range spanning from millimetre to soft X-ray (depending on the specific category of blazar), whereas the second peak appears at gamma-ray frequencies, within the energy range of MeV-TeV. The synchrotron process generates the initial hump, while the subsequent hump is due to the ICS of either the photons from synchrotron emission (SSC) or external to the jet (EC) (Diltz and Boettcher, 2016), and there are also hadronic models to explain the gamma-ray emission. The accretion disk (Dermer et al., 1992), the dusty torus (Tavecchio et al., 2011), the broad line region (Sikora et al., 1994), or a relatively slow sheath enveloping the jet (Marscher et al., 2010) are all possible sources of the external photon field. AGN spectral energy distributions are a critical tool for understanding the physical processes of particle acceleration and multi-wavelength emission.

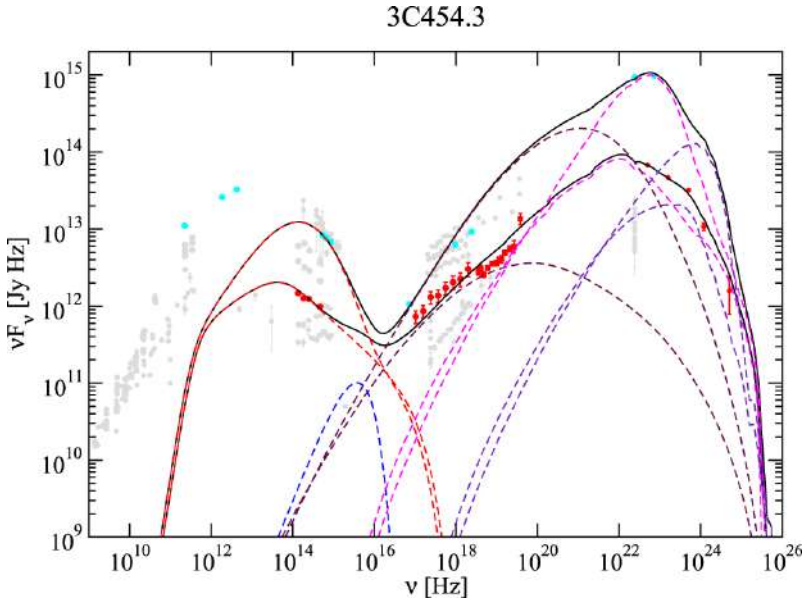

Figure 2.15: The broadband SED of 3C 454.3 fitted using the leptonic model for both its quiescent and flaring phases. The archival data points are grey, and the quiescent phase ones are red; the Cyan points represent broadband data from the flare of 19-20 November 2010. The solid black line represents the total spectrum; the blue dashed line represents thermal emission from the accretion disk; the indigo dashed line represents external EC emission from the BLR; the red dashed line represents synchrotron emission from electrons/positrons; the maroon dashed line represents SCC emission; and the magenta dashed line represents the emission produced by external comptonization (EC) originating from the accretion disk. (Credit: Diltz and Boettcher 2016).

Chapter 3

Interferometry, Observations and Data Reduction

This chapter provides a brief overview of radio interferometry and describes the MeerKAT radio telescope and how it operates in detail. The procedure followed to reduce the data and the archives used to accumulate the multi-wavelength data are summarised in this chapter.

3.1 Basics of radio interferometry

3.1.1 How Radio Telescopes Work: A Brief Overview

Radio telescopes may be used as either a single dish or a group of telescopes (Ryle et al., 1959). Different types of radio telescopes can be distinguished from one another based on the optimisation for observation frequencies, the sort of radio emissions they can concentrate on, the types of reflectors used, and the mounts to which they are affixed. Equatorial and altitude-azimuth configurations are two types of mounts for telescopes (Condon and Ransom, 2016). Every single-dish radio telescope has the following standard components:

- A reflector dish,
- a receiver system,
- a back-end system for voltage detection and correlation, and
- a computer system for data collection and storage.

Dish

A radio telescope's dish also called the aperture (D), has a reflecting material or composite collecting surface area (A_e) that is used to detect radio waves (Foley et al., 2016). The most common shape of a dish telescope is a parabola, however, other shapes do exist. Radio telescopes use radio wave focusing devices with reflectors based on Prime Focus, Cassegrain, or Gregorian reflector designs. There are two reflectors in a Cassegrain or offset Gregorian design. Each of these telescope designs is equipped with both a primary and secondary reflector. Cassegrain secondary reflectors have a hyperbolic convex surface, whereas Gregorian secondary reflectors have an ellipsoid concave surface. Rather than relying on a secondary reflector, the Prime focus design has a receiver stationed at the main reflector's focal point. Figure 3.1 illustrates the three mentioned telescope designs.

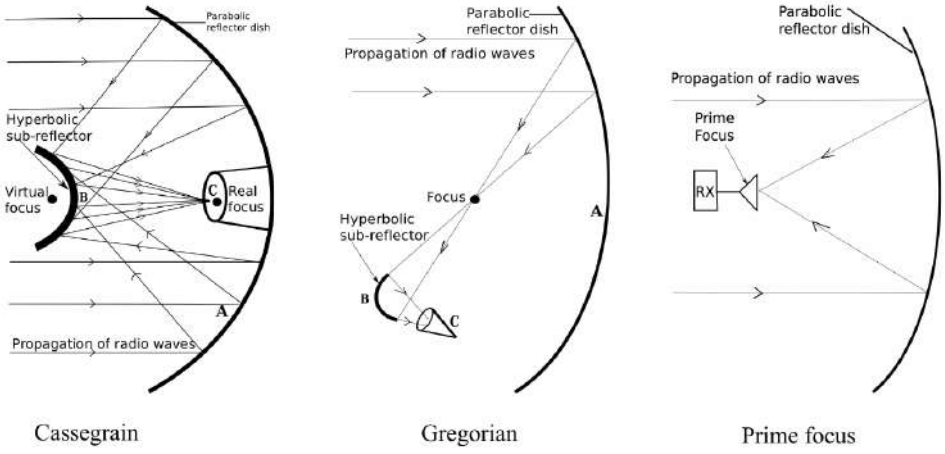

Figure 3.1: An illustration of the different configurations of antenna reflectors. (Credit: Seidu 2020.

Receivers

There are back-end and front-end receiver systems in a radio telescope. Feeds, interconnecting cables, mixers, and amplifiers make up the components of a conventional front-end system. The feed is a channel via which the signals collected by the secondary reflector are transferred to the receiver for efficient transmission through the wave-guide cable. The radio signals are modulated into a wave-guide mode by the feed. Splitters, also known as orthomode transducers (OMT), are devices that split a signal into two channels with opposite polarities. In the mixers, a local oscillator (LO) is used to combine the radio signals, which results in the conversion of polarised signals into signals at intermediate frequencies (IF). By converting the signal's frequency, we may reduce the amount of signal loss in transmission and control it more readily at the receiving end. The signal at the new frequency is amplified by an IF amplifier before it is filtered and down-converted. The front end is often cooled to prevent noise from being introduced to the signal outputs.

In a single-dish radio telescope, the detector, spectrometer, or radiometer are the components that make up the receiver back-ends. The noise power response per frequency bandwidth ($\Delta\nu$) is generated by a square-law detector, which is related to the temperature of the system. The spectrometer comprises a single side-band receiver that captures data related to the spectral lines. The spectrometer generates a spectrum based on observations of spectral lines, with the total power in each frequency range quantified. The radiometer operates as a square-law detector and averages across a broad frequency range, making it ideal for continuum measurements.

Measuring radio signals

A radio source generates signal power (P) that is spread out over a frequency bandwidth ($\Delta\nu$). The equation for the signal that the antenna receives from the source, as stated by the Nyquist theorem, is as follows:

$$P_\nu = kT\Delta\nu \tag{3.1}$$

where k is the Boltzmann constant and T is the temperature. Among the many characteristics of radio telescopes, the effective collecting area (A_e) of the dish is crucial (Thompson et al., 2017). The term "antenna efficiency" refers to the proportion of power received by the effective area of a dish from a radio-emitting field in relation to the total area of the dish. When the reflector surface is not constructed properly, some of the signals may be "lost". In addition, the parabola's form ensures that radio waves won't be reflected into the receiver unless the shape is imperfect. The source beam is defined as the solid angle (Ω) that is encompassed by a radio-emitting source with a constant brightness temperature T_B. Moreover, the antenna has a beam angle (θ) that is either equal to or less than the magnitude of the power being emitted from the radio frequency signal. An antenna's main radiation pattern depends on its power output from the source's focal point. When the emissions from a source are measured in directions other than the primary lobe, the results are referred to as side lobes. The antenna's beam width, measured in wavelengths, is inversely proportional to the aperture size.

The overall output power that is measured by a radio telescope includes the noise emanating from both the telescope's electronic components and its surrounding environment. The summation of all the noise sources is referred to as the system temperature and is mathematically represented as:

$$T_{sys} = T_{CMB} + T_{loss} + T_{atm} + T_{cal} + T_{spill} + T_R \tag{3.2}$$

the noise contribution that is produced by the cosmic microwave background (CMB)

is given by T_{CMB}, T_{cal} represents the amount of noise that is contributed by the noise diode's injected noise, T_R represents the receiver temperature, T_{loss} represents the noise contribution due to the feed loss, T_{atm} represents the noise contribution from atmospheric effect, and the spillover temperature, T_{spill}, is the noise contribution of ground radiation being scattered into the feed-horn and radiation from the sun. Wrobel and Walker (1999) define System Equivalent Flux Density (SEFD) as the flux density a source would give at the same power, and this is the unit that may be used to quantify the system temperature. A notation for the SEFD is

$$SEFD = \frac{2\eta T_{sys}}{A_e} \tag{3.3}$$

where η is the antenna efficiency. The factor of 2 corresponds to half of the total signal detected by a single polarisation of the receiver originating from an unpolarised source. Moving the telescope from on the source to off the source with a given flux density, an observer may estimate the SEFD by measuring the fractional increase in power.

Antenna temperature (T_A) is the amount of signal power received by the antenna from the source. In Equation 3.1, the power is related as:

$$T_A = \frac{P_\nu}{k} = \frac{A_e S_\nu}{2k} \tag{3.4}$$

In general, any source's emission flux can be expressed as:

$$S[Jy] = \frac{kT_A}{A_e} \times 10^{-26}[\mathrm{WHz^{-1}m^{-2}}] \tag{3.5}$$

According to equation 3.5, the antenna temperature (T_A) is directly proportional to the source flux density. In the case of an unresolved source, defined as one whose footprint spans across a relatively small solid angle ($d\Omega$), the proportionality between T_A and T_B is adjusted by a beam-filling factor. The beam-filling factor quantifies the proportion of the source's angular size relative to the telescope's beam size (Wrobel and Walker, 1999).

3.1.2 Radio Interferometry

A radio interferometer refers to a collection of radio antennas or "elements" that are simultaneously utilized for astronomical observations, thereby imitating the function of a single telescope with a significantly large aperture. The maximum size of the radio interferometer telescope is equivalent to the maximum distance or baseline separating any two of its constituent elements. The large aperture is synthesised and selectively sampled only in the areas where an element is detected. The synthesised aperture's size determines the array's resolution, or "beam size." Rohlfs and Wilson (2013) and Thompson et al. (2017)

are used for this summary of interferometry.

Due to material constraints, the angular resolution of single-dish telescopes is typically on the order of $\theta \sim \frac{\lambda}{D}$, where λ is the wavelength of the light received, and D is the diameter of the dish. An increasing diameter for wavelength, λ, will induce improved angular resolution, and the output of two telescope dishes combined logically will achieve this (Rohlfs and Wilson, 2013). Each telescope dish has a diameter of d, and there is a distance between them of D, where d is less than D.

3.1.3 Two element interferometer

Early interferometric methods were studied by Michelson and Pease in the 1890s when they researched the employment of two separate optical elements to attain greater angular resolution ($\theta = \lambda/B$). Using two dipole antenna arrays operating at 175 MHz with a maximum baseline separation of 240 metres, Ryle and Vonberg subsequently transferred this technology to the radio domain in 1946. As a result, enormous interferometers like The Atacama Large Millimetre Array (ALMA), which has 66 elements with a maximum diameter of 12 m, have been built and can be spaced up to 14 km apart from each other (Thompson et al., 2017).

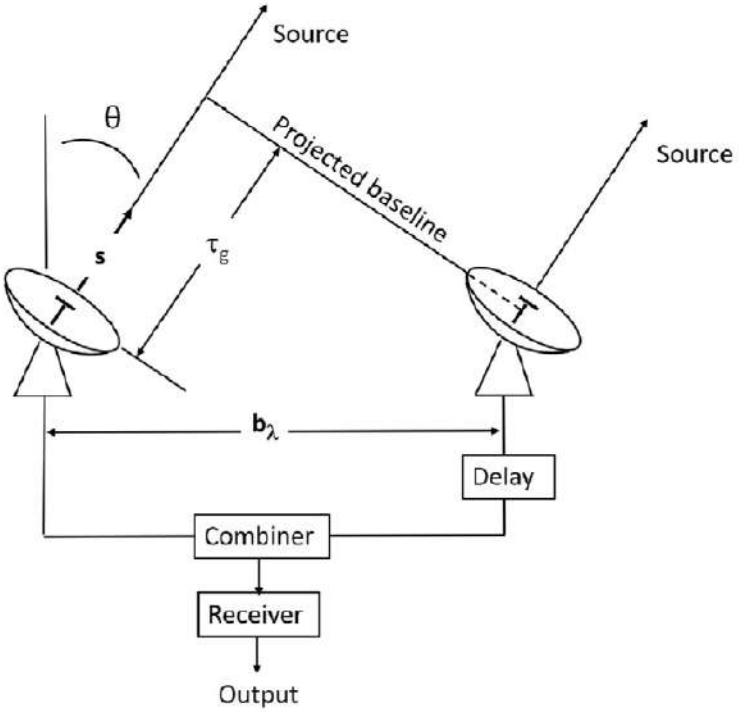

Figure 3.2: The two-element interferometer's geometrical features. The delay circuit in the receiver compensates for the geometric path delay τ_g and is capable of introducing an additional delay τ_i. The received emissions are assumed to be plane waves since the source is supposed to be far-field. It is also classified as a single-point source, which means that it is located on one plane. (Credit: Burke et al. 2019).

In Figure 3.2, the two fixed antennas receive signals which are subsequently combined, amplified, and detected by a radio receiver. The resulting total power is then expressed as a function of time. The baseline vector $\mathbf{b}_\lambda$ (wavelengths) or $\mathbf{b}$ (metres) connects the two antennas' phase centres, and the direction of the radio source is indicated by the unit vector $\mathbf{s}$ (Burke et al., 2019). The projected baseline is the projection of $\mathbf{b}$ perpendicular to $\mathbf{s}$, with length $b\cos\theta$. The difference in path length existing between the signal's arrival to the reference antenna and at the other is represented by the projection along $\mathbf{s}$ (Burke et al., 2019). The difference in length of the physical path is:

$$\Delta l_g = \mathbf{b} \cdot \mathbf{s} = b \sin\theta \text{ (metres)} \tag{3.6}$$

and the phase difference between the two signals is expressed as:

$$\phi = 2\pi\nu\tau_g = 2\pi\mathbf{b}_\lambda \sin\theta \text{ (radians)} \tag{3.7}$$

The two signals, represented as voltages, are added together in the receiver, followed by square-law detection and time averaging. V_A and V_B represent the two signal voltages, and V_{rec} represents the receiver-generated noise voltage. The receiver's R_{A+B} output is determined by the equation:

$$R_{A+B}(\tau_g) = \langle [V_A \cos\omega t + V_B \cos\omega(t-\tau_g) + V_{rec}]^2 \rangle \tag{3.8}$$

Because the average time of $\langle \cos^2(\omega t) \rangle = 1/2$, only the following is left:

$$R_{A+B}(\tau_g) = \frac{1}{2}[(V_A^2 + V_B^2) + V_{rec}^2] + \langle V_A V_B \cos\omega\tau_g \rangle \tag{3.9}$$

As the receiver gain fluctuates, so does the output stability. These output variations may be equal to or greater than the interference term. Gain variations in total power terms may not be an issue for all applications in astronomy (such as pulsars and other time-varying sources). For long-term integration of weak sources, however, cross-correlation is always used, which eliminates the total-power terms (Burke et al., 2019).

The average of the two amplitudes over time, with one of them being time-delayed by τ, is the definition of the cross-correlation $R_{xy}(\tau)$ of the two amplitudes $x(t)$ and $y(t)$. This is expressed as:

$$R_{xy}(\tau) \equiv \langle x(t) y(t-\tau) \rangle \tag{3.10}$$

The correlation between the voltages of the two fundamental signals is,

$$R_{AB}(\tau_g) = \langle V_A \cos \omega t V_B \cos \omega (t - \tau_g) \rangle \tag{3.11}$$

or alternatively

$$R_{AB}(\tau_g) = \langle \frac{1}{2} V_A V_B \cos \omega \tau_g \rangle \tag{3.12}$$

Recognising the effective antenna area $A(\mathbf{s})$ direction-dependent in actual interferometers is a first step in understanding antenna performance (Burke et al., 2019). The point source specific flux density, S_ν, and antenna pair-effective area, $A(\mathbf{s}) = \sqrt{A_1(\mathbf{s})A_2(\mathbf{s})}$, are used to generate the cross-correlation. Therefore, the cross-correlation can be expressed as:

$$R_{AB}(\tau_g) = A(\mathbf{s}) S_\nu \cos \omega \tau_g = A(\mathbf{s}) S_\nu \cos (\omega \mathbf{b} \cdot \mathbf{s}/c) \tag{3.13}$$

or alternatively,

$$R_{AB}(\tau_g) = A(\mathbf{s}) S_\nu \cos (2\pi \mathbf{b}_\lambda \cdot \mathbf{s}) \tag{3.14}$$

3.1.4 Fourier Synthesis Imaging

The production of cross-correlating voltages at the correlator interference patterns may be affected using two or more telescopes. A spatial coherence, known as complex visibilities, is created when voltages at various locations are cross-correlated with one another. Amplitude and phase are two elements that make up the visibilities.

The Fourier transform (FT) establishes a correlation between the observed interference pattern and the radio intensity in the sky. The Fourier domain (u, v) is estimated using interferometers rather than the image domain (x, y). The observed sky brightness distribution $(T(x, y))$ is apparent from the observed visibilities $(V(u, v))$ via sampling in Fourier space. $T(x, y)$ represents the two-dimensional Fourier transform of $V(u, v)$ (Thompson et al., 2017). The theorem of van Cittert-Zernike postulates that Fourier transform of visibility as a function of baseline coordinates (u, v) is the distribution of sky brightness as a function of sky coordinates (x, y). The function of complex visibility is:

$$V(u, v) = \iint T(x, y) e^{2\pi i (ux + vy)} dx dy \tag{3.15}$$

and the distribution of sky brightness is defined as:

$$T(x,y) = \iint V(u,v)e^{-2\pi i(ux+vy)}dudv \tag{3.16}$$

Using the convolution theorem,

$$D(x,y) * T(x,y) = B^d(x,y), \tag{3.17}$$

this is; dirty beam $*$ true sky $=$ dirty image. A dirty image is created by convolving the dirty beam point spread function with the sky intensity distribution of the source. To reconstruct the image of the distribution of sky brightness, the deconvolution method must be used which is a procedure that removes the dirty beam from the synthesised image to obtain not only smoothness but also an accurate representation of the true sky.

3.2 MeerKAT Radio Telescope

The MeerKAT radio telescope is a precursor to the mid-frequency radio telescope known as the Square Kilometre Array (SKA). Its approximate coordinates are $21°26'$ East, $30°42'$ South, making it a part of the Karoo area of the Northern Cape Province in South Africa. Before the SKA is complete, MeerKAT will continue to hold the title of the most sensitive and largest radio telescope in the Southern Hemisphere. SKA1-MID will include MeerKATs radio telescope antennas, receiver, and digitiser after the larger array's construction phase is complete. This means that the MeerKAT array core will serve as the geographic centre of the SKA1-mid array and that the MeerKAT antennas will provide a significant proportion of the SKA1-mid aperture inside the core (Booth et al., 2009). MeerKAT consists of 64 Gregorian-offset antennas; each antenna has a diameter of 13.5 m, and 48 antennas are concentrated in the core area of the array, with a radius that is roughly 1 km, and the remaining 16 antennas are scattered outward over an area of up to 8 kilometres around the core. The MeerKAT array's shortest and longest baselines are 29 metres and 8 kilometres, respectively. For maximum efficiency, each antenna is equipped with four cryogenic receiver systems that operate in different radio wavelength bands, the remainder are spread over a radius of 4 km, see Figure 3.3. The MeerKAT receptors are determined by the scientific goals of the telescope. The MeerKAT telescope was inaugurated on 13 July 2018 (Jonas and MeerKAT Team, 2016).

3.2.1 How MeerKAT Operates

MeerKAT now supports polarisation, transient searches, pulsar timing, spectral line imaging, deep continuum, and other observational modalities. Numerous 'data spigots' are available to provide data to various instruments, and several standard data outputs are

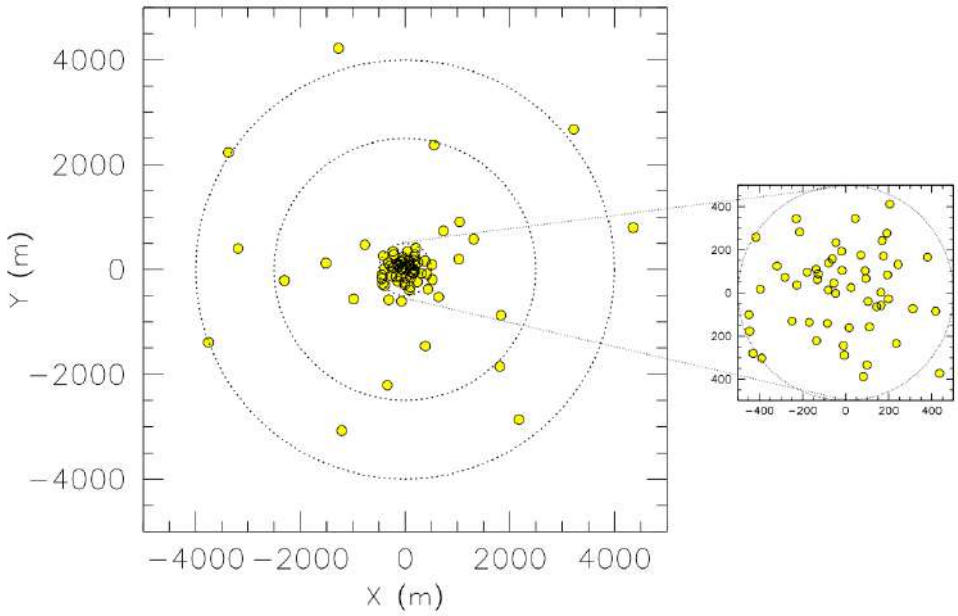

Figure 3.3: Full overview of the 64 MeerKAT antennas distributed in two components. The innermost part consists of 48 antennas, and it employs a 2-D Gaussian *uv*-distribution characterized by a maximum baseline of 1 km and a dispersion of 300 m. The outer part, which has 16 antennas, follows a Gaussian *uv*-distribution with a 2.5 km dispersion. (Credit: Booth et al. 2009).

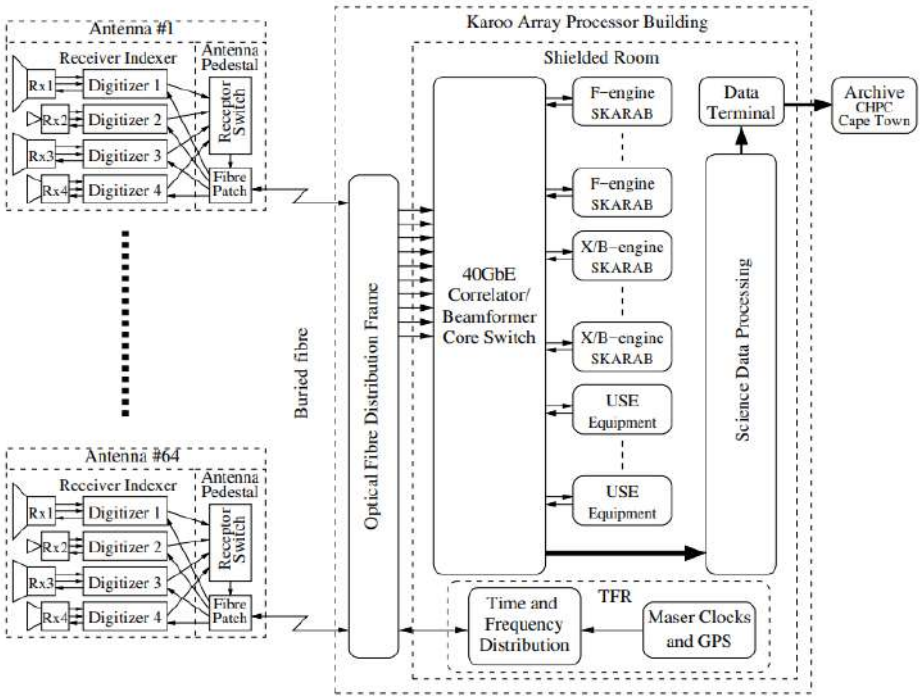

Figure 3.4: MeerKAT's overall signal transport and data processing architecture appears in this figure, which includes an analogue and digital signal channel, the digitisers, the correlator/beamformer, the scientific data processing (SDP) subsystem, and the time and frequency reference (TFR) subsystem. (Credit: Jonas and MeerKAT Team 2016).

provided as well, such as an imaging pipeline (Booth et al., 2009; Jonas and MeerKAT Team, 2016). The three major MeerKAT receptor components are:

1. antenna positioner (for a dish-shaped antenna mounted on a pedestal),
2. a variety of radio receivers, and
3. the digitisers associated with them.

The antenna performs real-time digitisation of the receiver outputs, and underground optical fibres transfer the resulting digital data streams to the Karoo Array Processor Building (KAPB) (see Figure 3.4). The Correlator/Beamformer (CBF) digital signal processor is responsible for processing the antenna signals (Jonas and MeerKAT Team, 2016). The CBF data is transferred to the Science Processor computer cluster and disk storage modules, which use it to analyse and process the data. In addition, the CBF makes the MeerKAT antenna's data accessible to user-supplied computer back-ends, such as a precision pulsar timing system, a search for extraterrestrial intelligence (SETI) signal processor, and a search for pulsars and fast radio bursts (FRBs). The digitisers and other parts of the telescope rely on clock and absolute time signals provided by a time and frequency reference (TFR) system (Jonas and MeerKAT Team, 2016). The TFR system utilises two hydrogen maser clocks, two rubidium atomic clocks, a precision crystal oscillator, and an array of Global Navigation Satellite System (GNSS) receiver devices to synchronise with Coordinated Universal Time (UTC).

3.2.2 Receptors for the MeerKAT L Band

Receiving electromagnetic radiation and converting it to a voltage signal is the principal function of the receiver. The voltage signal is amplified by a cryogenic receiver, which may introduce some noise into the signal. In order to operate, the first two receivers must have a sensitivity of around 220 m^2/K (> 300 m^2/K is attainable) in the L band (900-1670 MHz). Each element of the MeerKAT L band antenna, including the main reflector, sub-reflector, feed horns, cryogenically cooled receiver, digitisers located atop the feed indexer, and driving system, is part of the pedestal-based receiver (Jonas and MeerKAT Team, 2016). Under optimal conditions, a run-time of 20 minutes for MeerKAT yields a pointing precision of $5''$, and normal condition has a run-time of 24 hours and provides a pointing accuracy of $25''$. In the case of L-band receivers, the crossed-dipole Ortho-mode Transducer (OMT) operates at a temperature of approximately 90 K.

The receiver indexer has digitisers, one positioned adjacent to each of the four receivers. The radio frequency (RF) voltage signal is converted into electrical circuits using the four digitisers. For instance, a shielded digitiser package located $\sim$ 1m from an L band receiver receives the RF signal through coaxial cables. The signal is sampled directly in the Nyquist zone rather than converted to a heterodyne receiver by the digitiser. An

analogue-to-digital converter (ADC) is used to do the sampling. One horizontal and vertical polarisation provides a 10-bit voltage that is then packed in 4×10 Gbps transmission channels through subterraneous optical fibre cables to the correlator housed inside the KAPB at the Losberg location.

3.3 MeerKAT Observations and Data Reduction

Multi-epoch observations of the Fast Radio Burst (FRB) fields were carried out with the MeerKAT telescope (the Meer TRAnsients and Pulsars[1] (MeerTRAP) project, project ID: SCI-20190418-VC-01) at L-band receiver (856–1712 MHz), which operates with a 1.28 GHz central frequency and has a native bandwidth of 856 MHz. Each FRB target had 90 minutes of on-source integration time, and a phase calibrator was observed for 2 minutes for every 15 minutes on the target FRB (Chibueze et al., 2022). The Band-pass and flux calibrators were J1939-6342 and J0408-6545, and the phase calibrators were J1619-8418, J1215-1731, and J2225-0457 (observed for 5 minutes at the beginning and end of the observations). A frequency resolution of $\sim$ 209 kHz was achieved by using the SKARAB correlator in its 4k mode to do the data correlation. This mode provides 4096 channels spread out throughout the 856 MHz bandwidth. Table 3.1 summarises the details of the MeerKAT observations (Chibueze et al., 2022).

Field name	Observation date	α_{J2000}	δ_{J2000}	Synthesised beam	rms (μJybeam^{-1}
FRB 20171019A	18 October 2019	$22^h17^m32^s.00$	$-08°39'32''.0$	$6''.8$ x $5''.0$	5.2
FRB 20190711A	09 September 2019	$21^h56^m00^s.00$	$-80°23'00''.0$	$12''.5$ x $4''.9$	4.6
FRB 20190714A	28 September 2019	$12^h15^m00^s.02$	$-13°00'00''.0$	$6''.5$ x $5''.1$	5.8

Table 3.1: Summary of the MeerKAT observations of the FRB fields used for this study (Chibueze et al., 2022).

3.3.1 Oxkat

Data for this research was reduced and processed using OXKAT[2] software (Heywood, 2020), with each epoch being treated independently. The oxkat reduction pipeline is a Python-based, semi-automated tool for processing MeerKAT data, presently optimised for L-band continuum observations. At present, the oxkat pipeline operates completely automatically until the step of direction-independent self-calibration and imaging, which is also referred to as "second generation calibration" or "2GC". The following tasks are those that were executed to reduce the data for this thesis:

[1] https://www.meertrap.org/
[2] https://github.com/IanHeywood/oxkatv0.1

1GC: Cross-calibration and initial imaging

All cross-calibration processes, which involved correcting the target phases and amplitudes with known calibrator sources, are done in CASA (McMullin et al., 2007). The target fields, target-secondary pairs, and primary calibrator, as well as a secondary calibrator, are identified after averaging the data over 1024 channels and interrogating the field list. The running of the BANDPASS and GAINCAL tasks within the CASA software yielded solutions for bandpass and delay (per scan), as well as amplitude and phase corrections for complex gain that remained unaffected by frequency (per-integration time). Antennas that were not working well were also flagged initially, in addition to the frequency bands that are known to be contaminated by RFI (there were $\sim 40\%$ of the original bandwidth dominated by satellite RFI). Upon correction of the target fields using primary and secondary calibrator models, the resulting calibrated target fields were partitioned into separate measurement sets.

Automatic flagging is performed on the corrected target data before imaging using WSClean, utilising the auto-masking and multi-frequency tools with a Briggs' weighting of -0.3 (Offringa and Smirnov, 2017). This weighting achieves the optimal balance between noise sensitivity and angular resolution with a synthesised beam of ~ 8 arcsecs.

FLAG: Flagging

Flagging involves marking on each baseline to indicate the position of the Galactic neutral hydrogen line, which falls within the frequency range of 1419.8 MHz to 1421.3 MHz, as well as the low-gain band-pass edges spanning from 856 MHz to 880 MHz and 1658 MHz to 1800 MHz (Chibueze et al., 2022). On baselines shorter than 600 metres, many more areas of the spectrum are susceptible to RFI than are marked. The calibration procedures of TFCROP and RFLAG in CASA, along with the TRICOLOUR package for the target fields, were used to filter out any remaining data that could have been affected by RFI (Chibueze et al., 2022). This process ensures that only data that has not been impacted by RFI is displayed.

2GC: Self-calibration

The CASA and WSClean (Offringa et al., 2014) are used to iteratively enhance the calibration of the target visibilities for self-calibration. Re-imaging the corrected data with the original mask utilised for 1GC target imaging is essential as it provides guidance to the software on the location of actual emission, thereby significantly improving image resolution. During re-imaging, a target sky model is inevitable once the mask is modified. When the target data is self-calibrated, the CASA software utilizes the sky model to generate a series of calibration solutions that are unidirectional and based on the phase centre of the dataset. Therefore, the data that has been corrected by the 2GC process is subjected to

re-imaging, and subsequently, the sky and mask models are updated.

The WSClean image (Offringa et al., 2014) was used to deconvolve and image the target data. Both the wide-band and multi-scale deconvolution techniques were enabled to enhance the efficacy of imaging the diffuse emission that was observed in the fields. The process of deconvolution was performed in eight sub-band images per epoch, each having central frequencies of 909, 1016, 1123, 1230, 1337, 1444, 1551, and 1658 MHz. The multi-frequency synthesis (MFS) map is generated by WSClean utilizing the deconvolution mode of a joined channel and a centre frequency of 1283 MHz. To generate a model of the target field that is free of self-calibration artefacts using WSClean, each sub-band is deconvolved individually using an initially high mask of 20σ rms (using the auto masking function that WSClean gives). In the last cycle of imaging, this masking threshold was repeatedly decreased until it reached a value of 3σ rms. The oxkat pipeline utilises the conventional tasks provided by the Cubical program for self-calibration (Kenyon et al., 2018).

3.4 Archival catalogues

Observational data used to produce the full spectral energy distribution were gathered from many telescopes, both space and ground-based. The following sections summarise the locations, energy ranges, and key features of each telescope and appears in order of increasing detection energy.

The NRAO VLA Sky Survey (NVSS)

The NVSS has provided coverage of 82% of the celestial sphere from the North of J2000.0 declination = $-40°$ at a frequency of 1.4 GHz (Condon et al., 1998). The Very Large Array (VLA) and the Expanded Very Large Array (EVLA) have both been carrying out simultaneous observations of a subset of sources since the spring of 2010. The majority of the EVLA and VLA runs were completed in blocks of time ranging from one to two hours. The images have an almost uniform sensitivity and a full width at half maximum (FWHM) angular resolution of 45 arcseconds (Condon et al., 1998).

The integration time at 4.86 GHz and 8.46 GHz was around 30 seconds; at 22.46 GHz, it was around 100 seconds; and at 43.34 GHz, it was around 120 seconds. The standard NRAO software (AIPS or CASA) are used to flag, calibrate, and image the *uv* data, and all flux density measurements were calibrated using reference values from either the 3C 48 or 3C 286 calibrator sources. During the several months of observation, the EVLA and VLA were in different configurations. Thus, for a certain setup, higher frequencies resulted in a significantly higher angular resolution. Because of this, all sources that seemed resolved in any VLA frequency or configuration were carefully flagged (Condon et al., 1998).

The Wide-field Infrared Survey Explorer (WISE)

The WISE is NASA medium-class explorer mission that surveyed the entire sky in four varying micrometre bands (3.4, 4.6, 12 and 22 microns) to obtain precise digital images. WISE is proficient at reaching 5σ point source sensitivities that surpass 0.08, 0.11, 1, and 6 mJy across all four different micrometre bands (Chen et al., 2018).

On 14 January 2010, after WISE's launch on 14 December 2009, the survey officially began. The data outputs from WISE consist of a calibrated digital atlas of coadded images in the four survey bands, as well as a source catalogue detailing the locations and radii of the objects observed in the atlas. Ancillary data products include the individual single-exposure images coadded to form the image Atlas and a working database of sources extracted from the single-exposure images. The WISE preliminary data release was made available on 14 April 2011 (Wright et al., 2010) and covered approximately 57% of the sky (Chen et al., 2018).

Two Micron All Sky Survey (2MASS)

The 2MASS Point Source catalogue was the result of a collaboration between the Infrared Processing and Analysis Centre and the University of Massachusetts. This project received funding from the National Science Foundation and The National Aeronautics and Space Administration. Through the accumulation of 7.8 seconds of integration time for every point in the sky and the implementation of rigorous quality control measures, a point-source detection level of 10σ was achieved. This level was found to be better than 15.8, 15.1, and 14.3 magnitudes at the J, H, K_s bands, respectively, for almost the entire sky (Skrutskie et al., 2006).

Two fully automated 1.3-metre telescopes were used for the 2MASS study. One of these telescopes was located at the northern facility at Mt. Hopkins, Arizona, while the other was located at the southern facility in CTIO, Chile. The telescopes are equipped with a three-channel camera, wherein each channel comprises a 256×256 array of HgCdTe detectors, and have the capability to simultaneously observe the sky at J (1.25 μm), H (1.65 μm), and K_s (2.17 μm) wavelength bands (Wang et al., 2008).

Sloan Digital Sky Survey (SDSS)

The SDSS is a significant survey that employs spectroscopic redshift and multi-spectral imaging techniques. This survey was carried out at the Apache Point Observatory, located in New Mexico, USA. The survey employs a specialized optical telescope with a 2.5-m wide-angle. The process of gathering data commenced in the year 2000. The ultimate imaging data release, known as DR9, encompasses over 35% of the sky and comprises photometric observations of almost 1 billion sources. Furthermore, the survey has contin-

uously obtained spectra and has thus far recorded spectra of over four million sources. A photometric system comprising a set of five different filters, namely the u, g, r, i, and z filters, is made use of to obtain the images. The processing of the images has resulted in the accumulation of lists of objects detected as well as numerous characteristics, such as whether the objects seem point-like or elongated (Gunn et al., 2006).

The inclusion of the Southern Hemisphere in the fourth phase of the SDSS marked the commencement of its first observations in this region. The southern observations are conducted using the Irénée du Pont Telescope located at the Las Campanas Observatory, situated in the northern region of Chile (Bowen and Vaughan, 1973).

Second XMM-Newton X-ray source catalogue (2XMM)

The 2XMM is a catalogue of incidental X-ray sources from the XMM-Newton observatory of the European Space Agency (ESA). The compilation of the ESA was carried out by the XMM-Newton Survey Science Centre (SSC). In July 2006, the pre-release version of the 2XMMp catalogue was made accessible to the general public and was simply a subset of the whole 2XMM catalogue. Astronomical objects such as active galaxies, galaxy clusters, interacting compact binaries, and active stellar corona are all sampled from the 2XMM catalogue. As a result, 2XMM is an excellent tool for discovering and cataloguing unusual X-ray source populations because of its extensive coverage of the sky (Watson et al., 2009).

Catalogue detections have a median flux (encompassing the photon-energy range of 0.2 - 12 keV) of around 2.5×10^{-14} erg cm^{-2} s^{-1}. In the soft energy band of 0.2 - 2 keV and the hard energy band of 2.5 - 12 keV, the median flux is roughly 5.8×10^{-15} erg cm^{-2} s^{-1} and 5.8×10^{-15} erg cm^{-2} s^{-1}, respectively. Fluxes below 1×10^{-14} erg cm^{-2} s^{-1} are found in around 20% of the sources. The catalogue detections normally have a positional precision of 5 arcseconds (confidence radius of 99 percent). Overall, the flux measurements from the three European Photon Imaging Camera (EPIC) cameras are within 10% of one another in most energy bands (Watson et al., 2009).

Fermi Large Area Telescope (LAT) 10-year Source Catalog (4FGL)

The Fermi Large Area Telescope, which was launched in June 2008, is a pair-conversion telescope that is designed to detect gamma rays above 20 MeV. The telescope's detector works by measuring the path and kinetic energy of the electron-positron pairs that are produced by gamma rays that enter the detector. The Fermi-LAT is comprised of a silicon micro-strip tracker, an electromagnetic calorimeter with a CsI hodoscope, and an anti-coincidence detector used to reject signals produced by background charged particles (Abdollahi et al., 2020). The wide Field of View (FoV) of the LAT, which is around 2.7 steradians, enables it to conduct a comprehensive survey of the whole sky in intervals of three hours. The 4FGL catalogue contains 5064 sources with a significance of at least 4σ,

and the location and spectral features of these sources are reported.

3.5 Spectral Energy Distribution model

The single-zone leptonic model of Böttcher et al. (2013) was used to model the SEDs. Although the data is not perfectly simultaneous, it is worth noting that the majority of the observations have integration times that exceed typical time scales for radiative cooling and the dynamic of electrons (and protons) that emit in the radio to gamma-ray ranges. This steady-state model is therefore acceptable for the objective of this thesis and it incorporates synchrotron emission and Compton scattering (SSC). The model assumes a single emission zone which has a spherical shape in the co-moving reference frame and is propelled along the jet with the Lorentz factor denoted as Γ_{jet}. Electron injection is performed with a distribution of energy that follows a power-law model. A state of self-consistent equilibrium is established by taking into account the interplay between electron injection, radiative energy losses, and the time required for the electrons to escape from the emission zone. This equilibrium state is then used to determine the final radiation spectrum. The scale of the time it takes for particles to escape the emission zone is quantified as a multiple of the time taken by light to cross the emission region by a factor of $\eta_{esc} \geqslant 1$, with the result that $t_{esc} = \eta_{esc} R/c$, where R is the radius of the emission region.

Chapter 4

Results: MKAT J221834.96-082253.50

The results of this study are presented in this chapter and analysed from the perspective of the study's objectives, which are to identify interesting objects within the MeerKAT fields based on their radio morphology, assemble available archival multi-wavelength data and build spectral energy distributions for those sources for which sufficient multi-wavelength coverage exists. The input parameters used to generate the SED for radio galaxy MKAT J221834.96-082253.50 are defined. The single-zone leptonic model proposed by Böttcher et al. (2013) was used to fit the broadband SEDs.

4.1 Radio continuum emission

Figure 4.1 shows the FRB 20171019A (RA(J2000) = $22^h17^m32^s.00$; DEC(J2000) = $-08°39'32''.0$) MeerKAT L band configuration image. Fifty-eight (58) of Sixty-four (64) antennas were used, with a total synthesised bandwidth of 856 MHz and a centre frequency of 1284 MHz. It has the root mean square (rms) noise of 5.2 μJy beam^{-1}, and a 3σ detection of < 15 μJy beam^{-1}. The quasars J1939-6342 (RA(J2000) = $19^h39^m25^s.05$; DEC(J2000) = $-63°42'43''.6$) and the J2225-0457 (RA(J2000) = $22^h25^m47^s.26$; DEC(J2000) = $-4°57'01''.4$) were used for the absolute flux density and gain calibration, respectively. The target, "FRB 20171019A", was observed for 5400.0 sec; J1939-6342 was observed for 600.0 sec, and J2225-0457 was observed for 840.0 sec and the total observation time was 7247.12 sec.

Figure 4.2 shows the FRB 20190711A (RA(J2000) = $21^h56^m00^s.00$; DEC(J2000) = $-80°23'00''.0$) MeerKAT L band configuration image. Sixty (60) of Sixty-four (64) antennas were used with a total synthesised bandwidth of 856 MHz and a centre frequency of 1284 MHz. It has the root mean square (rms) noise of 4.6 μJy beam^{-1}, and a 3σ detection of < 15

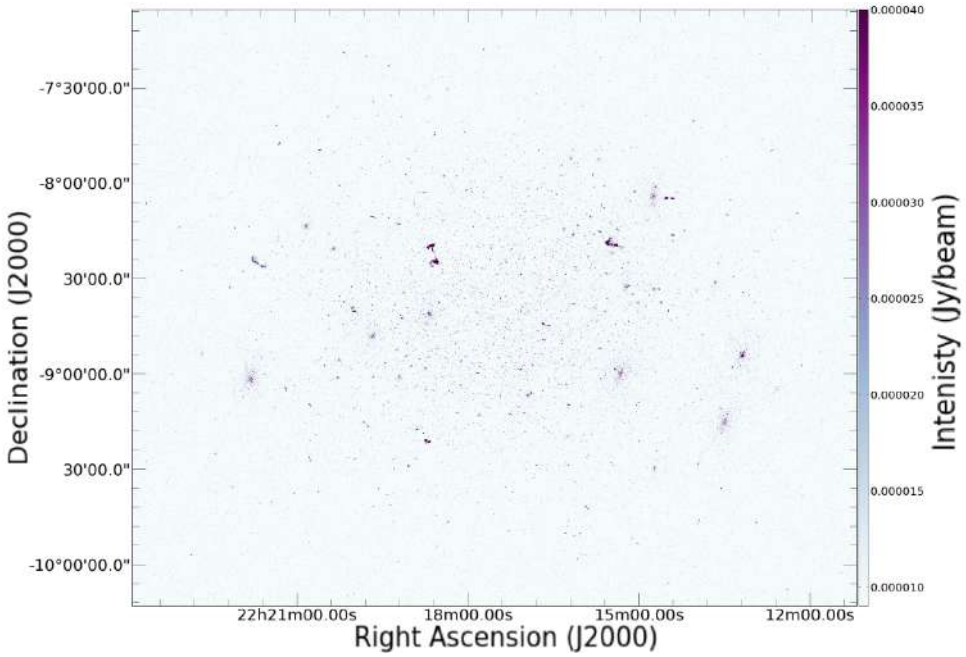

Figure 4.1: FRB 20171019A MeerKAT field.

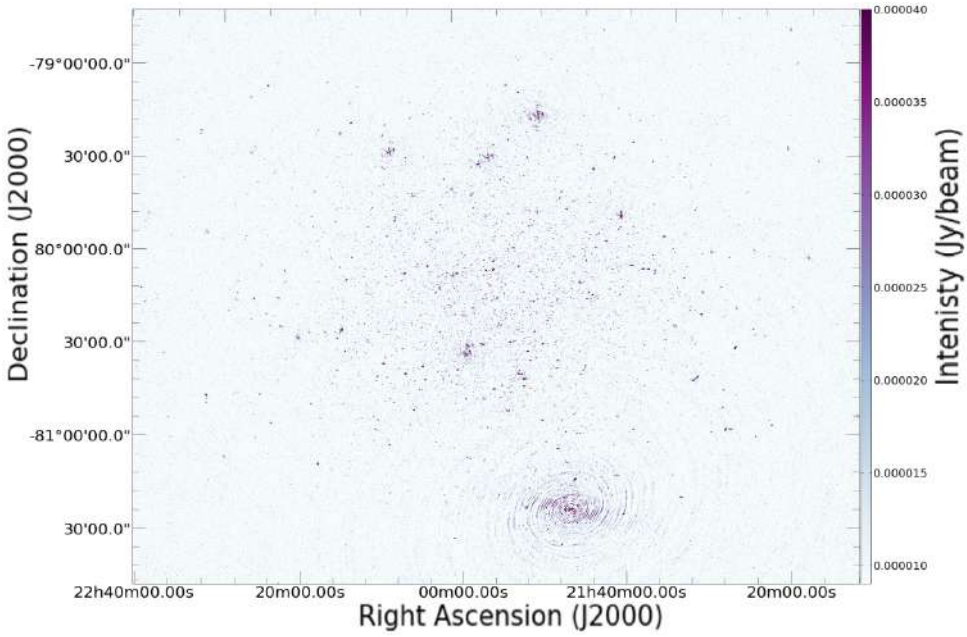

Figure 4.2: FRB 20190711A MeerKAT field.

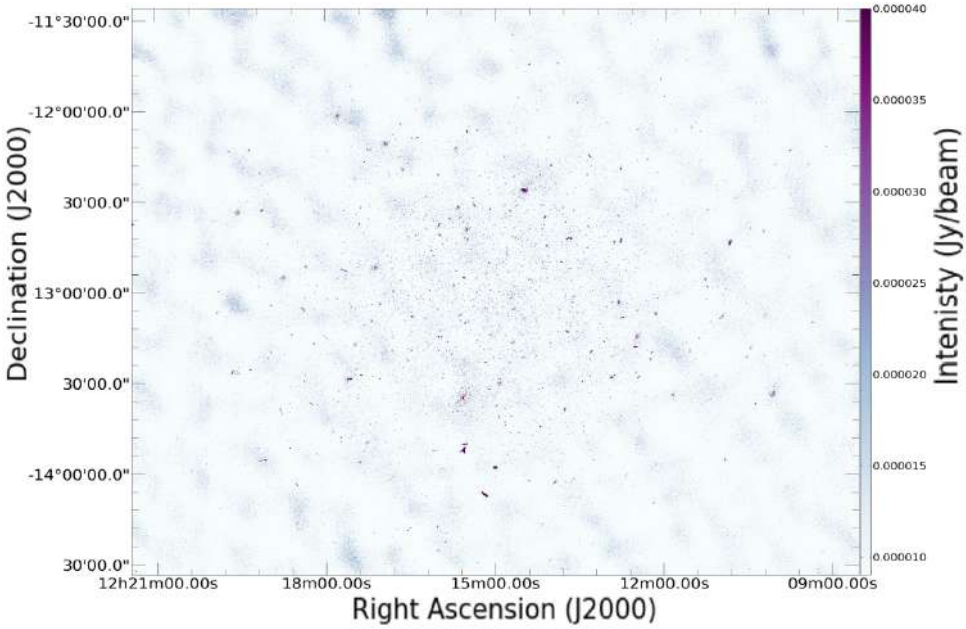

Figure 4.3: FRB 20190714A MeerKAT field.

μJy beam^{-1}. The J0408-6545 and the J1619-8418 were used for the absolute flux density and gain calibration, centred at RA(J2000) = $4^h08^m20^s.38$; DEC(J2000) = $-64°45'09''.6$ and RA(J2000) = $16^h19^m33^s.97$; DEC(J2000) = $-84°18'19''.1$,respectively. The target, "FRB 20190711A", was observed for 5400.0 sec; J0408-6545 was observed for 300.0 sec, and J1619-8418 was observed for 840.0 sec and the total observation time was 6942.65 sec.

Figure 4.3 shows the FRB 20190714A (RA(J2000) = $12^h15^m00^s.02$; DEC(J2000) = $-13°00'00''.0$) MeerKAT L band configuration image. Sixty (60) of Sixty-four (64) antennas were used, with a total synthesised bandwidth of 856 MHz and a centre frequency of 1284 MHz. It has the root mean square (rms) noise of 5.8 μJy beam^{-1}, and a 3σ detection of 52.0 μJy beam^{-1}. The J1939-6342 and the J2225-0457 J1215-1731 (RA(J2000) = $12^h15^m46^s.84$; DEC(J2000) = $-17°31'46''.2$) were used for the absolute flux density and gain calibration, respectively. The target, "FRB 20190714A", was observed for 5400.0 sec; J1939-6342 was observed for 600.0 sec, and J1215-1731 was observed for 840.0 sec and the total observation time was 7388.43 sec.

4.2 Objects of interest

Radio galaxies were classified as interesting radio sources based primarily on their radio morphology, and the presence of three well-resolved features (central engine, radio jets, and radio lobes) (see Figure 4.4). The remaining radio galaxies are presented in Appendix A. Forty-two (42) interesting radio galaxies were identified from the MeerKAT fields (see Table 4.1). Twenty-two (22) sources were from the FRB 20171019A field; seven (7) sources were from the FRB 20190711A field; and thirteen (13) sources were from the FRB 20190714A field.

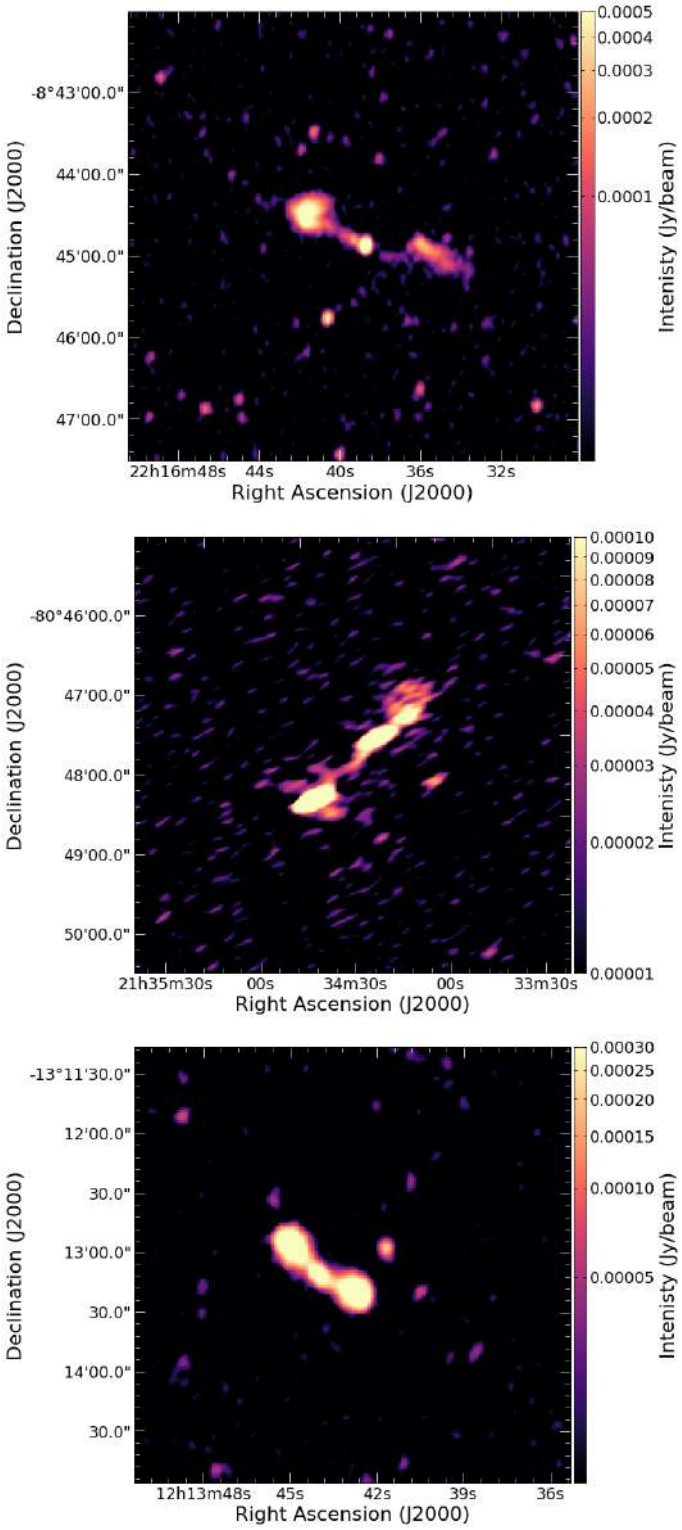

Figure 4.4: Three selected radio galaxies from MeerKAT fields. The image at the top is from the FRB 20171019A field, the centre one is from the FRB 20190714A field, and the bottom is from the FRB 20190711A field. The remaining radio galaxies are presented in Appendix A.

FRB 20171019A						
Source name	Coordinates (≈)		Morphology			Counterparts
	J2000		Core	Jet(s)	Lobe(s)	High Energy
	RA	DEC	Detection			2XMMi source catalogue
MKAT J221834.96-082253.50	$22^h18^m36^s.96$	$-08°22'53''.50$	✓	✓	✓	✓
MKAT J221939.10-073444.56	$22^h19^m39^s.10$	$-07°34'44''.56$	✗	✗	✓	✗
MKAT J222118.12-081735.54	$22^h21^m18^s.12$	$-08°17'35''.54$	✓	✗	✓	✗
MKAT J222034.40-074945.96	$22^h20^m34^s.40$	$-07°49'45''.96$	✓	✗	✓	✗
MKAT J221936.32-081109.02	$22^h19^m36^s.32$	$-08°11'09''.06$	✓	✓	✓	✗
MKAT J22184562-080310.22	$22^h18^m45^s.62$	$-08°03'10''.22$	✓	✓	✗	✗
MKAT J221800.66-080227.69	$22^h18^m00^s.66$	$-08°02'27''.69$	✓	✗	✓	✗
MKAT J222036.62-085608.03	$22^h20^m36^s.62$	$-08°56'08''.03$	✓	✗	✗	✗
MKAT J222014.19-091348.00	$22^h20^m14^s.19$	$-09°13'48''.00$	✓	✗	✓	✗
MKAT J222045.66-091004.88	$22^h20^m45^s.66$	$-09°10'04''.88$	✓	✗	✓	✗
MKAT J221946.34-091618.28	$22^h19^m46^s.34$	$-09°16'18''.28$	✓	✓	✓	✗
MKAT J221747.60-091241.91	$22^h17^m47^s.60$	$-09°12'41''.91$	✓	✓	✗	✗
MKAT J221916.90-092652.50	$22^h19^m16^s.90$	$-09°26'52''.50$	✓	✓	✗	✗
MKAT J221857.49-092632.99	$22^h18^m57^s.49$	$-09°26'32''.99$	✓	✗	✓	✗
MKAT J221749.39-094051.87	$22^h17^m49^s.39$	$-09°40'51''.87$	✓	✓	✗	✗
MKAT J221541.18-072137.89	$22^h15^m41^s.18$	$-07°21'37''.89$	✓	✗	✓	✗
MKAT J221638.73-084454.07	$22^h16^m38^s.73$	$-08°44'54''.07$	✓	✓	✓	✗
MKAT J221400.26-083404.97	$22^h14^m00^s.26$	$-08°34'04''.97$	✓	✓	✗	✗
MKAT J221647.69-092901.94	$22^h16^m47^s.69$	$-09°29'04''.69$	✓	✗	✓	✗
MKAT J221501.91-095339.58	$22^h15^m01^s.91$	$-09°53'39''.58$	✓	✗	✓	✗
MKAT J221555.84-094211.26	$22^h15^m55^s.84$	$-09°42'11''.26$	✗	✗	✓	✗
MKAT J221559.15-095721.20	$22^h15^m59^s.15$	$-09°57'21''.20$	✓	✗	✓	✗
FRB 20190711A						
MKAT J220651.89-794016.15	$22^h06^m51^s.89$	$-79°40'16''.15$	✓	✗	✓	✗
MKAT J215514.73-794506.12	$21^h55^m14^s.73$	$-79°55'06''.12$	✓	✗	✓	✗
MKAT J223112.35-801714.91	$22^h31^m12^s.35$	$-80°17'14''.91$	✓	✗	✓	✗
MKAT J222728.58-805114.45	$22^h27^m28^s.58$	$-80°51'14''.45$	✓	✗	✓	✗
MKAT J214949.16-795039.84	$21^h49^m49^s.16$	$-79°50'39''.84$	✓	✗	✗	✗
MKAT J213953.58-801346.58	$21^h39^m53^s.59$	$-80°13'46''.58$	✓	✗	✓	✗
MKAT J213431.14-804716.94	$21^h34^m31^s.14$	$-80°47'16''.94$	✓	✓	✓	✗
FRB 20190714A						
MKAT J121532.03-135026.52	$12^h15^m32^s.03$	$-13°50'26''.52$	✓	✗	✓	✗
MKAT J121344.05-131310.72	$12^h13^m44^s.05$	$-13°13'10''.72$	✓	✓	✓	✗
MKAT J121800.40-131456.51	$12^h18^m00^s.40$	$-13°14'56''.51$	✓	✓	✓	✗
MKAT J121523.92-123023.21	$12^h15^m23^s.92$	$-12°30'23''.21$	✓	✓	✓	✗
MKAT J121815.61-133651.12	$12^h18^m15^s.61$	$-13°36'51''.12$	✓	✓	✗	✗
MKAT J121907.41-135535.80	$12^h19^m07^s.41$	$-13°55'35''.80$	✓	✗	✓	✗
MKAT J121558.91-124114.01	$12^h15^m58^s.91$	$-12°41'14''.01$	✓	✗	✓	✗
MKAT J121740.73-124337.38	$12^h17^m40^s.73$	$-12°43'37''.38$	✓	✗	✓	✗
MKAT J121809.93-124323.17	$12^h18^m09^s.93$	$-12°43'23''.17$	✓	✗	✓	✗
MKAT J121752.58-134615.29	$12^h17^m52^s.58$	$-13°46'15''.29$	✓	✓	✓	✗
MKAT J121243.67-122602.82	$12^h12^m43^s.67$	$-12°26'02''.82$	✓	✗	✓	✗
MKAT J121338.55-130217.43	$12^h13^m38^s.55$	$-13°02'17''.43$	✓	✗	✓	✗
MKAT J120923.40-130955.90	$12^h09^m23^s.40$	$-13°09'55''.90$	✓	✗	✓	✗

Table 4.1: The sources of interest from the three MeerKAT FRB fields along with their properties. The tick symbol (✓) serves as an indicator of the identification of the core, jet(s), lobe(s), and the existence of high-energy counterparts. On the other hand, the cross symbol (✗) denotes the absence of detection or counterparts.

The selected source

Figure 4.5 shows the image of MKAT J221834.96-082253.50, a striking radio galaxy selected from forty-two (42) radio galaxies because of its radio morphology. The collimated jets and radio lobes are well-resolved. This radio galaxy is from the FRB 20171019A MeerKAT field. The factor that led to the selection of this radio galaxy for further study was the availability of X-ray data. Its radio morphology exhibits a fair symmetry with kiloparsec-scale radio jets (208.67″ and 142.34″ for the northeast and southeast jet, respectively) that extend from the nucleus on both sides, even though the central region is not well resolved. The locations of the upper and lower lobes are northeast (NE-Lobe) and southwest (SW-Lobe), respectively. These lobes appear edge-brightened, a characteristic feature of an FR II radio galaxy (Fanaroff and Riley, 1974). Both lobes are bent towards an easterly direction, and the SW-lobe has weaker emission than the NE-lobe (with the shape of an axe), presumably due to interactions with the surrounding environment and the intergalactic medium (IGM). There are hot spots at the edges of the lobes and along the jets of the NE-Lobe. These hot spots likely indicate shocks formed as a result of the jet's interaction with the IGM.

The source is at a luminosity distance of 737.12 ± 51.60 Mpc (Albareti et al., 2017), with a redshift of $z = 0.16786 \pm 0.00003$ (Ahn et al., 2012). The luminosity distance and redshift were estimated based on the search query in Set Of Identifications, Measurements, and Bibliography for Astronomical Data (SIMBAD)[1], with a search radius of 2 arc-minutes. The counterpart used for the luminosity distance and redshift estimation is LEDA 1004803 (Best et al., 2005; Takey et al., 2013) since it is the only source near MKAT J221834.96-082253.50 with a redshift, and its coordinates are RA(J2000) = $22^h18^m37^s.35$ and DEC(J2000) = $-08°21'09''.10$.

[1] https://simbad.cds.unistra.fr/

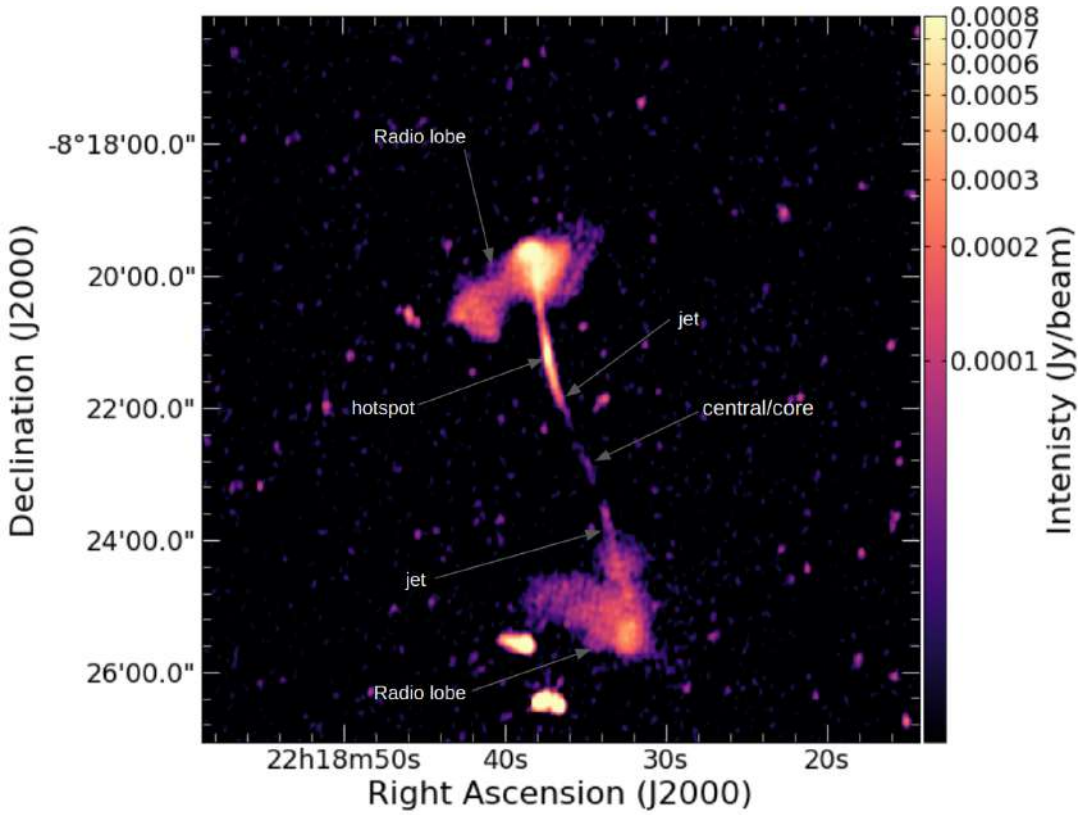

Figure 4.5: A high-resolution radio image of MKAT J221834.96-082253.50 at a frequency of 1.28 GHz, imaged with the MeerKAT telescope. The rms value is $\sigma = 1.88\mu$Jy/beam.

4.3 Spectral index map

The spectral index determines the power-law distribution of the radiation flux, S, emitted by a radio galaxy; this distribution is characteristic of synchrotron emission, $S_\nu \propto \nu^\alpha$, where α is the spectral index. The spectral index is flat within the hot spot regions and steepens towards the inner regions of the lobes. This is consistent with relativistic electrons forming at a shock region, where plasma is transported at high speeds from the core. After the shock has receded, the plasma in the lobe cools and α becomes steeper. The regions closer to the core, which were formed earlier, have harder spectra than regions further out. Figures 4.6 and 4.7 shows the spectral index and index error maps of radio galaxy MKAT J221834.96-082253.50, respectively. Due to MeerKAT's wide bandwidth and sensitivity, in-band spectral index maps can be generated from a single observation. The spectral index distribution of MKAT J221834.96-082253.50 was achieved by combining the sub-band full-resolution FITS images. There were 8 sub-band images with the central frequencies of 909, 1016, 1123, 1230, 1337, 1444, 1551, and 1658 MHz, respectively. Every single sub-band image's synthesised beam was adjusted to be the same.

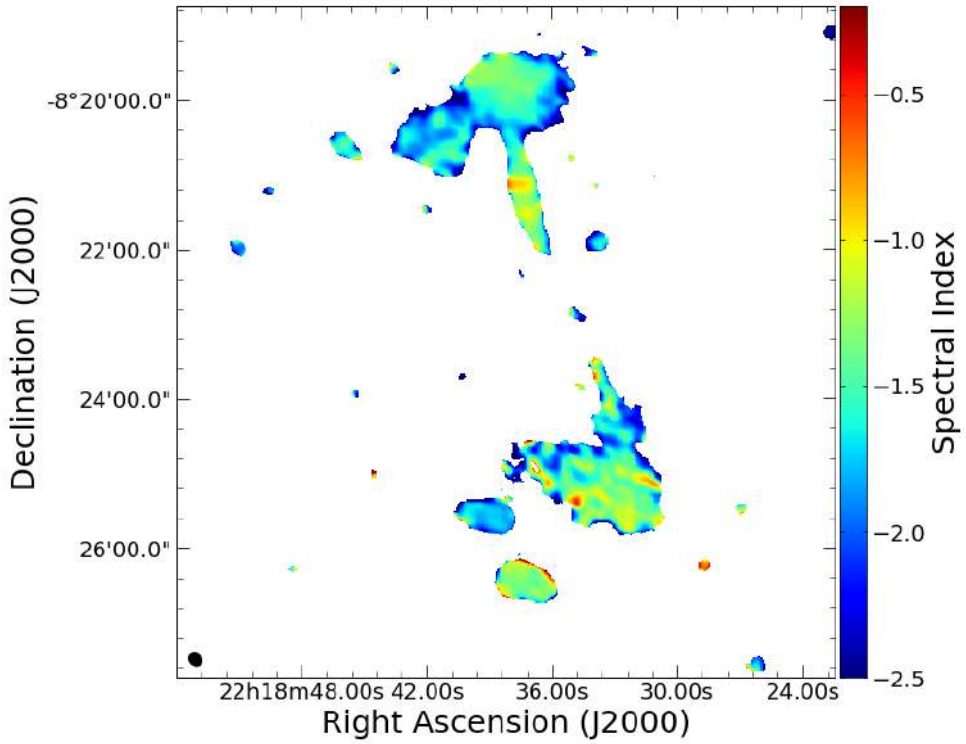

Figure 4.6: The spectral index map of MKAT J221834.96-082253.50, the colour bar indicates the variation in the spectral index. The synthesised beam ($6.8^{''} \times 5.0^{''}$) of each sub-band image is represented by a black ellipse in the lower left corner.

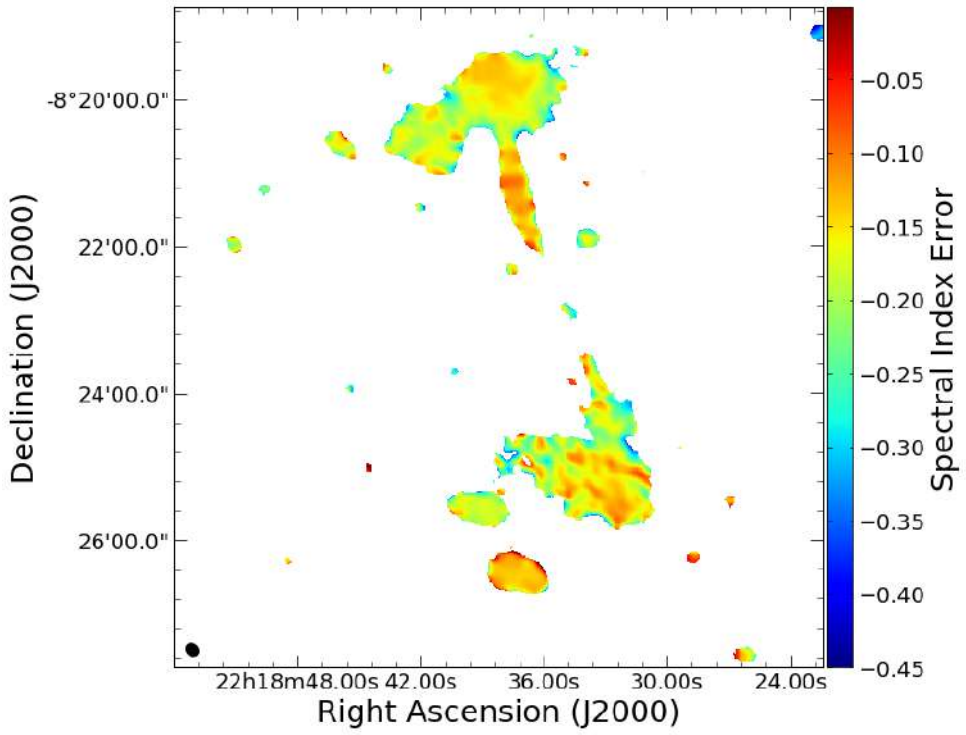

Figure 4.7: The spectral index error map of MKAT J221834.96-082253.50. The colour bar indicates the uncertainty, which varies across the image. The synthesised beam ($6.8^{''} \times 5.0^{''}$) is represented in a black ellipse in the lower left corner.

4.4 Multi-wavelength archival FITS image

4.4.1 Radio band

The Karl G. Jansky VLA was used for the Faint Images of the Radio Sky at Twenty Centimetres (FIRST) survey. According to this survey, NVSS 221836-082120 was detected at a frequency of 1.4 GHz (Condon et al., 1998). The integrated flux of this detection is reported to be 8.3 ± 0.9 mJy, with a position angle of 85.6° (see Figure 4.8). The observation was part of the survey image field C2224M08. The observation was conducted on 20 September 1993 in A configuration at L-band and the image centred at $22^h18^m36^s.96$ (Right Ascension (J2000)) and $-08°21'20''.4$ (Declination (J2000)). As can be seen from the image, only edge-brightened radio lobes are detected, typical for FR-II radio galaxies. Even though NVSS is very sensitive to diffuse emission at large-scale, the jets and core are not resolved, and the survey fails to reveal the source's finer details because of the coarser resolution of 45″. Figure 4.9 shows the grey contours of the 1.28 GHz radio emission morphology of MKAT J221834.96-082253.50 as imaged with the MeerKAT telescope and superimposed on the 1.4 GHz VLA image. The contour levels are 0.05, 0.1, 0.2, 0.4, 0.6, and 0.8 mJy beam^{-1}.

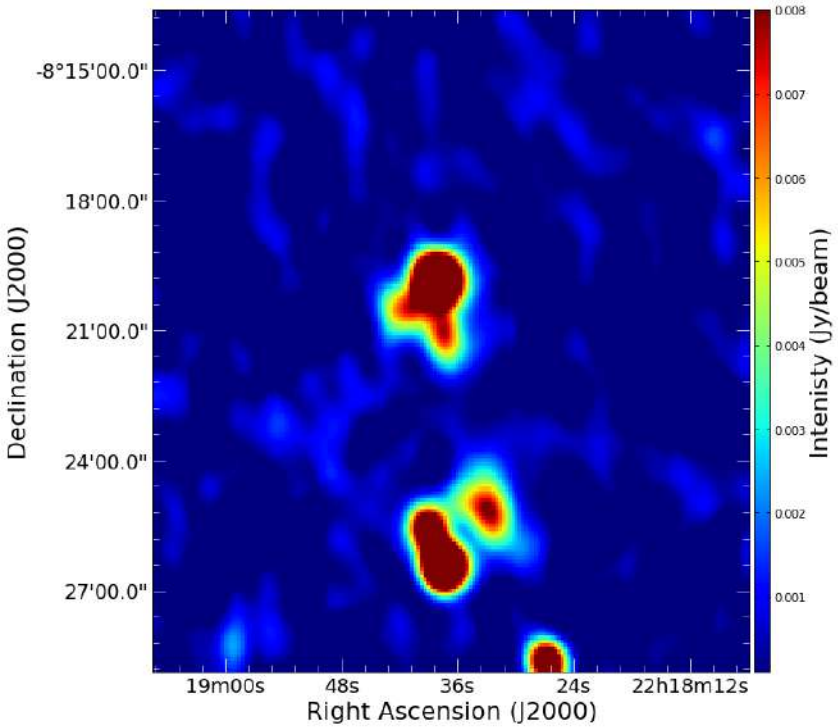

Figure 4.8: The 1.4 GHz image of NVSS 221836-082120 from the NVSS catalogue. (Credit: Condon et al. 1998).

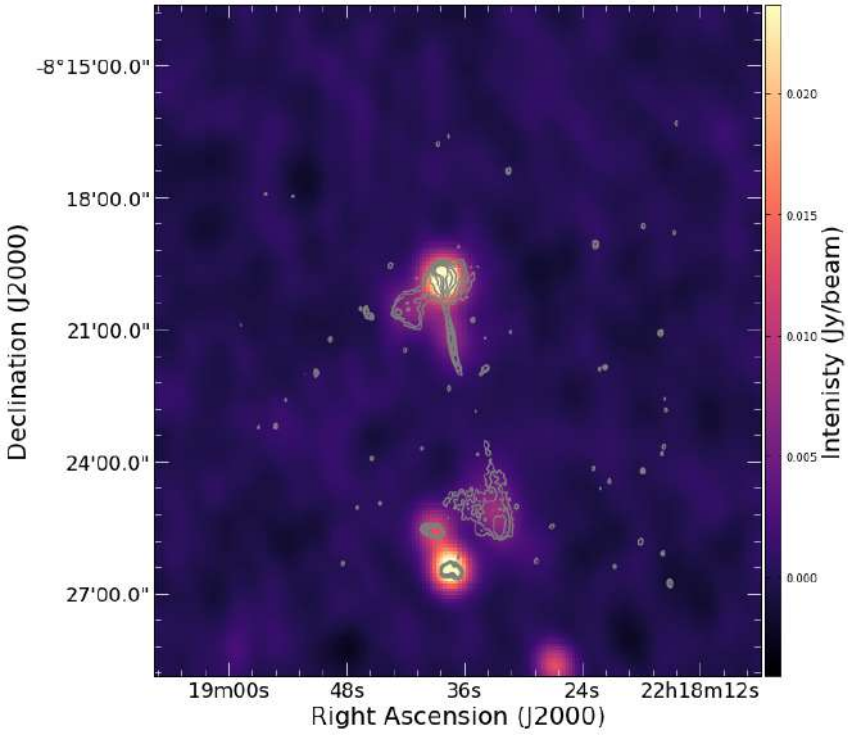

Figure 4.9: The contours (grey) of the 1.28 GHz radio emission morphology of MKAT J221834.96-082253.50 superimposed on the 1.4 GHz VLA image.

4.4.2 Infrared band

Two Micron All Sky Survey (2MASS)

Figure 4.10 shows J-H-K_s bands 2MAASS composite (red, green, and blue (RGB)) image of 2MASS J22183738-0821085 obtained from the 2MASS All-Sky Point Source Catalog (Skrutskie et al., 2006). An infrared source is found at right ascension (J2000) is $22^h18^m37^s.38$ and the declination (J2000) is $-08°21'08''.5$. The observation date was 18 October 1998, with the seeing FWHM of 2.63965" and a zero point (magnitude) of 19.8725. The magnitude scale is stretched logarithmically using a technique that optimises the enhancement of low surface brightness aspects of the galaxy while preserving good contrast in the nucleus.

Figure 4.11 shows the contours (white) of the 1.28 GHz radio emission morphology of MKAT J221834.96-082253.50 superimposed on the K_s-band full image of 2MASS J22183738-0821085. The contour levels are 0.05, 0.1, 0.2, 0.4, 0.6, and 0.8 mJy beam^{-1}. The 2MASS source is associated with the hot-spot region on the jet, along the northern direction of the radio galaxy (see the right panel of Figure 4.11 and Figure 4.6) of MKAT J221834.96-082253.50. The counterpart from 2MASS is located in the hot-spot region on the northeast jet of MKAT J221834.96-082253.50 (see the right panel of Figure 4.15 and Figure 4.6) with J, H, and K_s fluxes ranging from 14.570 to 13.318 magnitudes, which results in a near-infrared luminosity of approximately 4×10^{45} erg s^{-1}.

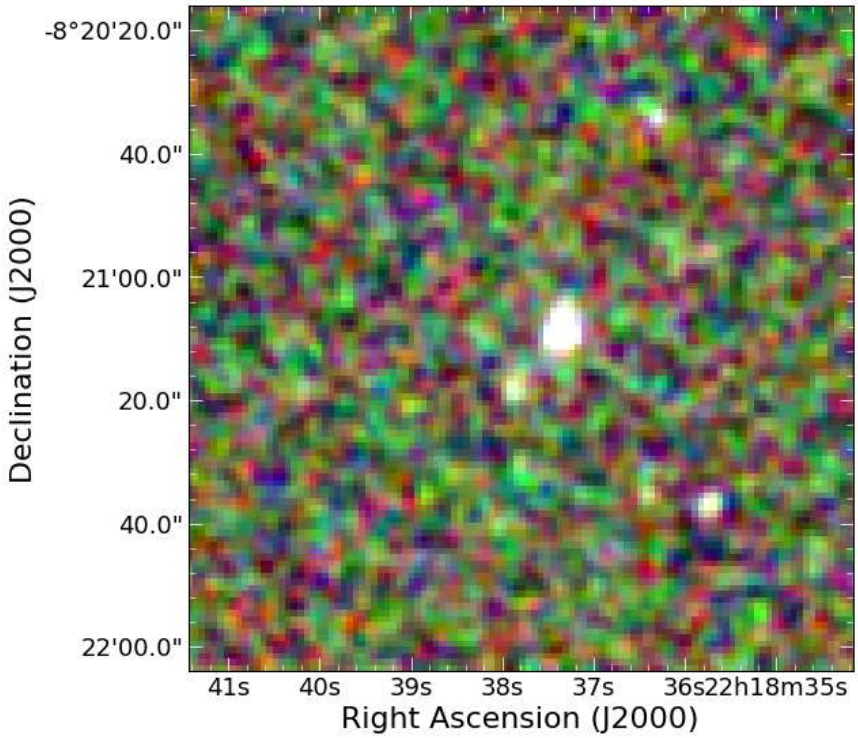

Figure 4.10: The composite J-H-K_s image (RGB) of 2MASS J22183738-0821085 from the 2MASS All-Sky Point Source Catalog. (Credit: https://irsa.ipac.caltech.edu/cgi-bin/2MASS/IM/nph-im_pos?type=at&ds=asky&date=&scan=&coadd=&band=A&subsz=120&POS=334.655676+-8.35251620).

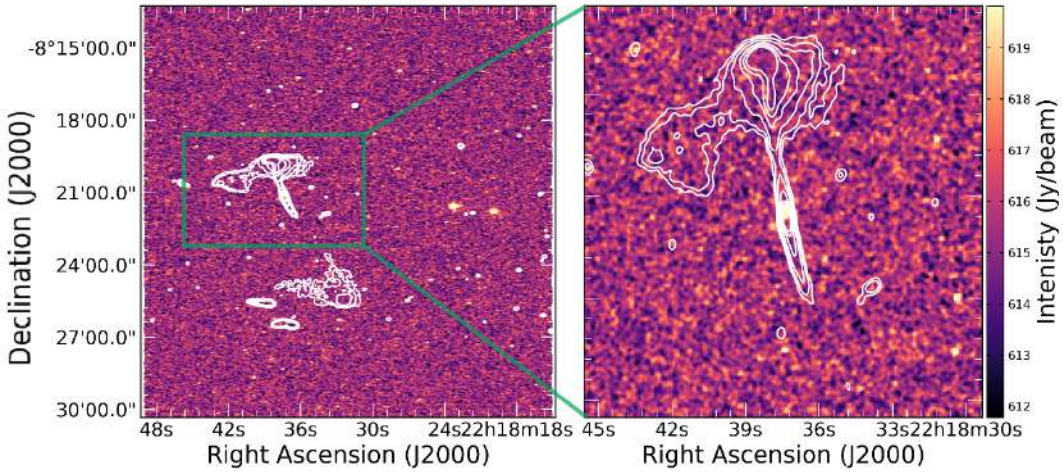

Figure 4.11: Left panel: The K_s-band 2MASS image of 2MASS J22183738-0821085, with the contours (white) of MKAT J221834.96-082253.50 superimposed. Right panel: the zoomed image of the position of the 2MASS counterpart with 1.28 GHz radio emission morphology contours of MKAT J221834.96-082253.50 from the full image.

The Wide-field Infrared Survey Explorer (WISE)

The mid-infrared images obtained from WISE are shown in Figure 4.12. These images were obtained using the 3.4 μm (W1) and 4.6 μm (W2) bands, which are stellar-sensitive, as well as the 12 μm (W3) and 22 μm (W4) bands, which are sensitive to the interstellar medium (ISM). The images have angular resolutions of 6.1, 6.4, 6.5, and 12 arcsecs, respectively. In the 3.4 and 4.6 μm bands, the hot-spot region is detected and the emission is extended to the southeast direction. The observation dates of the earliest, middle and latest frames for all bands were on the 22nd, 23rd and 25th of May 2010, respectively. The observed right ascension (J2000) is $22^h18^m37^s.36$, and the declination (J2000) is $-08°21'09''.0$. The 1-σ uncertainties of each band in zero point are 0.006, 0.007, 0.012, and 0.012 mags, respectively. Figure 4.13 shows the W1 image with the contours of the 1.28 GHz MHz radio emission morphology of MKAT J221834.96-082253.50 superimposed; the contour levels are 0.05, 0.1, 0.2, 0.4, 0.6, and 0.8 mJy beam^{-1}.

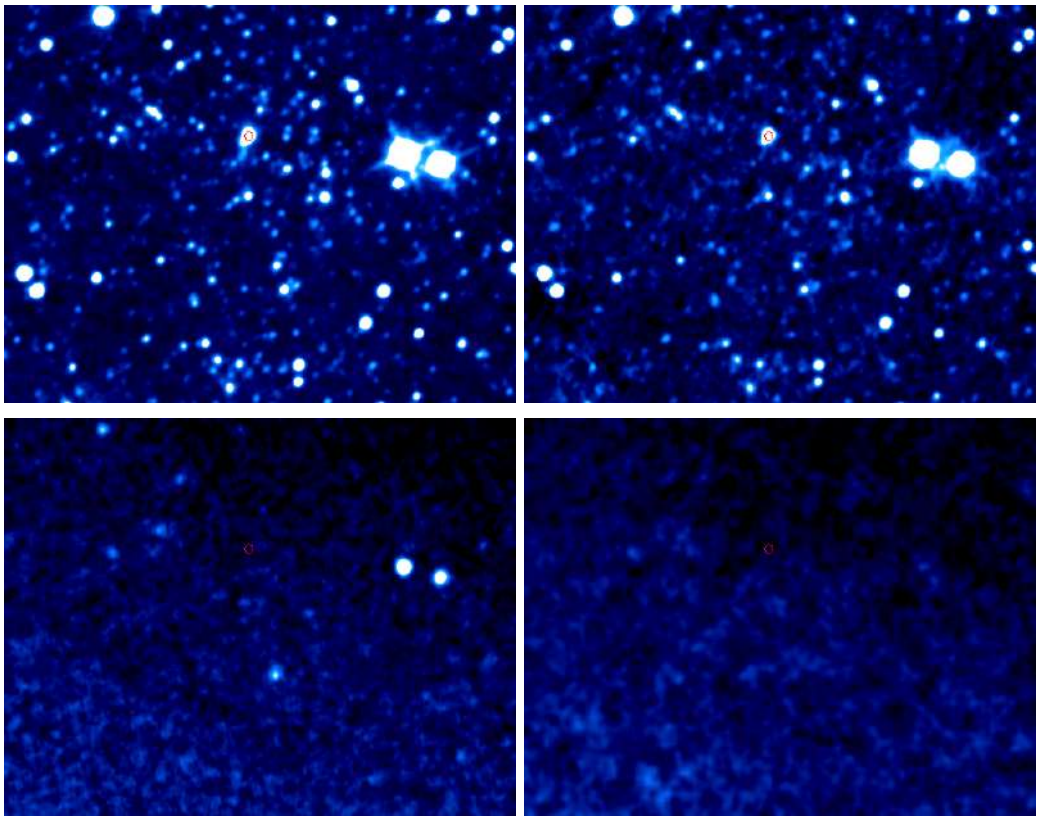

Figure 4.12: Top left: The WISE band 1 (W1), top right: band 2 (W2), bottom left: band 3 (W3), bottom right: band 4 (W4) image of WISE J221837.36-082109.0 and is the target in the ALLWISE catalogue. The red circles indicate the hot-spot region and the size of each image is $93.84' \times 93.84'$. (Credit: Wright et al. 2010).

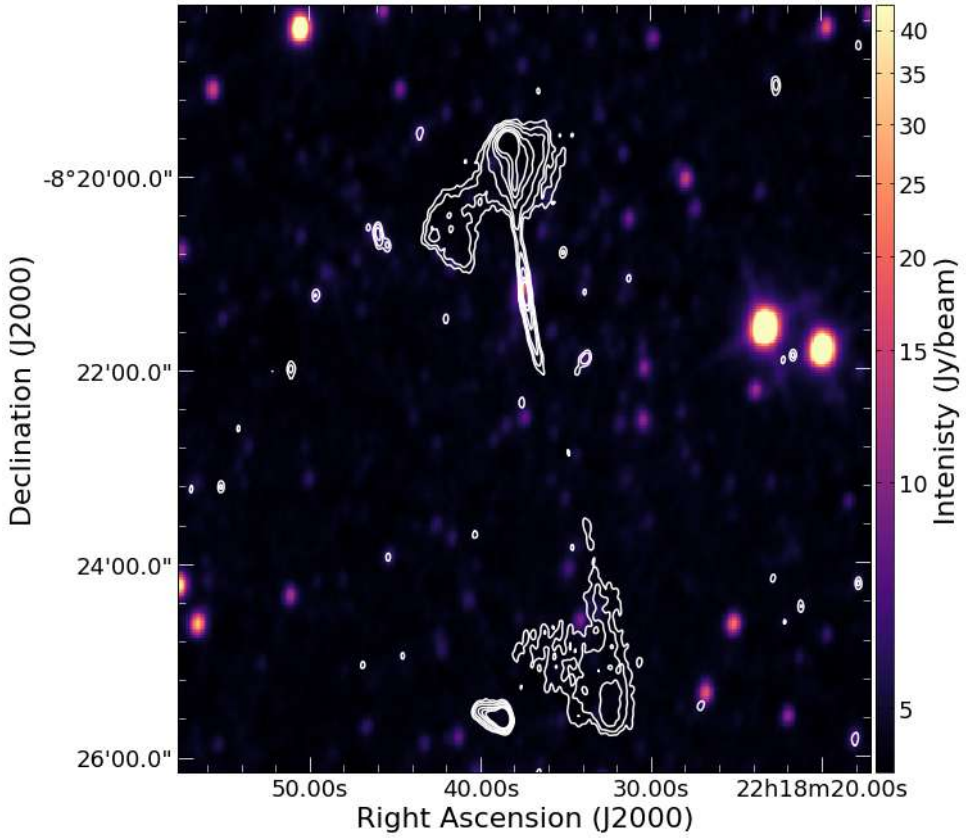

Figure 4.13: W1 image from WISE with the contours (white) of MKAT J221834.96-082253.50 superimposed.

From Figure 4.13, the WISE counterpart is associated with the hot-spot region on the jet, along the north direction of the radio galaxy and is very bright and luminous. The absence of prolonged infrared emission from the lobes is consistent with the anticipated lack of substantial thermal emission associated with the radio galaxies' lobes. Infrared observations from 2MASS and WISE show no sign of the radio core and dust emission associated with the SMBH accretion disk.

4.4.3 Optical band

Figure 4.14 shows the SDSS composite image (from u, g, r, i, and z bands) of SDSS J221837.36-082109.0 obtained from the SDSS Data Release 13 catalogue (SDSS Collaboration et al., 2016). The observed right ascension (J2000) is $22^h18^m37^s.36$, and the declination (J2000) is $-08°21'09''.09$. The date of observation was 03 September 2000. Figure 4.15 shows the 1.28 GHz radio emission morphology of MKAT J221834.96-082253.50 superimposed on the g-band optical image. The contour levels are 0.05, 0.1, 0.2, 0.4, 0.6, and 0.8 mJy beam^{-1}. The optical counterpart is also associated with the hot-spot region on the jet, along the northern direction of the radio galaxy (see the right panel of Figure 4.15 and Figure 4.6) of MKAT J221834.96-082253.50. The coordinates for the counterpart from the optical source used for the core are RA(J2000) = $22^h18^m34^s.58$ and DEC(J2000) = $-08°22'53''.08$.

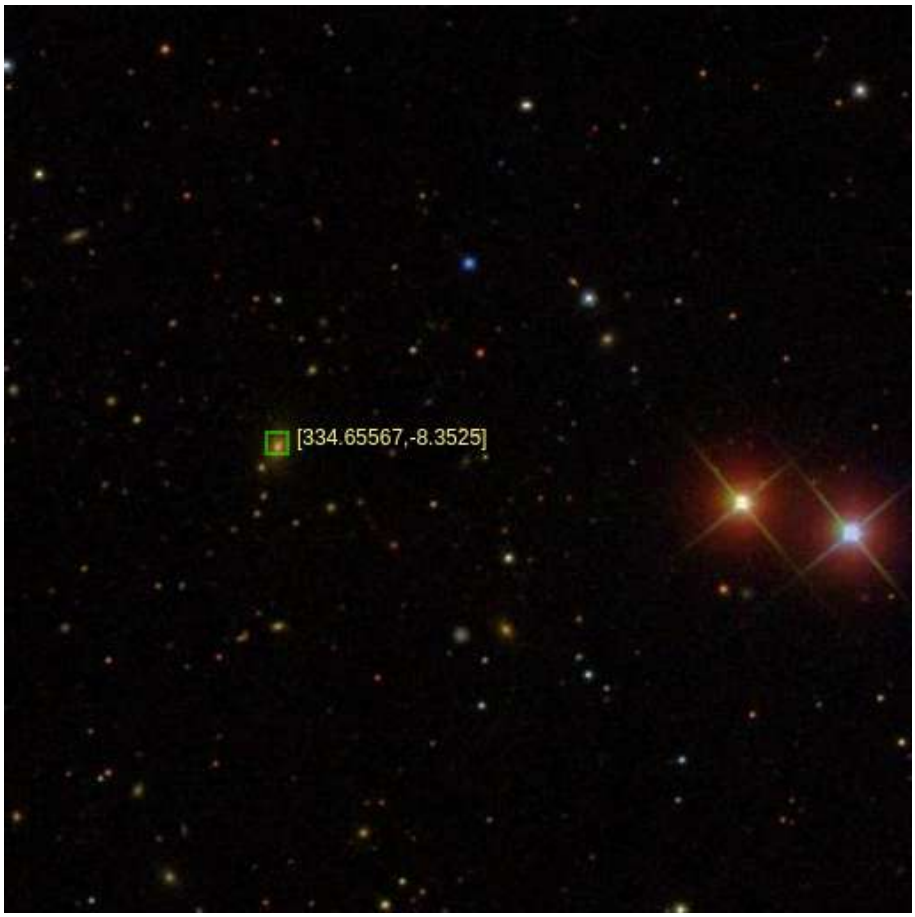

Figure 4.14: The u, g, r, i, and z bands composite SDSS image of SDSS J221837.36-082109.0. The green box indicates the detection of the hot-spot region of MKAT J221834.96-082253.50 and the numbers inside the brackets represent the sky coordinate in degrees. (Credit: https://skyserver.sdss.org/dr13/en/tools/explore/summary.aspx?id=1237652600107892869).

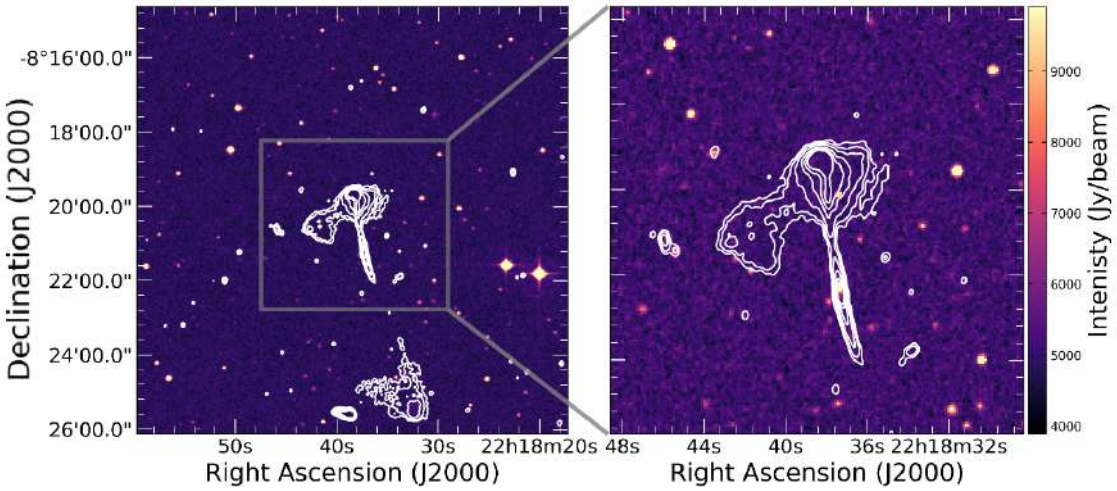

Figure 4.15: Left panel: The g-band image of SDSS J221837.54-082117.4 taken from the SDSS DR13. The white contours show the 1.28 GHz radio emission morphology of MKAT J221834.96-082253.50. Right panel: the SDSS DR13 g-band zoomed image of the position of the optical counterpart with 1.28 GHz radio emission morphology contours of MKAT J221834.96-082253.50 from the full image.

4.4.4 High-Energy band (X-ray and γ-ray)

There are no FITS images of MKAT J221834.96-082253.50 found in the archives that are associated with the X-ray and γ-ray bands. The X-ray counterparts (see Tables A.1 and A.2) were obtained from XMM-Newton 2nd Incremental Source (2XMMi source) catalogue (Xmm-Newton Survey Science Centre, 2008) accessed through SAOImage DS9. The coordinates for the counterpart from the X-ray sources used for the core are RA(J2000) $= 22^h18^m35^s.60$ and DEC(J2000) $= -08°23'04''.49$, while for the hot-spot, the coordinates are RA(J2000) $= 22^h18^m37^s.44$ and DEC(J2000) $= -08°21'14''.82$. Fermi Large Area Telescope (LAT) 10-year Source DR2 catalog (Abdollahi et al., 2020) was used to obtain the upper limit. This was estimated from the flux threshold of the 4FGL-DR2 catalog with a confidence level of 3σ and is above the gamma-ray flux of ~ 1 GeV.

4.5 SEDs of MKAT J221834.96-082253.50

The overall multi-wavelength spectral energy distributions of the radio galaxy core and hot-spot region, obtained from the archival data (see Tables A.1 and A.2) over the widest range, are shown in Figures 4.16 and 4.17, respectively. The SED is well reproduced through the use of a leptonic model (see Table 4.2 for the input parameters used). The model for both the core and hot-spot region was fitted using the same input parameters due to the lack of sufficient information on MKAT J221834.96-082253.50 in the archives or literature. As a result, most of these input parameters were estimated using the available archival data points. The catalogues where the data points were obtained are NVSS (radio band), 2MASS Point Sources (infrared band), SDSS Release 9 (optical band), XMM-Newton 2nd Incremental Source (2XMMi source) (X-ray band), and Fermi-LAT 10-year Source DR2 (γ-ray band). The core and hot region SED is dominated by non-thermal emission at low frequencies. The model shows a low-frequency component that peaks near optical frequencies while the high-energy component peaks at GeV energies. An upper limit on the high-energy band is shown by the orange arrow ($\sim 2 \times 10^{11}$ erg cm^{-2} s^{-1}). In Figure 4.16, the archival measurements of optical fluxes do not fit with the model. In Figure 4.17, the optical spectrum does not match the IR spectrum in any physically realistic manner. Therefore, it is believed that the data optical data points are not actually associated with the core or hot-spot.

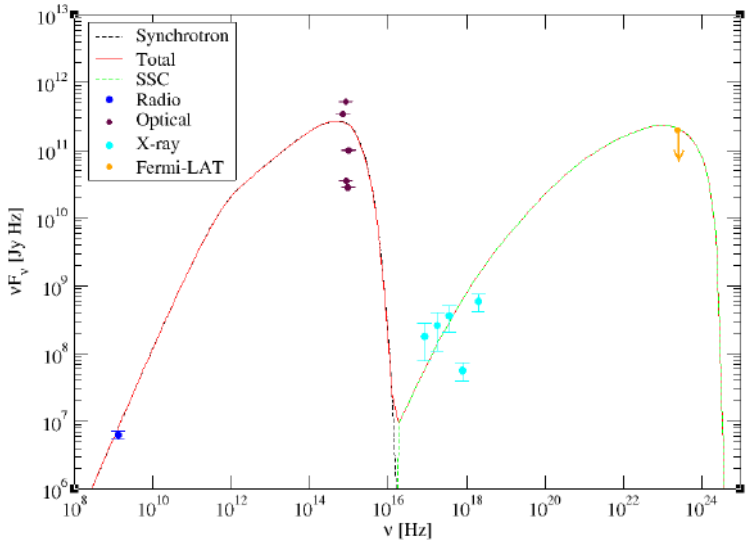

Figure 4.16: The SED of the central region of MKAT J221834.96-082253.50. The synchrotron, SSC, and total are represented by a black broken line, green broken line, and solid red line, respectively. The data points represent the fluxes with errors of different wave-band (radio (dark-blue), optical (maroon), and x-ray (sky-blue)) from the archives. The upper limit is from the Fermi Large Area Telescope (LAT) 10-year Source DR2 catalog (orange).

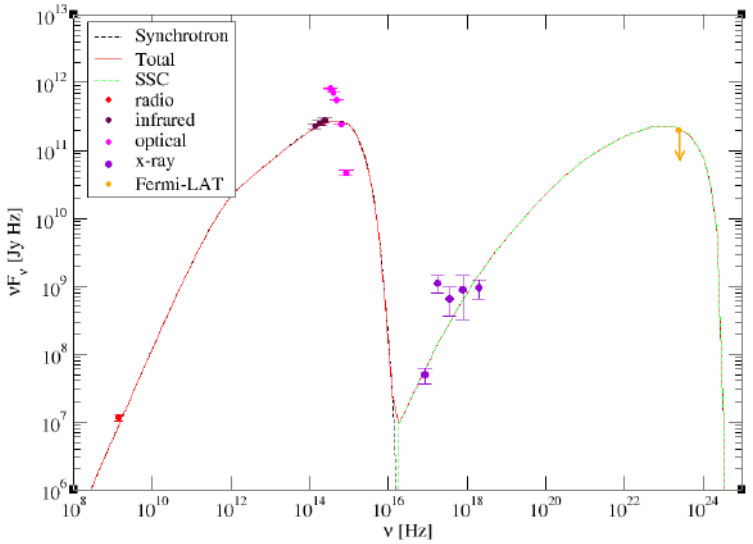

Figure 4.17: The SED of the hot-region of MKAT J221834.96-082253.50. The synchrotron, SSC, and total are represented by a black broken line, green broken line, and solid red line, respectively. The data points represent the fluxes with errors of different wave-band (radio (red), infrared (maroon), optical (pink), and x-ray (purple)) from the archival. The upper limit is from the Fermi Large Area Telescope (LAT) 10-year Source DR2 catalog (orange).

Parameter	**Symbol**	**MKAT J221834.96-082253.50**
Injection luminosity	$L_{e,inj}$	$2.5 \times 10^{44}\ erg\ s^{-1}$
Electron injection minimum energy	$\gamma_{e,min}$	2.5×10^{4}
Electron injection maximum energy	$\gamma_{e,max}$	3.8×10^{4}
Electron injection spectral index	q_e	1.01
Escape time parameter	η_{esc}	0.25
Magnetic field at z_0	**B**	0.25 G
Injection height	z_0	1.5 pc
Bulk Lorentz factor	Γ	1.0
Accretion disk luminosity	L_{disk}	$1.0 \times 10^{-20}\ erg\ s^{-1}$
Blob radius	r_{BLR}	1.2×10^{18} cm
Supermassive blackhole mass	M_{BH}	$4.0 \times 10^{8} M_{\odot}$
Observing angle	θ_{obs}	90°
Redshift	z	0.168

Table 4.2: The input parameters used for the SED fitting of MKAT J221834.96-082253.50 on a single-zone leptonic SSC model. These parameters were assumed based on the multi-wavelength achieves data points (see Tables A.1 and A.2).

Chapter 5

Discussion

This chapter presents an analysis of the results obtained in the preceding chapter, along with the scientific rationale or significance derived from them. Additionally, the map illustrating spectral radiative ageing of MKAT J221834.96-082253.50 is included.

5.1 Radio morphology and interpretation

5.1.1 Identification of the radio core

Based on the resolution of the lobes and the symmetry of MKAT J221834.96-082253.50 shown in Figures 4.5 and 5.1, the core position was determined to be at the J2000 right ascension of $22^h18^m34^s.96$ and the declination of $-08°22'53''.50$. The beam size was convolved ($13.508'' \times 10.024''$) using the CASA task imsmooth to recover the emission around the core region since in the normal beam size it was not well resolved (see Figure 5.1). The infrared (2MASS and WISE) and optical (SDSS DR13) counterparts are located close to the hot-spot on the periphery of the northeast jet (see Figure 4.11, 4.13, and 4.15). This implies that the hot-spot can either be associated with the northeast jet of MKAT J221834.96-082253.50 or be a nearby source interacting with the jet. Therefore, the classification can be certified as a misclassification.

5.1.2 Radio jets

The jets at a resolution of $6.754'' \times 5.012''$ are shown in Figure 4.5. The northeast jet can be traced out to a projected distance of $208.67''$ until the northeast lobe, whereas the southeast jet extends out to a distance of $142.34''$, where they suddenly widen and merge into the southeast lobe. Both jets are initially straight with a position angle $p.a = -6.13°$, and the existence of hot-spots at the northern jet's periphery is also noteworthy (see Figure 4.6).

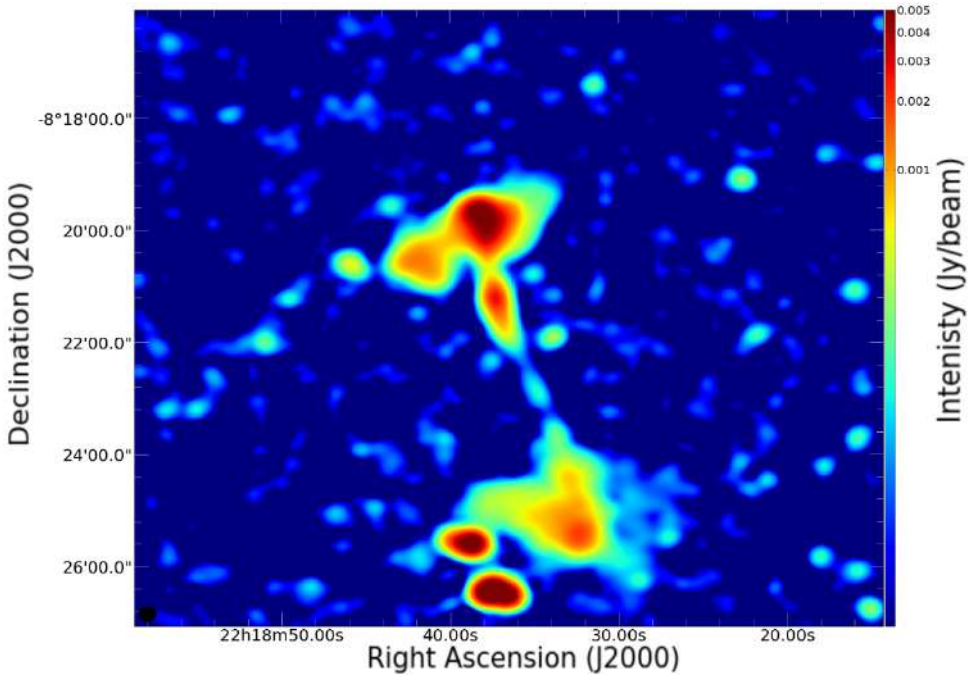

Figure 5.1: The 1.28 GHz MeerkAT image of MKAT J221834.96-082253.50, the beam was convolved and its size is $13.508'' \times 10.024''$.

5.1.3 Radio lobes

Radio lobes are radio emissions created by outflows from the centre of a galaxy and extend outwards on both sides, and the lobes are often much larger than the host galaxy. Two proposed models are used to describe the formation of these radio lobes: (i) Galactic winds propelled by Starburst: these outflows are generated by the supernova explosions in the core, which combine with the stellar winds to create a super-bubble that can be observed as a radio lobe; (ii) jets propelled by AGN. The lobes are quite asymmetric in total emission, extent and distance from the core (see Figure 4.5).

The northern lobe is shaped like an "Axe" with a hot-spot at its edge, while the southern lobe has a faint emission elongated in the west direction and lacks a compact hot-spot; they are two separate compact sources to the southwest of the south lobe. The extended emission observed at 1.28 GHz using the MeerKAT radio telescope has a resemblance to the radio morphology typically associated with FR II radio galaxies, indicating a possibility for supersonic expansion. The radio morphology of MKAT J221834.96-082253.50 shows similarities with the morphology of CygnusA, which is categorised as an FR II radio source.

5.2 Spectral index map

The spectral index is utilised to help interpret the source of the radio emission for each feature. It is an effective tool for exploring how electron energy is related to the IGM and for understanding more about the features of relativistic electrons and the magnetic field in which they radiate.

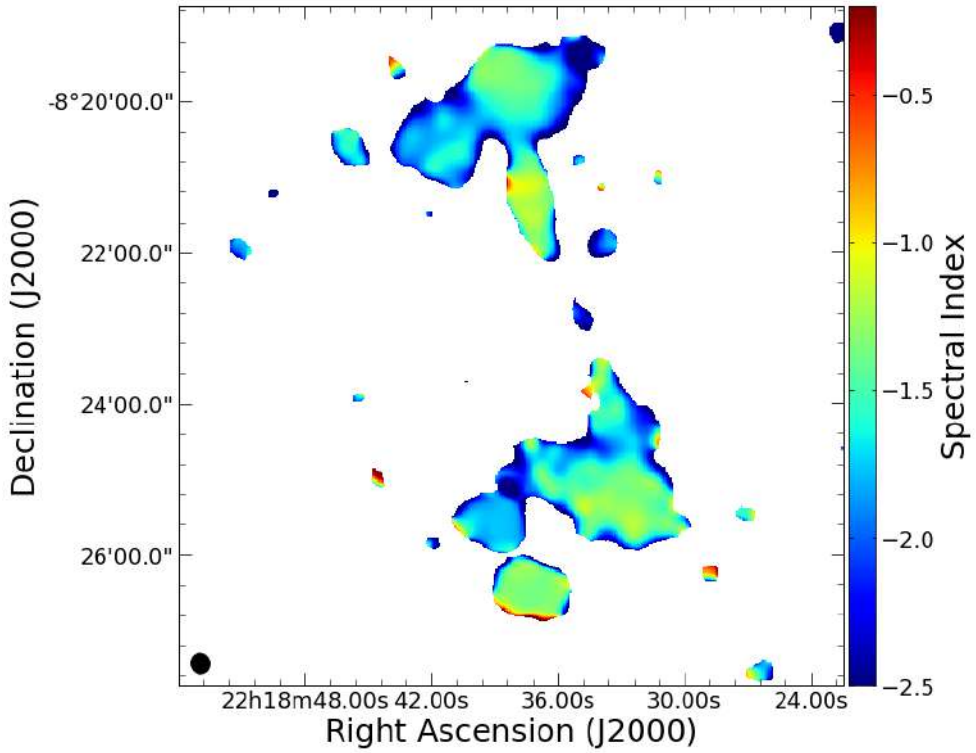

Figure 5.2: The spectral index map of MKAT J221834.96-082253.50 obtained between 909 and 1658 MHz after the beam convolution; the colour bar shows the variation in the spectral index, and the synthesised beam ($13.508'' \times 10.024''$) is shown in a black circle in the lower left corner.

Figure 4.6 and 5.2 shows that the emission in the jets shows spectral indices in the range of $\alpha \sim -1.5$ to -0.5; emission in the central region (core) show the spectral indices ranging from $\alpha \sim -2.5$ to -2.0, and the spectral index within the lobes shows a variation ranging from $\alpha \sim -1.5$ at their inner edges, to $\alpha \sim -2.5$ at the outer edges. The central region shows a steep spectrum which flattens away from the centre. Both lobes contain a combination of flat and steep spectra. Particles in the inner regions have energies consistent with those of a low-energy electron population, whose radio spectrum peaks below MeerKAT's sensitivity range, as shown by their steep spectrum.

It is possible to draw the following conclusion when the steepening occurs: MKAT J221834.96-082253.50 is an evolved source. This means that materials were transported over distances of hundreds of kpc and subsequently returned to the inner regions. The furthest margins of the lobe contain the youngest plasma ("freshly accelerated"), and the sections nearer the centre region contain the oldest plasma ("cooled"). The spectrum of MKAT J221834.96-

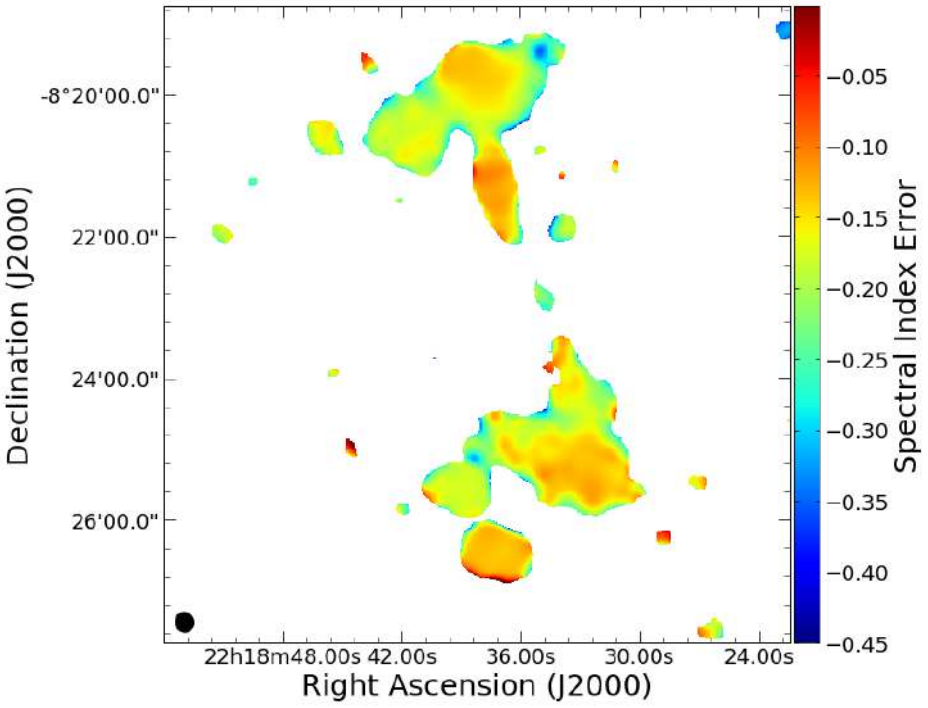

Figure 5.3: The spectral index error map of MKAT J221834.96-082253.50 after the beam convolution, the colour bar shows the variation in the spectral index. The synthesised beam ($13.508'' \times 10.024''$) is visually represented by a black circle located in the lower left corner. This spectral index error map was obtained with a 10% uncertainty of the spectral index (α).

082253.50 presents a steep spectral index at the core, inconsistent with the compact core of FR-II radio galaxies, which typically have a flat spectrum. As a result, the following two distinct possibilities are taken into consideration and summarised in Savini et al. (2018):

- The source has ongoing activity, and the central region reveals a spectral index that is steep compared to what is commonly observed in active radio galaxies. In other words, the assumption that the flat spectrum from the jets, and the steepening/flattening of the spectrum from the lobes can mask the central region, meaning that the active centre may be either steep ($\alpha \sim -0.7$) or flat ($\alpha \sim 0$).

- The source could be an AGN that is fading away, whereby the radio emissions detected in the vicinity of the host galaxy are the oldest. The fundamental components of the source, including the core, lobes, and jets, remain observable. However, the synchrotron spectrum shows a steep spectrum towards the inner regions, which suggests that the central region is no longer providing fresh particles. The fading scenario is evident from the steep spectrum trend seen in the core region.

5.3 Spectral radiative ageing map

In order to get a more comprehensive understanding of the activity history of the radio source, the Broadband Radio Astronomy Tools (BRATS)[1] software package (Harwood et al., 2013, 2015) was used to generate the radiative age map for MKAT J221834.96-082253.50, shown in Figure 5.4. Five (5) convolved beam MeerKAT sub-band images, having the central frequency of 909, 1230, 1337, 1444, and 1658 MHz respectively, were used. The package evaluates the spectral ages of the radio maps by using the spatial region for the source per-pixel basis. To determine the age of MKAT J221834.96-082253.50, the JP model (Jaffe and Perola, 1973) was used. The standard JP model assumes particles with a single injection for an applied power law subjected to a uniform magnetic field with efficient pitch angle scattering.

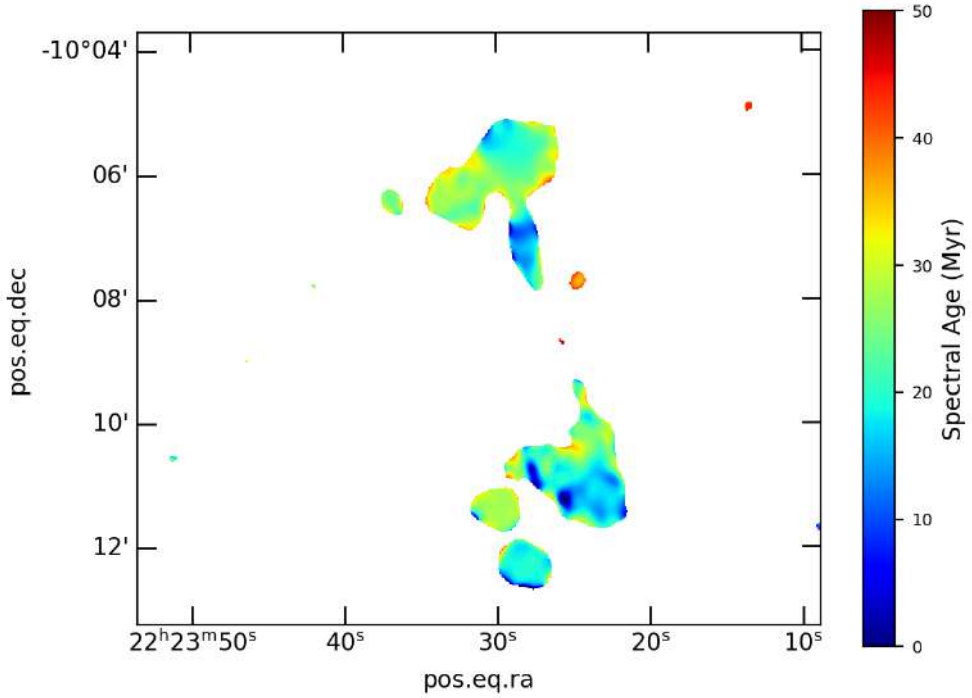

Figure 5.4: The spectral radiative ageing map of MKAT J221834.96-082253.50, fitted using JP model, with an injection index of 0.68. The colour bar indicates the radiative age variation in Mega-years.

A grid search is carried out using the BRATS software package in order to determine the spectral age that best fits the model. The grid is evaluated using a best-fitting age by carrying out a broad search over a range of defined maximum (50 Myr) and minimum (0 Myr) ages. For a more accurate age evaluation, the software automatically repeats the search for the age interval that produced the best fit in the previous cycle until the

[1] http://www.askanastronomer.co.uk/brats/

desired accuracy is reached. For MKAT J221834.96-082253.50, the BRATS package command fitjpmodel was initialised to perform the JP model fitting. In the case of MKAT J221834.96-082253.50, the edges of the lobes have an age of $\sim$ 10 Myr which are the youngest regions, and it increases towards the inner regions. Also, the age of $\sim$ 10 Myr is seen at the position of the hot-spot along the northeast jet. The centre regions have an age of $\sim$ 50 Myr. These findings are in agreement with the scenarios articulated in Section 5.2.

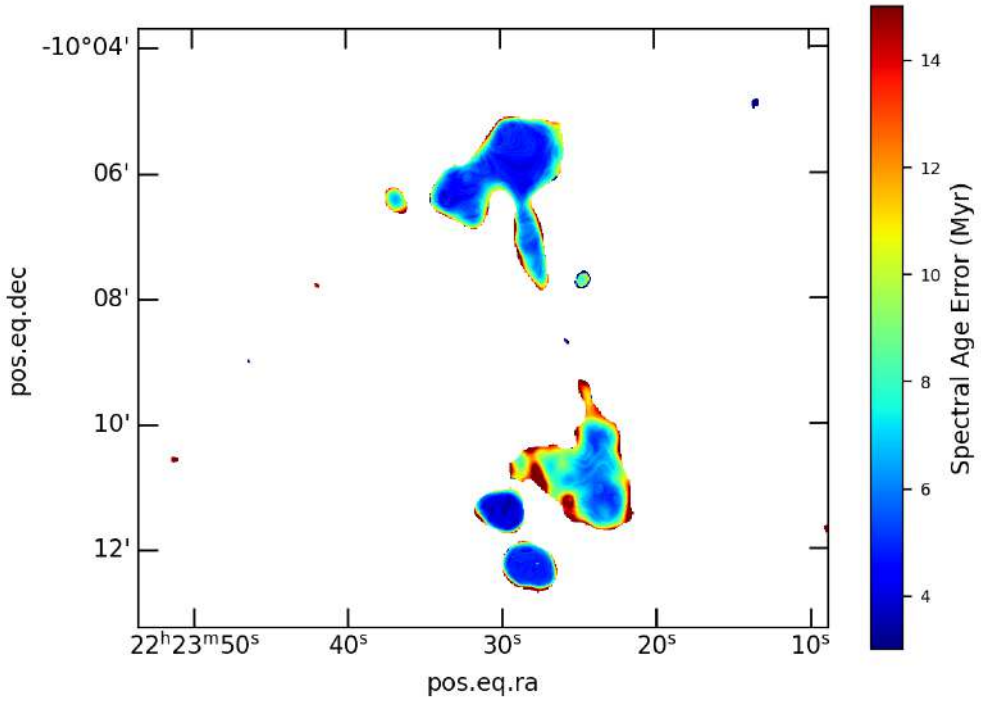

Figure 5.5: The spectral radiative ageing error map of MKAT J221834.96-082253.50, fitted using JP model, with an injection index of 0.68. The colour bar indicates the radiative age error variation in Mega-years.

5.4 Interpretation of the multi-wavelength spectral energy distributions

Synchrotron radiation from electrons is considered to be responsible for the jet radio emission while the high energy emission can be generated through two processes: either through inverse Compton scattering of seed photons by the same electrons or through hadronic processes (Migliori et al., 2013). The double-peaked SEDs structure seen in BL Lacs is similar to the SEDs of radio galaxies.

The overall non-simultaneous multi-wavelength SEDs of the radio galaxy core and hot-spot of MKAT J221834.96-082253.50, obtained from the combination of archival data, are shown in Figures 4.16 and 4.17. A radiative leptonic model that generates emission in a compact region moving along the jet via synchrotron (radio to optical) and SSC (X-ray to the γ-ray) accurately reproduces the SED of the core and hot-spot. The bulk Lorentz factor in this model is set to $\Gamma = 1.0$ and the jetted outflow is observed at an angle of $\theta = 90°$. The co-moving radius of the jet emission zone is 11.2×10^{18} cm with the mean magnetic field of $B = 0.25$ G in the radiating plasma. The escape time parameter was set to $\eta_{esc} = 0.25$ and this indicates that the emission region is not spherical symmetry. The inconsistencies between the model and measurements in optical fluxes indicate a variable source or potential sources not associated with the radio galaxy or hot-spot. The X-ray spectrum shape is well-reproduced by the SSC hump. The upper limit is from the Fermi Large Area Telescope (LAT) 10-year Source DR2 catalog (Abdollahi et al., 2020). The inverse Compton component of the core and hot-spot emissions are poorly constrained due to insufficient high-frequency data in the hard X-ray and gamma-ray regions.

Chapter 6

Summary and Conclusion

In this thesis, the aim was to perform a multi-wavelength study of radio galaxies. This study used the fields from the MeerTRAP[1] science project, as depicted in Table 3.1, which were observed by the MeerKAT radio telescope (see Chapter 3), and the available archived data. The main findings from Chapter 4 are summarised below.

MKAT J221834.96-082253.50 was the only radio source selected from forty-two (42) radio sources due to its well-resolved radio morphology and the X-ray band counterparts. The physical properties of the radio-loud galaxy MKAT J221834.96- 082253.50 at various wavelengths were intensely investigated and studied. MKAT J221834.96-082253.50 is a bright radio source with strong double-sided jets, bent lobe emission at the radio band and has the characteristics of an active galaxy. The radio contours from the MeerKAT radio continuum image were superimposed on the VLA image from NVSS (see Figure 4.9); on the infrared image (see Figures 4.11 and 4.13) from 2MASS and WISE, and on the optical image (see Figure 4.15) from SDSS. The position of the core/central region is at J2000 right ascension $22^h18^m34^s.96$ and the declination $-08°22'53''.50$ while the hot-spot region is at right ascension $22^h18^m37^s.64$ and the declination $-08°21'12''.80$. The hot-spot identification on the periphery of the northeast jet of MKAT J221834.96-082253.50, in the infrared and optical bands from the archive, was ruled a misclassification based on the factors outlined in Section 5.1.1.

The spectral index distribution (see Figures 4.6 and 5.2) of MKAT J221834.96-082253.50 was calculated using eight (8) different sub-band FITS images with the central frequency between 909 and 1658 MHz. This distribution reveals a spectral index of $\alpha \sim -2.5$ to -2.0, which is steep in the inner jet regions, and it flattens ($\alpha \sim -1.5$ to 1.0) outwards. The spectral index at the lobes is mixed; most inner regions are flat ($\alpha \sim 1.0$) and the edges are steep ($\alpha \sim 2.0$). The spectral radiative age map of MKAT J221834.96-082253.50 was generated from a Jaffe and Perola (1973) (JP) model, using the BRATS software package, and it reveals that the age at the core region is older than at the jets and lobes (see Figure

[1] https://www.meertrap.org/

5.4). The finding of the steep spectral index at the radio galaxy's core or nucleus is similar to the work done by Shulevski et al. (2015), Shulevski et al. (2017) and Savini et al. (2018), on VLSS J1431.8+1331, B2 0924+30, and MaxBCG J199, respectively. Their spectral index at the core/nucleus for each radio source was $\alpha \sim -1.2$, $\alpha \sim -1.4$, and $\alpha \sim -1.3$, respectively. According to their work, the source could be identified either as an AGN remnant, which is a relic from its previous state as an active radio galaxy, or the core region has a steeper spectrum compared to typical active radio galaxies. Alternatively, the source may be indicative of a dying AGN. In the framework of AGN, this steep spectral index around the radio core is rare.

The archival[2] multi-wavelength data of MKAT J221834.96-082253.50 were combined to build the non-simultaneous broadband spectral energy distributions of MKAT J221834.96-082253.50 (see Figures 4.16 and 4.17). The one-zone leptonic SSC model of Böttcher et al. (2013) was used to fit the SED and the parameters of the fitted model are presented in Table 4.1. The broadband SED model of MKAT J221834.96-082253.50 shows a double-humped feature (the one in low frequencies is due to synchrotron and the one in high frequencies is due to SCC). The upper limit at HE gamma-rays presented in Figures 4.16 and 4.17 is the flux threshold $\sim 2 \times 10^{11}$ erg cm^{-2} s^{-1} of 4FGL-DR2 Fermi-LAT catalog (Abdollahi et al., 2020).

In conclusion, this thesis demonstrates the phenomenon of multi-wavelength study, along with the analysis of spectral index and radiative ageing. MKAT J221834.96-082253.50 is not prominent, and because of this constraint, the SED has insufficient archival data across the electromagnetic spectrum. Further in-depth analysis of the mechanisms of particle acceleration and photon emission within MKAT J221834.96-082253.50 requires longer-term observations with more sensitive instruments.

[2] http://ned.ipac.caltech.edu/

Bibliography

Abdollahi, S., Acero, F., Ackermann, M., Ajello, M., Atwood, W., Axelsson, M., Baldini, L., Ballet, J., Barbiellini, G., Bastieri, D., et al. (2020). Fermi Large Area Telescope fourth source catalog. *The Astrophysical Journal Supplement Series*, 247(1):33.

Ade, P. A., Aghanim, N., Arnaud, M., Ashdown, M., Aumont, J., Baccigalupi, C., Banday, A., Barreiro, R., Bartlett, J., Bartolo, N., et al. (2016). Planck 2015 results-xiii. cosmological parameters. *Astronomy & Astrophysics*, 594:A13.

Agarwal, A., Mihov, B., Andruchow, I., Cellone, S. A., Anupama, G., Agrawal, V., Zola, S., Slavcheva-Mihova, L., Özdönmez, A., Ege, E., et al. (2021). Multi-band behaviour of the TeV blazar PG 1553+ 113 in optical range on diverse timescales-Flux and spectral variations. *Astronomy & Astrophysics*, 645:A137.

Ahn, C. P., Alexandroff, R., Prieto, C. A., Anderson, S. F., Anderton, T., Andrews, B. H., Aubourg, É., Bailey, S., Balbinot, E., Barnes, R., et al. (2012). The ninth data release of the Sloan Digital Sky Survey: first spectroscopic data from the SDSS-III Baryon Oscillation Spectroscopic Survey. *The Astrophysical Journal Supplement Series*, 203(2):21.

Albareti, F. D., Prieto, C. A., Almeida, A., Anders, F., Anderson, S., Andrews, B. H., Aragón-Salamanca, A., Argudo-Fernández, M., Armengaud, E., Aubourg, E., et al. (2017). The 13th data release of the Sloan Digital Sky Survey: First spectroscopic data from the SDSS-IV survey mapping nearby galaxies at Apache Point Observatory. *The Astrophysical Journal Supplement Series*, 233(2):25.

Bardeen, J. M. and Petterson, J. A. (1975). The Lense-Thirring effect and accretion disks around kerr black holes. *The Astrophysical Journal*, 195:L65.

Beckmann, V. and Shrader, C. (2013a). *Active galactic nuclei*. John Wiley & Sons.

Beckmann, V. and Shrader, C. R. (2013b). The AGN phenomenon: open issues. *arXiv preprint arXiv:1302.1397*.

Best, P. N., Kauffmann, G., Heckman, T. M., and Ivezić, Ž. (2005). A sample of radio-loud active galactic nuclei in the Sloan Digital Sky Survey. , 362(1):9–24.

Birkinshaw, M. (1999). The Sunyaev–Zel'dovich effect. *Physics Reports*, 310(2-3):97–195.

Blandford, R., Meier, D., and Readhead, A. (2019). Relativistic jets from active galactic nuclei. *Annual Review of Astronomy and Astrophysics*, 57:467–509.

Blandford, R. and Payne, D. (1982). Hydromagnetic flows from accretion discs and the production of radio jets. *Monthly Notices of the Royal Astronomical Society*, 199(4):883–903.

Boccardi, B., Krichbaum, T., Ros, E., and Zensus, J. (2017). Radio observations of active galactic nuclei with mm-VLBI. *The Astronomy and Astrophysics Review*, 25(1):1–48.

Booth, R., De Blok, W., Jonas, J., and Fanaroff, B. (2009). MeerKAT key project science, specifications, and proposals. *arXiv preprint arXiv:0910.2935*.

Böttcher, M., Harris, D. E., and Krawczynski, H. (2012). *Relativistic jets from active galactic nuclei*. John Wiley and Sons.

Böttcher, M., Reimer, A., Sweeney, K., and Prakash, A. (2013). Leptonic and hadronic modeling of Fermi-detected blazars. *The Astrophysical Journal*, 768(1):54.

Bowen, I. and Vaughan, A. (1973). The optical design of the 40-in. telescope and of the Irenee DuPont telescope at Las Campanas Observatory, Chile. *Applied Optics*, 12(7):1430–1435.

Burke, B. F., Graham-Smith, F., and Wilkinson, P. N. (2019). *An introduction to radio astronomy*. Cambridge University Press.

Chen, X., Wang, S., Deng, L., de Grijs, R., and Yang, M. (2018). Wide-field Infrared Survey Explorer (WISE) catalog of periodic variable stars. *The Astrophysical Journal Supplement Series*, 237(2):28.

Chibueze, J. O., Caleb, M., Spitler, L., Ashkar, H., Schussler, F., Stappers, B., Venter, C., Heywood, I., Richards, A., Williams, D., et al. (2022). A MeerKAT, e-MERLIN, H.E.S.S. and Swift search for persistent and transient emission associated with three localised FRBs. *arXiv preprint arXiv:2201.00069*.

Condon, J. J., Cotton, W., Greisen, E., Yin, Q., Perley, R. A., Taylor, G., and Broderick, J. (1998). The NRAO VLA sky survey. *The Astronomical Journal*, 115(5):1693.

Condon, J. J. and Ransom, S. M. (2016). *Essential radio astronomy*. Princeton University Press.

Courvoisier, T. J.-L. (2001). What May We Learn from Multi-Wavelength Observations of Active Galactic Nuclei. In *Quasars, AGNs and Related Research Across 2000*, pages 155–164. Springer.

Delhaize, J., Heywood, I., Prescott, M., Jarvis, M. J., Delvecchio, I., Whittam, I. H., White, S. V., Hardcastle, M. J., Hale, C. L., Afonso, J., et al. (2021). MIGHTEE: are giant radio galaxies more common than we thought? *Monthly Notices of the Royal Astronomical Society*, 501(3):3833–3845.

Dermer, C., Schlickeiser, R., and Mastichiadis, A. (1992). High-energy gamma radiation from extragalactic radio sources. *Astronomy and Astrophysics*, 256:L27–L30.

Diltz, C. and Boettcher, M. (2016). Leptonic and lepto-hadronic modeling of the 2010 November flare from 3C 454.3. *The Astrophysical Journal*, 826(1):54.

D'Onofrio, M., Marziani, P., and Sulentic, J. W. (2012). *Fifty years of quasars: from early observations and ideas to future research*, volume 386. Springer Science & Business Media.

EHT Collaboration, E. H. T., Akiyama, K., Alberdi, A., Alef, W., Asada, K., AZULY, R., et al. (2019). First M87 event horizon telescope results. I. The shadow of the supermassive black hole. *Astrophys. J. Lett*, 875(1):L1.

Falcke, H., Melia, F., and Agol, E. (1999). Viewing the shadow of the black hole at the galactic center. *The Astrophysical Journal*, 528(1):L13.

Fanaroff, B. L. and Riley, J. M. (1974). The morphology of extragalactic radio sources of high and low luminosity. *Monthly Notices of the Royal Astronomical Society*, 167(1):31P–36P.

Foley, A., Alberts, T., Armstrong, R., Barta, A., Bauermeister, E., Bester, H., Blose, S., Booth, R., Botha, D., Buchner, S., et al. (2016). Engineering and science highlights of the KAT-7 radio telescope. *Monthly Notices of the Royal Astronomical Society*, 460(2):1664–1679.

Garofalo, D. and Singh, C. B. (2019). FR0 radio galaxies and their place in the radio morphology classification. *The Astrophysical Journal*, 871(2):259.

Gültekin, K., Richstone, D. O., Gebhardt, K., Lauer, T. R., Tremaine, S., Aller, M. C., Bender, R., Dressler, A., Faber, S., Filippenko, A. V., et al. (2009). The M–σ and M–L relations in galactic bulges, and determinations of their intrinsic scatter. *The Astrophysical Journal*, 698(1):198.

Gunn, J. E., Siegmund, W. A., Mannery, E. J., Owen, R. E., Hull, C. L., Leger, R. F., Carey, L. N., Knapp, G. R., York, D. G., Boroski, W. N., et al. (2006). The 2.5 m telescope of the sloan digital sky survey. *The Astronomical Journal*, 131(4):2332.

H. E. S. S. Collaboration, Abdalla, et al. (2018). The γ-ray spectrum of the core of Centaurus A as observed with H.E.S.S. and Fermi-LAT. , 619:A71.

Hardcastle, M., Harris, D., Worrall, D., and Birkinshaw, M. (2004). The origins of X-Ray emission from the hot spots of FR II radio sources. *The Astrophysical Journal*, 612(2):729.

Harwood, J. J., Hardcastle, M. J., and Croston, J. H. (2015). Spectral ageing in the lobes of cluster-centre FR II radio galaxies. *Monthly Notices of the Royal Astronomical Society*, 454(4):3403–3422.

Harwood, J. J., Hardcastle, M. J., Croston, J. H., and Goodger, J. L. (2013). Spectral ageing in the lobes of FR-II radio galaxies: new methods of analysis for broad-band radio data. *Monthly Notices of the Royal Astronomical Society*, 435(4):3353–3375.

Heywood, I. (2020). oxkat: Semi-automated imaging of MeerKAT observations. *Astrophysics Source Code Library*, pages ascl–2009.

Hughes, P., Aller, H., and Aller, M. (1991). Synchrotron emission from shocked relativistic jets. III-Models for the centimeter wave band quiescent and burst emission from 3C 279 and OT 081. *The Astrophysical Journal*, 374:57–71.

Jaffe, W. and Perola, G. (1973). Dynamical models of tailed radio sources in clusters of galaxies. *Astronomy and Astrophysics*, 26:423.

Jonas, J. and MeerKAT Team (2016). The MeerKAT Radio Telescope. In *MeerKAT Science: On the Pathway to the SKA*, page 1.

Kenyon, J., Smirnov, O., Grobler, T., and Perkins, S. (2018). CUBICAL–fast radio interferometric calibration suite exploiting complex optimization. *Monthly Notices of the Royal Astronomical Society*, 478(2):2399–2415.

Kerr, R. P. (1963). Gravitational field of a spinning mass as an example of algebraically special metrics. *Physical review letters*, 11(5):237.

Kormendy, J., Bender, R., and Cornell, M. (2011). Supermassive black holes do not correlate with galaxy disks or pseudobulges. *Nature*, 469(7330):374–376.

Koulouridis, E., Plionis, M., Chavushyan, V., Dultzin, D., Krongold, Y., Georgantopoulos, I., and León-Tavares, J. (2013). Activity of the Seyfert galaxy neighbours. *Astronomy & Astrophysics*, 552:A135.

Laing, R. and Bridle, A. (2002). Relativistic models and the jet velocity field in the radio galaxy 3c 31. *Monthly notices of the royal Astronomical Society*, 336(1):328–352.

Leckrone, D. S. (2020). From Darkness to Light: Black Holes and Quasars. In *Life With Hubble: An insider's view of the world's most famous telescope*. IOP Publishing.

Magorrian, J., Tremaine, S., Richstone, D., Bender, R., Bower, G., Dressler, A., Faber, S., Gebhardt, K., Green, R., Grillmair, C., et al. (1998). The demography of massive dark objects in galaxy centres. *The Astronomical Journal*, 115(6):2285.

Maini, A. (2016). Modelling the faint radio sky: the pathway to ska.

Marscher, A. P., Jorstad, S. G., Larionov, V. M., Aller, M. F., Aller, H. D., Lähteenmäki, A., Agudo, I., Smith, P. S., Gurwell, M., Hagen-Thorn, V. A., et al. (2010). Probing the inner jet of the quasar PKS 1510- 089 with multi-waveband monitoring during strong gamma-ray activity. *The Astrophysical Journal Letters*, 710(2):L126.

McMullin, J. P., Waters, B., Schiebel, D., Young, W., and Golap, K. (2007). CASA architecture and applications. In *Astronomical data analysis software and systems XVI*, volume 376, page 127.

Meisenheimer, K., Roser, H.-J., Hiltner, P., Yates, M., Longair, M., Chini, R., and Perley, R. (1989). The synchrotron spectra of radio hot spots. *Astronomy and Astrophysics*, 219:63–86.

Meyer, E. T., Fossati, G., Georganopoulos, M., and Lister, M. L. (2012). Collective evidence for inverse compton emission from external photons in high-power blazars. *The Astrophysical Journal Letters*, 752(1):L4.

Migliori, G., Siemiginowska, A., Kelly, B., Celotti, A., Begelman, M., et al. (2013). Jet emission in young radio sources: a Fermi Large Area Telescope gamma-ray view. *The Astrophysical Journal*, 780(2):165.

Montani, G. and Petitta, J. (2014). Plasma phenomenology in astrophysical systems: Radio-sources and jets. *Physics of Plasmas*, 21(6):061502.

Netzer, H. and Woltjer, L. (1990). *Active Galactic Nuclei*. Springer-Verlag.

Offringa, A., McKinley, B., Hurley-Walker, N., Briggs, F., Wayth, R., Kaplan, D., Bell, M., Feng, L., Neben, A., Hughes, J., et al. (2014). WSCLEAN: an implementation of a fast, generic wide-field imager for radio astronomy. *Monthly Notices of the Royal Astronomical Society*, 444(1):606–619.

Offringa, A. and Smirnov, O. (2017). An optimized algorithm for multiscale wideband deconvolution of radio astronomical images. *Monthly Notices of the Royal Astronomical Society*, 471(1):301–316.

Pacholczyk, A. (1970). Radio Astrophysics. Nonthermal Processes in Galactic and Extragalactic Sources. Freeman & Co., San Francisco.

Pacholczyk, A. G. (2014). *Radio galaxies: Radiation transfer, dynamics, stability and evolution of a synchrotron plasmon*. Elsevier.

Rees, M. J. and Ostriker, J. (1977). Cooling, dynamics and fragmentation of massive gas clouds: clues to the masses and radii of galaxies and clusters. *Monthly Notices of the Royal Astronomical Society*, 179(4):541–559.

Rix, H.-W., Barden, M., Beckwith, S. V., Bell, E. F., Borch, A., Caldwell, J. A., Häussler, B., Jahnke, K., Jogee, S., McIntosh, D. H., et al. (2004). GEMS: galaxy evolution from morphologies and SEDs. *The Astrophysical Journal Supplement Series*, 152(2):163.

Rohlfs, K. and Wilson, T. L. (2013). *Tools of radio astronomy*. Springer Science & Business Media.

Rosswog, S. and Bruggen, M. (2003). Introduction to high-energy astrophysics. *Introduction to High-Energy Astrophysics*, page 376.

Rybicki, Lightman, R., and Lightman, A. (1979). Radiative Processes in Astrophysics Wiley Interscience.

Rybicki, G. B. and Lightman, A. P. (1991). *Radiative processes in astrophysics*. John Wiley & Sons.

Ryle, M., Hewish, A., and Shakeshaft, J. (1959). The synthesis of large radio telescopes by the use of radio interferometers. *IRE Transactions on Antennas and Propagation*, 7(5):120–124.

Savini, F., Bonafede, A., Brüggen, M., Wilber, A., Harwood, J. J., Murgia, M., Shimwell, T., Rafferty, D., Shulevski, A., Brienza, M., et al. (2018). Studying the late evolution of a radio-loud AGN in a galaxy group with LOFAR. *Monthly Notices of the Royal Astronomical Society*, 474(4):5023–5035.

SDSS Collaboration, Albareti, F. D., Allende Prieto, et al. (2016). The Thirteenth Data Release of the Sloan Digital Sky Survey: First Spectroscopic Data from the SDSS-IV Survey MApping Nearby Galaxies at Apache Point Observatory. *arXiv e-prints*, page arXiv:1608.02013.

Seidu, M. (2020). Variability of Methanol and OH Masers Associated with the Star Forming Region g339.62-0.12. Master's thesis, North-West Uiversity, Potchefstroom Campus.

Shulevski, A., Morganti, R., Barthel, P., Harwood, J., Brunetti, G., Van Weeren, R., Röttgering, H., White, G., Horellou, C., Kunert-Bajraszewska, M., et al. (2015). AGN duty cycle estimates for the ultra-steep spectrum radio relic VLSS J1431. 8+ 1331. *Astronomy & Astrophysics*, 583:A89.

Shulevski, A., Morganti, R., Harwood, J., Barthel, P., Jamrozy, M., Brienza, M., Brunetti, G., Röttgering, H., Murgia, M., White, G., et al. (2017). Radiative age mapping of the remnant radio galaxy B2 0924+ 30: the LOFAR perspective. *Astronomy & Astrophysics*, 600:A65.

Sikora, M., Begelman, M. C., and Rees, M. J. (1994). Comptonization of diffuse ambient radiation by a relativistic jet: The source of gamma rays from blazars? *The Astrophysical Journal*, 421:153–162.

Skrutskie, M., Cutri, R., Stiening, R., Weinberg, M., Schneider, S., Carpenter, J., Beichman, C., Capps, R., Chester, T., Elias, J., et al. (2006). The two micron all sky survey (2MASS). *The Astronomical Journal*, 131(2):1163.

Sokolovsky, K., Schinzel, F., Tanaka, Y., Abolmasov, P., Angelakis, E., Bulgarelli, A., Carrasco, L., Cenko, S., Cheung, C., Clubb, K., et al. (2014). Two active states of the narrow-line gamma-ray-loud AGN GB 1310+ 487. *Astronomy & Astrophysics*, 565:A26.

Takey, A., Schwope, A., and Lamer, G. (2013). The 2XMMi/SDSS Galaxy Cluster Survey. II. The optically confirmed cluster sample and the L_X - T relation. , 558:A75.

Tavecchio, F., Becerra-Gonzalez, J., Ghisellini, G., Stamerra, A., Bonnoli, G., Foschini, L., and Maraschi, L. (2011). On the origin of the γ-ray emission from the flaring blazar PKS 1222+ 216. *Astronomy & Astrophysics*, 534:A86.

Thompson, A. R., Moran, J. M., and Swenson, G. W. (2017). *Interferometry and synthesis in radio astronomy*. Springer Nature.

Urry, C. M. and Padovani, P. (1995). Unified schemes for radio-loud active galactic nuclei. *Publications of the Astronomical Society of the Pacific*, 107(715):803.

Venugopal, V. and Bhagdikar, P. S. (2012). de Broglie Wavelength and Frequency of the Scattered Electrons in Compton Effect. *arXiv preprint arXiv:1202.4572*.

VERITAS Collaboration, o. (2010). VERITAS 2008-2009 monitoring of the variable gamma-ray source M87. *The Astrophysical journal*, 716(1):819–824.

Wang, D., Zhang, Y.-x., and Zhao, Y.-h. (2008). An automatic system for photometric redshift estimation based on sky survey data. In *Advanced Software and Control for Astronomy II*, volume 7019, pages 1077–1084. SPIE.

Watson, M. G., Schröder, A., Fyfe, D., Page, C. G., Lamer, G., Mateos, S., Pye, J., Sakano, M., Rosen, S., Ballet, J., et al. (2009). The XMM-Newton serendipitous survey-V. The Second XMM-Newton serendipitous source catalogue. *Astronomy & Astrophysics*, 493(1):339–373.

Webb, S. (2012). *New eyes on the universe: twelve cosmic mysteries and the tools we need to solve them*. Springer Science & Business Media.

Wright, E. L., Eisenhardt, P. R., Mainzer, A. K., Ressler, M. E., Cutri, R. M., Jarrett, T., Kirkpatrick, J. D., Padgett, D., McMillan, R. S., Skrutskie, M., et al. (2010). The Wide-field Infrared Survey Explorer (WISE): mission description and initial on-orbit performance. *The Astronomical Journal*, 140(6):1868.

Wrobel, J. and Walker, R. (1999). Sensitivity. In *Synthesis imaging in radio astronomy II*, volume 180, page 171.

Xmm-Newton Survey Science Centre, C. (2008). VizieR Online Data Catalog: The XMM-Newton 2nd Incremental Source Catalogue (2XMMi) (XMM-SSC, 2008). *VizieR Online Data Catalog*, page IX/40.

Yang, X.-H. and Bu, D.-F. (2018). Effect of nuclear stars gravity on quasar radiation feedback on the parsec-scale. *Monthly Notices of the Royal Astronomical Society*, 478(3):2887–2895.

Appendix A

Appendix

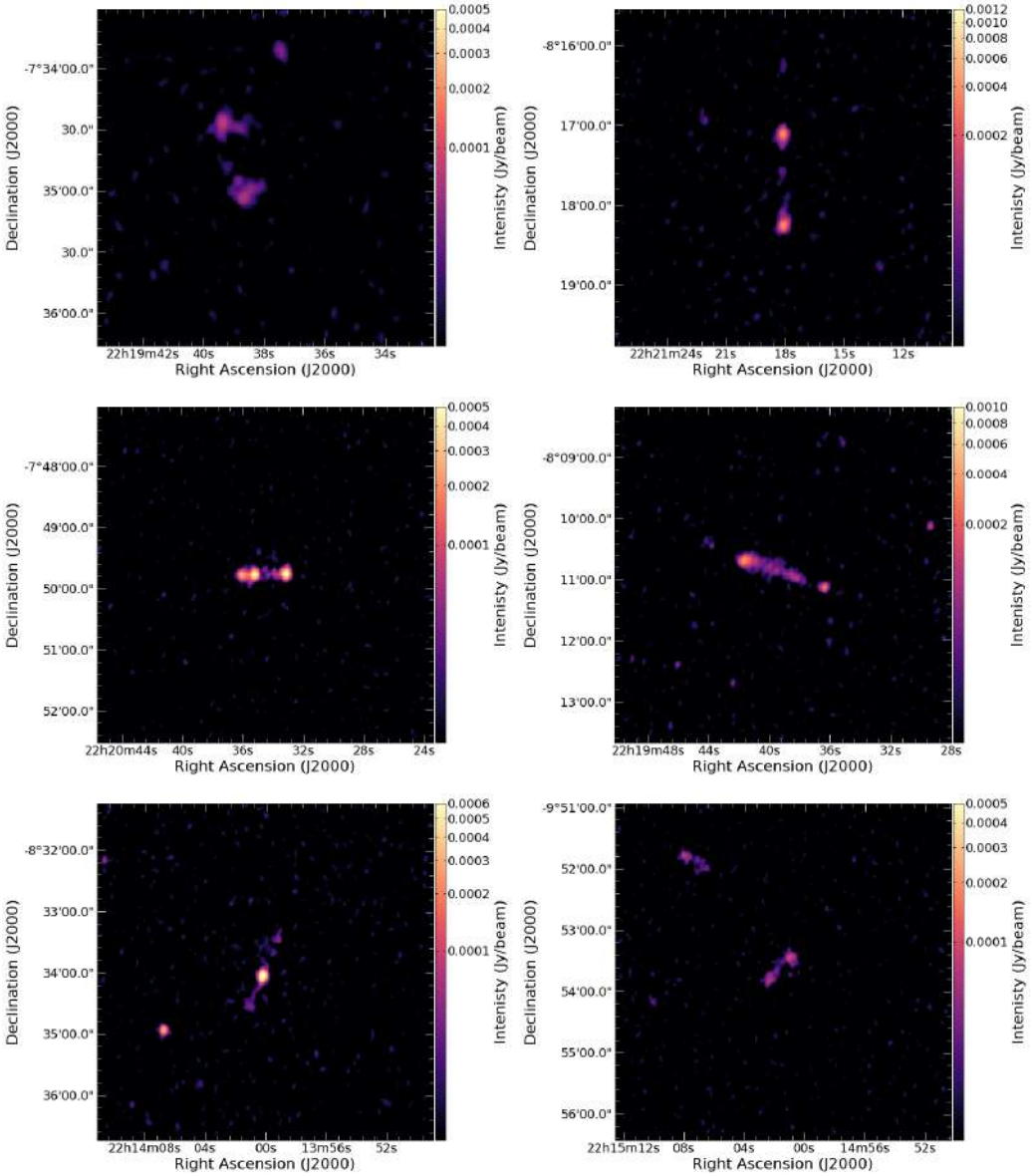

Figure A.1: The interesting radio galaxies from FRB 20171019A field.

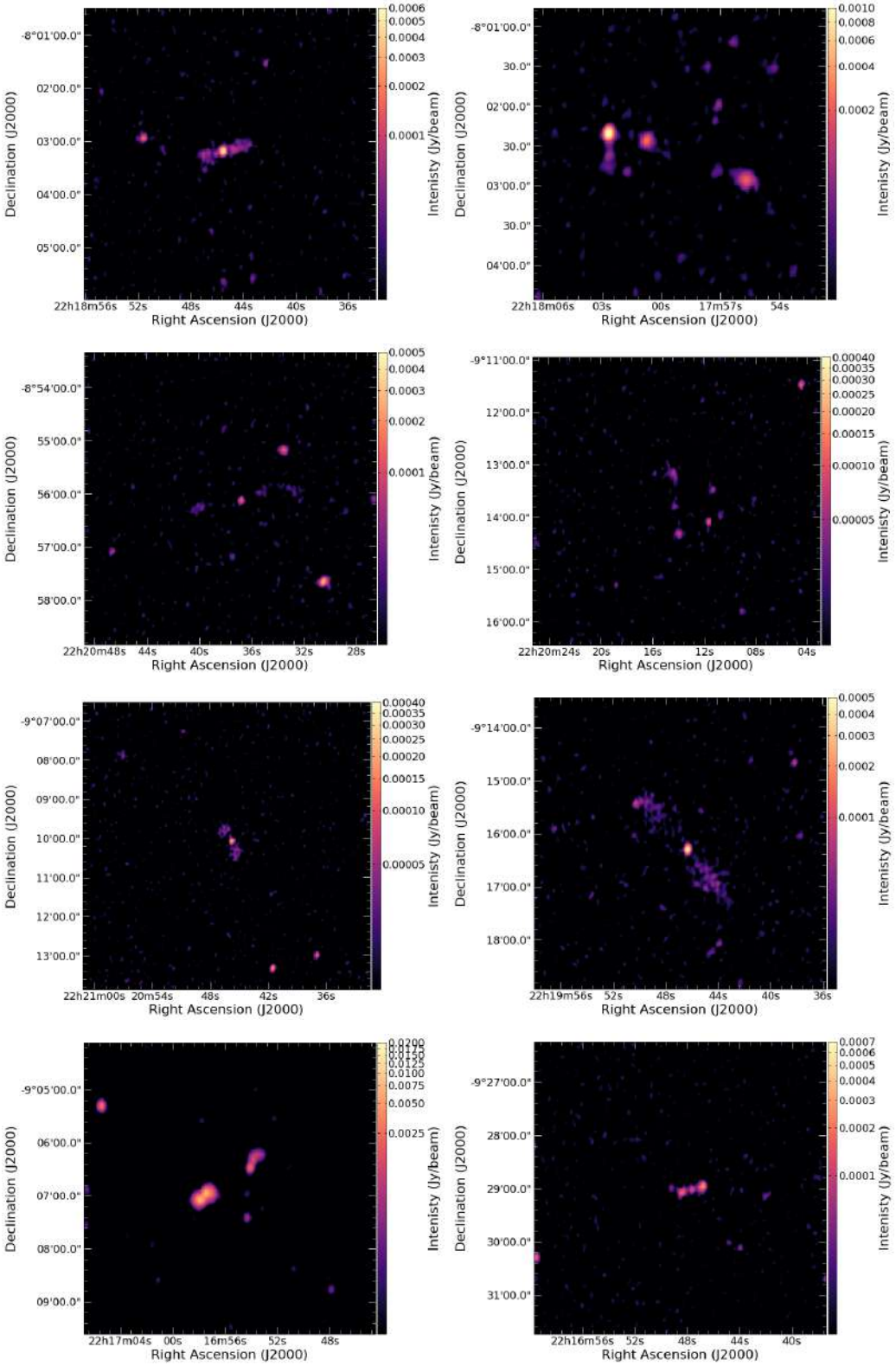

Figure A.2: The interesting radio galaxies from FRB 20171019A field.

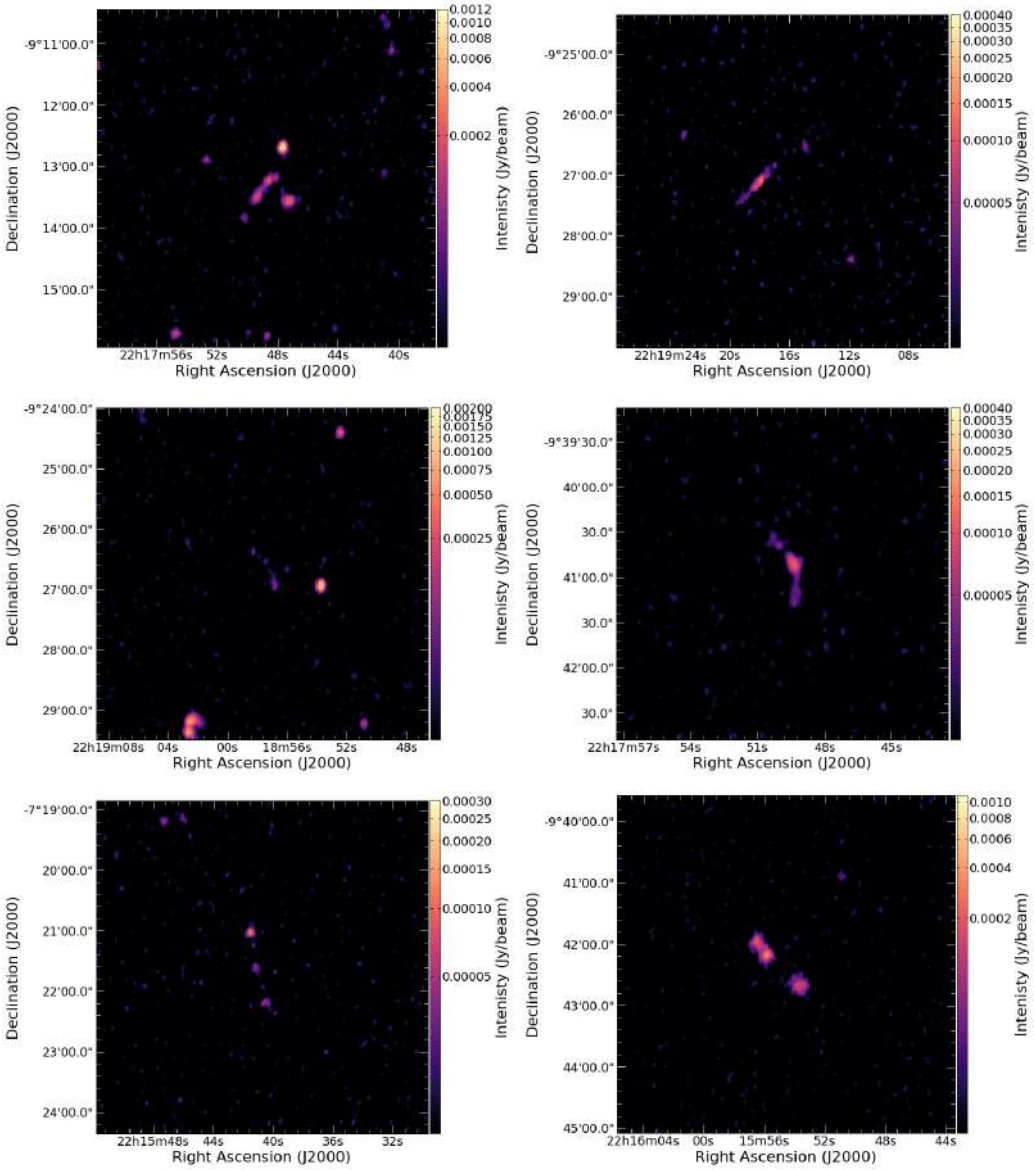

Figure A.3: The interesting radio galaxies from FRB 20171019A field.

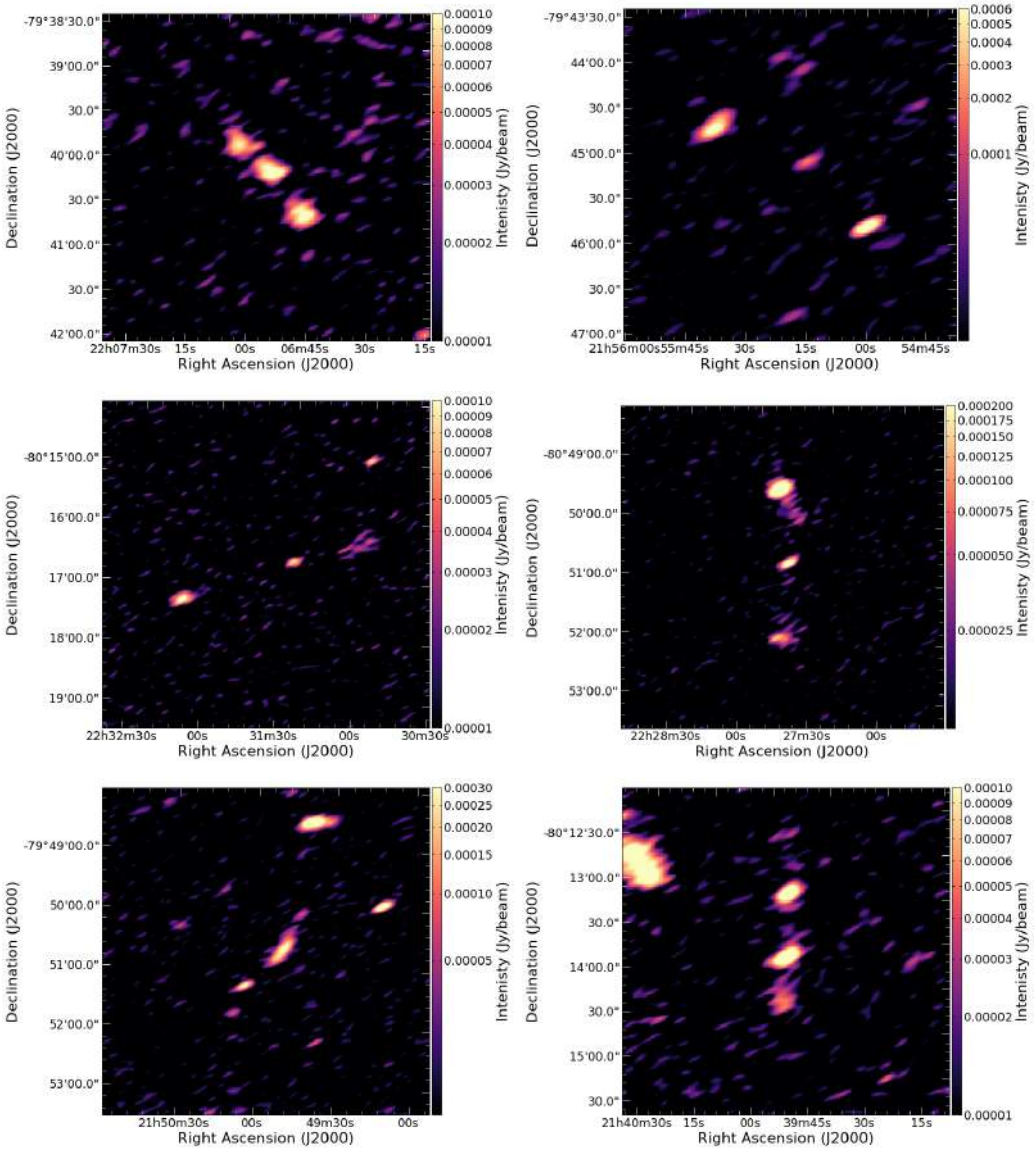

Figure A.4: The interesting radio galaxies from FRB 20190711A field.

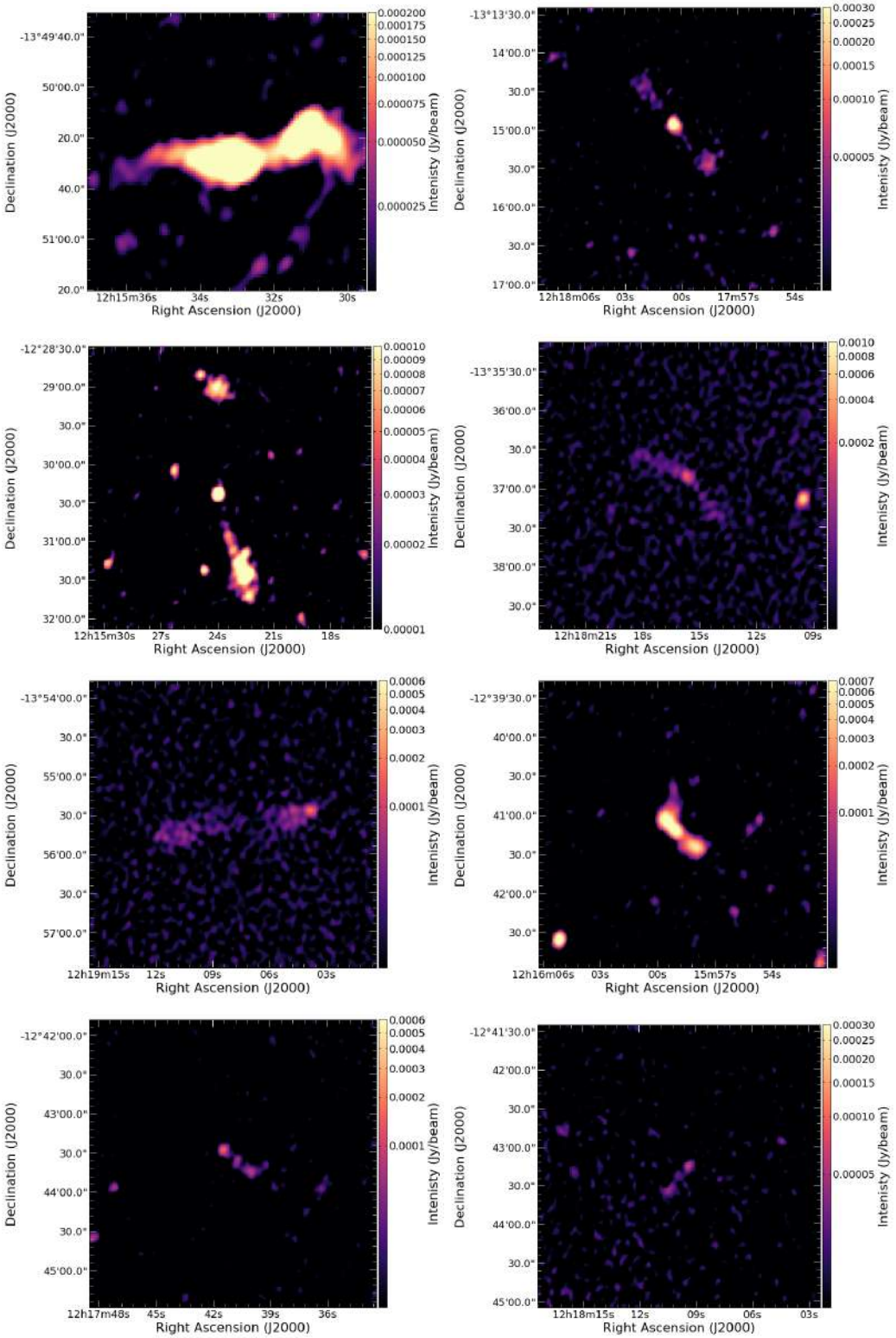

Figure A.5: The interesting radio galaxies from FRB 20190714A field.

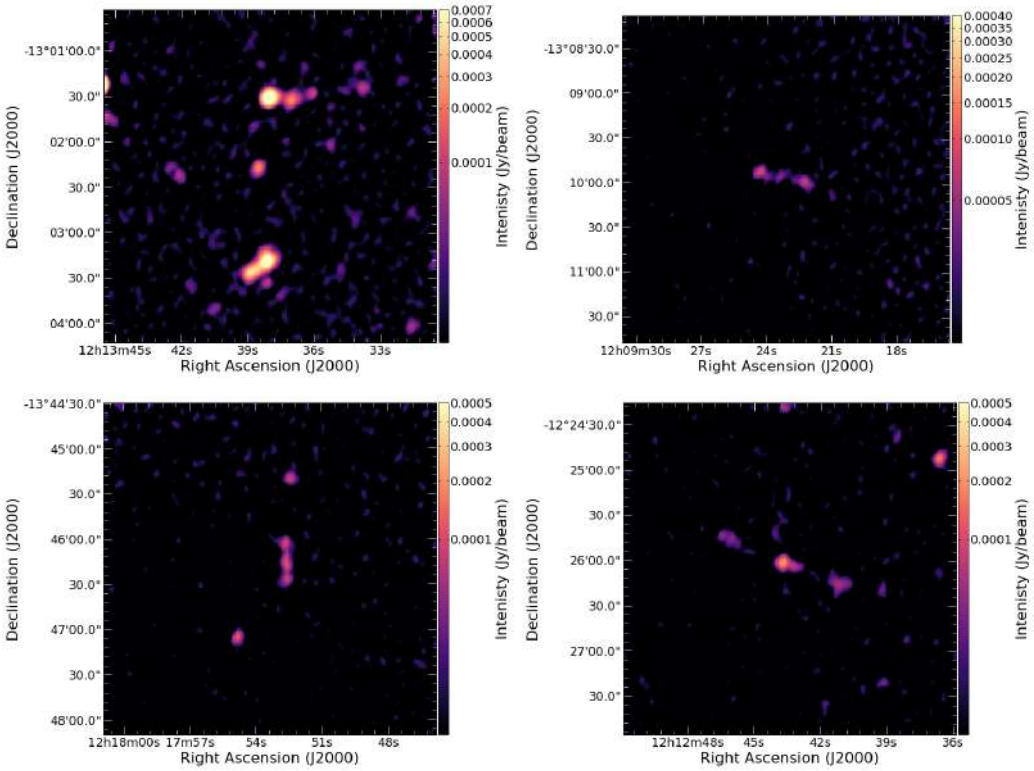

Figure A.6: The interesting radio galaxies from FRB 20190714A field.

The achieves data points for central/core region		
NVSS (radio band) [Offset (RA = 1.63″, DEC = 2.15″)]		
Frequency [Hz]	Flux [Jy Hz]	Flux_error [Jy Hz]
1.4000×10^{9}	6.3060×10^{6}	8.9986×10^{5}
SDSS Release 9 (optical band) [Offset (RA = 5.64″, DEC = 0.42″)]		
8.4420×10^{14}	2.8554×10^{10}	1.5006×10^{8}
6.3976×10^{14}	3.5484×10^{10}	3.3385×10^{8}
4.8628×10^{14}	9.9934×10^{10}	3.4938×10^{8}
4.0074×10^{14}	3.4205×10^{11}	5.0408×10^{8}
3.3568×10^{14}	5.2620×10^{11}	1.8420×10^{9}
2XMMi source (X-ray band) [Offset (RA = 9.50″, DEC = 10.99″)]		
8.4629×10^{16}	1.7771×10^{8}	9.9751×10^{7}
1.8134×10^{17}	2.5847×10^{8}	1.4955×10^{8}
3.6270×10^{17}	3.5957×10^{8}	1.5050×10^{8}
7.8586×10^{17}	5.5845×10^{7}	1.6596×10^{7}
1.9948×10^{18}	5.8951×10^{8}	1.7079×10^{8}
Fermi-LAT 10-year Source DR2 (γ-ray band)		
2.4180×10^{23}	2.0000×10^{11}	1.0520×10^{11}

Table A.1: The achieves data points for the central/core region. The catalogues used to obtain these data points were accessed using SAOImage DS9. The offset direction is from the MeerKAT central/core position (RA(J2000) = $22^h18^m34^s.96$ and DEC(J2000) = $-08°22'53''.50$) to the individual counterpart's position.

The achieves data points for hot-spot region		
NVSS (radio band) [Offset (RA = $1.04''$, DEC = $0.25''$)]		
Frequency [Hz]	Flux [Jy Hz]	Flux_error [Jy Hz]
1.4000×10^{9}	1.1620×10^{7}	1.2600×10^{5}
2MASS Point Sources (infrared band) [Offset (RA = $4.45''$, DEC = $4.12''$)]		
2.4274×10^{14}	2.8401×10^{11}	2.3057×10^{10}
1.8038×10^{14}	2.5794×10^{11}	2.4351×10^{10}
1.3885×10^{14}	2.3049×10^{11}	1.8051×10^{10}
SDSS Release 9 (optical band) [Offset (RA = $3.26''$, DEC = $5.57''$)]		
8.4420×10^{14}	4.7301×10^{10}	4.4940×10^{9}
6.3976×10^{14}	2.4124×10^{11}	1.775×10^{9}
4.8628×10^{14}	5.5733×10^{11}	2.5666×10^{9}
4.0074×10^{14}	7.1662×10^{11}	2.6401×10^{9}
3.3568×10^{14}	8.2557×10^{11}	8.3643×10^{9}
2XMMi source (X-ray band) [Offset (RA = $2.97''$, DEC = $2.02''$)])		
8.4629×10^{16}	4.9428×10^{7}	1.2695×10^{7}
1.8134×10^{17}	1.1138×10^{9}	3.2088×10^{8}
3.6270×10^{17}	6.5753×10^{8}	2.9992×10^{8}
7.8586×10^{17}	8.8354×10^{8}	5.5709×10^{8}
1.9948×10^{18}	9.4805×10^{8}	2.9560×10^{8}
Fermi-LAT 10-year Source DR2 (γ-ray band)		
2.4180×10^{23}	2.0000×10^{11}	1.0520×10^{11}

Table A.2: The achieves data points for the hot-spot region. The catalogues used to obtain these data points were accessed using SAOImage DS9. The offset direction is from the MeerKAT hot-spot position (RA(J2000) = $22^{h}18^{m}37^{s}.64$ and DEC(J2000) = $-08°21'12''.80$) to the individual counterpart's position.